A LEAPFROG NAVIGATION SYSTEM

A DISSERTATION

SUBMITTED TO THE DEPARTMENT OF AERONAUTICS AND ASTRONAUTICS

AND THE COMMITTEE ON GRADUATE STUDIES

OF STANFORD UNIVERSITY

IN PARTIAL FULFILLMENT OF THE REQUIREMENTS

FOR THE DEGREE OF

DOCTOR OF PHILOSOPHY

Guttorm Ringstad Opshaug

May 2003

I certify that I have read this dissertation and that in my opinion it is fully adequate, in scope and in quality, as a dissertation for the degree of Doctor of Philosophy.

Per K. Enge
(Principal Advisor)

I certify that I have read this dissertation and that in my opinion it is fully adequate, in scope and in quality, as a dissertation for the degree of Doctor of Philosophy.

Bradford W. Parkinson

I certify that I have read this dissertation and that in my opinion it is fully adequate, in scope and in quality, as a dissertation for the degree of Doctor of Philosophy.

Stephen M. Rock

Approved for the University Committee on Graduate Studies.

~

Abstract

There are times and places where conventional navigation systems, such as the Global Positioning System (GPS), are unavailable due to anything from temporary signal occultations to lack of navigation system infrastructure altogether. The goal of the Leapfrog Navigation System (LNS) is to provide localized positioning services for such cases. Specific applications may range from Mars exploration, via autonomous snow cats, to providing positioning to groups of firemen inside a burning building.

The concept behind leapfrog navigation is to advance a group of navigation units teamwise into an area of interest. In a practical 2-D case, leapfrogging assumes known initial positions of at least two currently stationary navigation units. Two or more mobile units can then start to advance into the area of interest. The positions of the mobiles are constantly being calculated based on cross-range distance measurements to the stationary units, as well as cross-ranges among the mobiles themselves. At some point the mobile units stop, and the stationary units are released to move. This second team of units (now mobile) can then overtake the first team (now stationary) and travel even further towards the common goal of the group. Since there always is one stationary team, the position of any unit can be referenced back to the initial positions. Thus, LNS provides absolute positioning.

In this work I started by looking at different technologies for providing the cross-range measurements needed for leapfrogging. GPS and Ultra-WideBand (UWB) were considered as candidate technologies. I also studied how multipath reflections affected the fundamental ranging measurements of the two technologies. Simulations showed that multipath may bias GPS code phase measurement by several meters. This magnitude of error was found to be too large for a viable Leapfrog Navigation System. However, similar simulations showed representative multipath errors of only 1.6 cm and 5.7 cm for GPS carrier and UWB respectively. Both error magnitudes were considered to be within tolerances for use with LNS.

Furthermore, I developed navigation algorithms needed to solve leapfrog positions based on cross-range measurements. I used statistical tools to predict how position errors would grow as a function of navigation unit geometry, cross-range measurement accuracy and previous position errors. Using this knowledge I predicted that a Leapfrog Navigation System using 100 m baselines and 200 m leap distances could travel almost 15 km before accumulating absolute position errors of 10 m (1σ).

Finally, I built a prototype leapfrog navigation system using 4 GPS transceiver ranging units. I placed the 4 units in a 10m x 10m grid, and leapfrogged the group 20 meters forwards, and then back again. Average horizontal RMS position errors never exceeded 16 cm during these field tests.

Acknowledgements

First off I would like to thank my advisor, Professor Per Enge, for giving me the right mix of guidance and freedom to explore new ideas. Every time I left his office I felt I had inched a little closer towards finishing, and I had "mysteriously" picked up a new task to accomplish for our next meeting. These "Per-reviews" certainly made the Ph.D. process very worthwhile.

Second, I want to thank my two other reading committee members, Professors Brad Parkinson and Steve Rock. Both proved invaluable in helping me focus in on the important parts of my research. Furthermore, all my reading committee members are outstanding teachers who make learning into a fun experience.

Next, I am truly grateful of my parents, Erna and Otto, for being so supportive and understanding although I by now have spent nearly 9 years 9 time-zones way from home. The same goes for my friends back home, who I only get to see once or twice a year but who remain my fix stars.

I would like to take this time to thank all my friends and colleagues for all their help and support in my time here. In particular, C.O. Lee Boyce Jr. and Konstantin G. Gromov have been "in the trenches" with me since I first arrived. I would also like to thank Alexander "Sasha" Mitelman, Michael Koenig, Dennis Akos, Ming Luo, Keith Alter, Jock Christie, Masayoshi Matsuoka and Yolanta Lubos personally.

Great thanks go to the staff of both the Aero and Astro Department and HEPL/GP-B. Especially, I feel that Aldo Rossi, Sherann Ellsworth and Dana Parga have made my life a lot simpler.

I also would like to thank the good people at Alpine Meadow Ski Resort for providing me with a snow cat for some of my early field tests. Eric Carlson and Dave Sheetz were instrumental in that process.

Finally, I would like to thank all my friends on the Stanford Ski Team who have made my time here so enjoyable.

Table of Content

List of Tables

~

List of Figures

~

1 Introduction

The goal of this work is to develop a navigation system for areas where coverage of any conventional navigation service is scarce or altogether void.

1.1 Background and Motivation

1.1.1 GPS

From its conception in the 1970's the Global Positioning System (GPS) has grown from being just a military system to one that is predominantly used by the civilian society. Current estimates of the number of GPS users are in the tens of millions worldwide [1] and that number is steadily growing. Applications range from finding your position when you are out hiking to being found if you have an emergency [2], and from driving farm tractors around cornfields [3] to landing planes at airfields [4]. To accomplish these tasks, GPS user hardware (HW) has also gone through a revolution; from backpack-sized units costing \$10k+ [5], to a couple of integrated circuits (ICs) that takes up less than a square centimeter and costs a few dollars to produce [6].

Non-augmented GPS requires orbital information and measurements from at least 4 satellites (Space Vehicles - SVs) in order to solve for 3-D user position and clock bias [7]. The satellites travel in sidereal 12-hour orbits, roughly 20200 km off the ground. The GPS constellation currently holds a total of 28 SVs in 6 orbital planes of 55 deg inclination. The original specification (1973) for GPS called for 21 SVs with 3 orbital spares [5]. Although there are currently 7 satellites more than that operational minimum, there is no guarantee that at least 4 SVs are visible absolutely everywhere on Earth absolutely all the time. One particular example of this problem can be inferred from Figure 1.1.

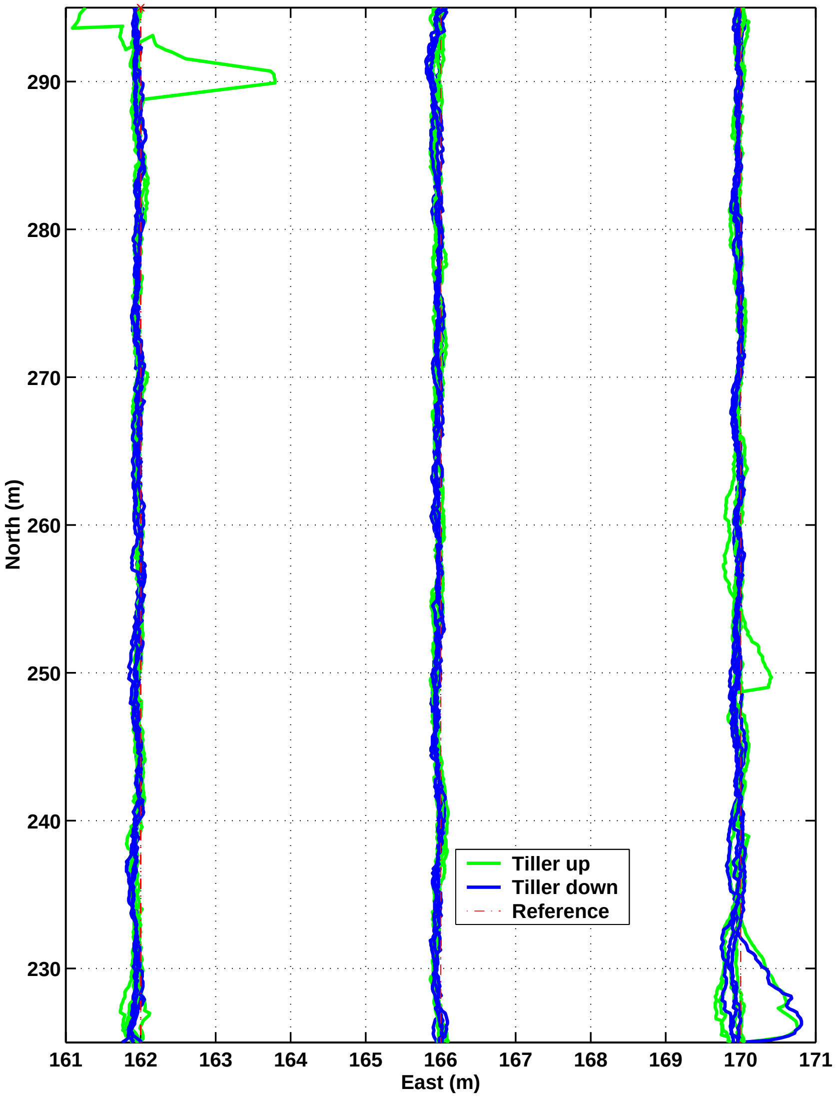

Figure 1.1 Snow Cat Field Test Results

Figure 1.1 shows results from a field test of a GPS-based snow cat autopilot performed at Alpine Meadows Ski Resort on 4/15/02. The solid lines show position fixes of the snow cat as it is set to follow reference lines at 162, 166 and 170 meters east. Although the autopilot follows its pre-programmed courses to within ~ 10 cm most of the time, there are a couple of outliers at (170E, 248N) and (162E, 288N) (the ones at (170E, 225N) are transient responses). Seemingly, the 8-ton heavy snow cat jumps several meters to the side in 1/5 second (update rate). However, these anomalies align with drop-outs in GPS tracking. GPS was available about 50% of the time during the field test campaign. The main reason for this can be better understood by looking at Figure 1.2.

Figure 1.2 Alpine Meadows Field Test Area

The test area at Alpine Meadows was lined with tall trees, and surrounded by tall mountains, blocking clear view of much of the GPS constellation.

Signal occultations may also occur if one tried to receive GPS indoors [2]. Most wall materials attenuate GPS signals 5-25dB [8], and that will threaten the margins in the GPS link-budget.

Both the indoor and the outdoor cases may be affected by multipath reflections in addition to reception-power limitations. Multipath reflections will bias the fundamental GPS pseudorange[1] measurements and ultimately result in an erroneous position solution. In general, the 20 msec data bit duration of GPS limits received power accumulation (thus power margin), and the 1.023 MHz C/A-code chip rate makes GPS susceptible to multipath components that are within ~300 m (one chip width) of a direct path signal. Thus, there is a question if GPS has "the right" signal structure for some navigation applications in multipath intensive environments. Chapter 2 provides further information about the GPS signal structure.

The introduction of E-911 [2] has sprouted much new research into the areas of indoor and urban canyon navigation, and some methods already show great results in alleviating signal power and multipath concerns [9]. However, there are still cases where GPS may be unavailable, either due to the above constraints, or due to lack of infrastructure altogether. The first case may be navigation through a tunnel, while the latter may be navigating the surface of distant planets.

1.1.2 Ultra-WideBand (UWB)

UWB technology started in the early 1960s in an attempt to characterize multi-port RF devices [10]. This could be done by sweeping a sinusoidal signal by the device to measure its frequency response, or equivalently, find its time-domain impulse response by exciting it with a short pulse. Most current UWB devices work by transmitting such short pulses instead of continuously modulating a carrier with another signal. These

---

[1] One-way range from SV to user, biased by user clock error.

pulses can be made to have very short durations, typically about 1 nanosecond (corresponding to 0.3 meters). The term Ultra-WideBand comes from the fact that the frequency spectrum of such a short pulse is very wide (~1 GHz for a 1 ns pulse). By current definition [11], a transmitter can be characterized as UWB if either of the following equations hold true:

$$2 \cdot \frac{f_{hi} - f_{low}}{f_{hi} + f_{low}} > 0.2 \qquad \textbf{Eq. 1.1}$$

or

$$f_{hi} - f_{low} > 500 \text{ MHz} \qquad \textbf{Eq. 1.2}$$

The first equation is a measure of fractional bandwidth, where f_{hi} and f_{low} are the upper and lower -10dB cut-off frequencies. Equation 1.2 is a classification constraint on the -10dB bandwidth of a signal. In the following we will assume use of pulses when dealing with UWB, although the above equations give no such requirements.

In addition to their almost infinite spectral diversity, UWB signals may be designed to have a significant portion of their spectrum at low frequencies. This makes UWB suitable for applications such as ground and foliage penetrating radars [12]. Another great virtue of UWB is its robustness towards fading from multipath reflections. It is possible to distinguish a direct signal from a multipath reflection if the two components are more than one pulse width apart. UWB sounding pulses have been used to measure various RF propagation environments to gain knowledge about their fading characteristics [13].

Recently there has been a drive to introduce UWB in cheap and ubiquitous communication devices. While such devices certainly may simplify many tasks, the greatest possible pitfall of UWB is intrinsic to the technology itself. The fact that a device is Ultra-WideBand means that it radiates power inside frequency bands that are assigned to other services. One argument is that the radiated power density is below FCC Part 15 regulations on unintentional radiation [11] (e.g. from microwave ovens, TV sets, PCs etc.). However, tests show that UWB may destructively interfere with GPS [14]. The current FCC ruling [15] on the matter calls for a -71.3 dBW/MHz level for unintentional interference, but a UWB level of -105.3 dBW/MHz in the frequency bands of GPS.

1.1.3 Mars Mission

This dissertation focuses on ways of providing navigation services to areas with little or no ordinary GPS coverage. The planet Mars is a prime example of such an environment.

The 1996-97 NASA Mars Pathfinder mission carried the Sojourner rover [16]. This vehicle had stereo vision cameras and an array of laser range finders for viewing the Martian surface. Navigation was done by gyro/accelerometers in addition to odometer readings. Sojourner was essentially remotely operated from Earth, and never ventured very far from the landing site. Future Mars missions may call for dust and rock samples to be returned to Earth for closer studies [17]. It may be of interest to collect such samples in the not-so immediate surroundings to the landing site. Both geological measurements and preparations for an eventual human habitat on Mars may require grid-like surveys over areas several square kilometers in size.

1.2 Previous Work

1.2.1 GPS Transceivers (GPST) and Synchrolites

Jonathan Stone developed the GPS Transceiver concept in his work with open pit mining trucks [18]. Open pit mines may be hundreds of meters deep with very steep side walls, making GPS reception as difficult as in any urban canyon. One solution to this problem is to place GPS transmitters, or pseudolites (PLs), around the rim of a mine. This ensures that the required number of GPS signals is available in order to calculate truck positions. A fixed differential GPS (DGPS) reference station [19] is also needed to gain the required positioning accuracy for guiding the trucks.

In its simplest implementation, a GPS transceiver consists of a GPS receiver, a pseudolite and a data link radio for transmitting corrections. Gaining the advantage of collocating a PL with a GPS differential reference station, comes at the cost of one data-link transmitter per unit. Simple GPS transceivers can easily be put together using commercially available products.

The predecessor of the GPS Transceiver is the “Synchrolite” developed by Stuart Cobb [20]. This device also consists of a GPS receiver and a pseudolite. However, an incoming GPS signal was synchronously re-transmitted using a different C/A-code, somewhat like an FM-radio repeater. No extra data link is needed for each device, but Synchrolites may prove expensive to produce due to extreme signal isolation requirements.

Synchrolites and GPS transceivers are all but the same when it comes to the fundamental measurements they provide. Thus the navigation equations to be solved look similar for the two devices.

1.2.2 Self Calibrating Pseudolite Arrays (SCPA)

Edward LeMaster introduced the concept of Self Calibrating Pseudolite Arrays in his Ph.D. work [21]. SCPA tests used one GPS transceiver mounted in a rover and 3 stationary ones on the ground. The array was synchronized to the pseudolite of the primary GPST, which made the system completely independent of regular GPS. By driving the rover around the stationary array of GPSTs, GPS carrier cycle ambiguities and cable biases were resolved. Ultimately, one could use the corrected measurements to compute the positions of both the rover and the entire fixed array.

The target application of SCPA is Mars exploration. Once a SCPA is initialized, its rover could roam freely in the area around the landing site. Position accuracies of a few centimeters are expected within a few baseline-distances from the array. However, total system range would be limited by array size and transmit-power levels, e.g. 1 μW of transmit power would limit total range to a few hundred meters.

1.2.3 Ad Hoc Navigation Systems

SCPA is one example of self-configuring, or ad hoc, navigation systems. Another system that has been suggested uses “thrown” Ultra-WideBand (UWB) pseudolites [22]. A reference station would be left by the entrance to an area of interest. UWB PLs would then be thrown around randomly, cross-ranges among all units would be measured, and positions of the fixed UWB PLs could be calculated. Once the fixed grid was initialized, users could find their positions by measuring cross-ranges to UWB PLs in known locations.

System coverage could be extended by throwing more units into an area of interest, thus leaving a trail of RF “bread crumbs” for finding one’s way back to the starting point.

Such a system may be used for providing positioning information to firemen entering a burning building or for other incursions into areas with limited visibility.

Æther Wire and Location Inc [23] is developing Ultra-WideBand Localizers. These ranging devices were originally intended to provide relative locations of all nodes in a swarm of mobile units. In addition to their obvious military applications, UWB Localizers may also find use in other kinds of distributed networks. Both inventory control [24] and Intelligent Vehicle Highway Systems (IVHS) could be implemented using this technology, but UWB Localizers are not yet commercially available.

1.2.4 Radio Frequency Channel Modeling

Understanding the propagation environment in which a radio system operates is vital in predicting its performance. The range of an indoor system [25] may be severely limited by signal attenuation through walls, and a city-wide outdoor network [26] may experience deep fades due to multipath reflections from surrounding buildings. There are several ways of characterizing an RF channel, and the fundamental measurements are generally its power spectrum or its power delay profile. Frequency domain techniques answer questions that involve Doppler effects, as well as frequency selective fading. The time domain power delay profile gives an accurate measurement of relative strength and arrival times of a direct signal and its multipath components. Both measurement types are frequently used in order to create statistical models of signal fading. Received signal power may be approximated by a Rician distribution [8, Ch. 4.6] if one signal component is significantly stronger than the others. Conversely, one would experience Raleigh fading [8, Ch. 4.6] if all components were to arrive with random delays but similar signal strengths.

Performance of communication systems is mainly described by their received signal-to-noise ratios (or bit-energy to noise energy ratios for digital systems). Thus, understanding the effects of fading becomes imperative in designing a communication system [27].

Although the navigation community considers multipath to be a malevolent term, others may actually use multipath to their advantage. Kjesbu et. al. tested IEEE 802.11b devices inside of the steel-lined dome of a nuclear reactor [28]. While this may be one of the harshest multipath environments one can imagine, their research showed that one transmitter would cover most of the building. Their equipment continued to operate even when steel pillars blocked the line-of-sight path between two devices. Multipath carried enough signal energy to be received almost everywhere, as signal reflections flooded the building.

Navigation systems, like GPS, are ruled by the same basic laws as communication systems although there are differences in how multipath affects the two. In both cases, it is important to characterize the propagation environment and how it affects various signal structures in predicting the corresponding system performances.

1.3 Contributions

I conceived, designed, built and tested the Leapfrog Navigation System (LNS). LNS was by no means created in a vacuum, and the system has its origins in Self Calibrating Pseudolite Arrays. Whereas SCPA only has one mobile unit, all units of LNS are mobile, effectively increasing system range by more than an order of magnitude. Furthermore, LNS does not require littering your path with “bread crumbs”, but rather “remembers” the trail as it goes on (If only Hansel and Gretel were so lucky). LNS requires known initial positions, e.g. given by a SCPA-like initialization. After calibration LNS is divided into two groups. One group starts out in their known stationary positions, while the others move into an area of interest. At some point, the mobile units stop, their positions are calculated using cross-range measurements, and the stationary group is released to move. In this way the group as a whole can travel towards a common goal.

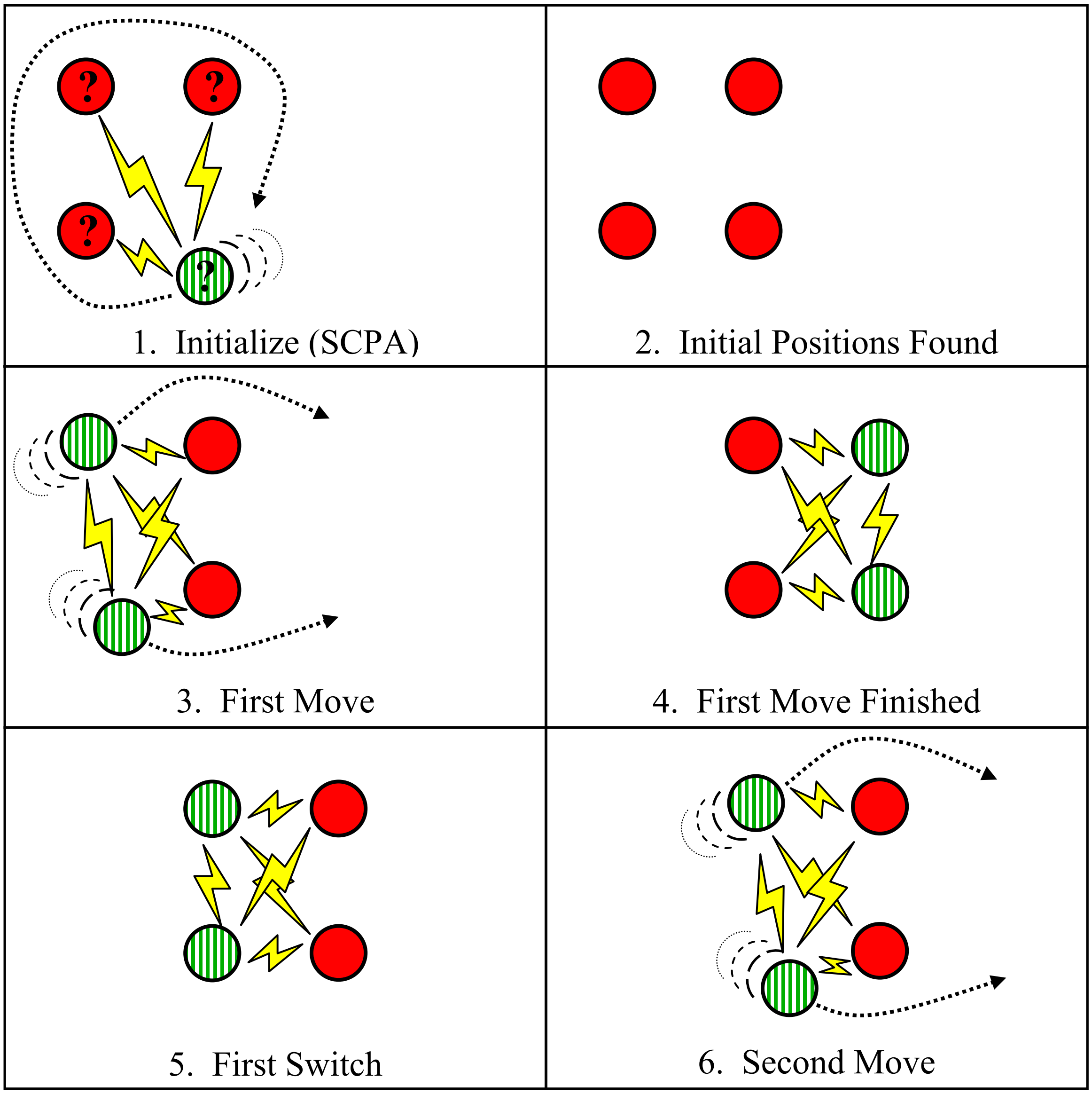

1. Initialize (SCPA)

2. Initial Positions Found

3. First Move

4. First Move Finished

5. First Switch

6. Second Move

Figure 1.3 Leapfrog Operations

Figure 1.3 shows a typical operational sequence in LNS. In the figure, solid circles are stopped units and striped circles are mobile ones. Question marks are used to show where initial positions are yet unresolved. The lightning bolts indicate cross-range measurements.

Furthermore, I developed algorithms for solving LNS positions of the mobile units using cross-range measurements from all stationary units in addition to the cross-ranges among the mobile units. I did a statistical covariance analysis for the pre-leap mobile positions, and found that position accuracies depended on the size of the fundamental range errors and relative geometry of the total system. I did a similar analysis for the post-leap case, and I found an additional term to the previous equation that described error accumulation due to the previous uncertainty of the stationary positions. Finally, I developed a recursive algorithm to estimate total position errors after N leaps of any distance.

GPS is affected by multipath fading in the same way as communication systems, but there are additional effects. Although maintaining a minimum signal-to-noise (SNR) ratio is necessary for GPS tracking, it is not a sufficient condition for proper operation. In order to understand the fundamental ranging accuracies of LNS, I measured both an indoor and an outdoor navigation channel (propagation environment). In this work I found a metric for estimating effects of multipath on positioning systems in cluttered environments. The Strongest Arrival Delay (SAD) is a first order estimate of the ranging bias introduced by multipath that is stronger than a direct path signal. Indoor and outdoor navigation channel measurements were used to model such ranging errors.

Given ranging errors and system topology, the total range of LNS could be estimated given a tolerance on absolute position errors.

LNS was implemented using GPS Transceivers based on off-the-shelf components. Field tests with 4 units starting out in the vertices of a 10m x 10m quadrate showed position errors better than 20 cm after 4 leaps of 10 meters each.

1.4 Outline of Dissertation

Several elements should be carefully considered in designing a Leapfrog Navigation System. First, available technologies for navigation must be identified. Next, each technology must provide a way for mechanizing its fundamental navigation equations into algorithms that yield positioning. Finally, candidate technologies must be described in terms of power consumption, size of equipment, signal structure, susceptibility to multipath etc.

Both GPS and UWB are presented in Chapter 2 of this thesis, and their signal structures are describes in detail. Chapter 2 also contains the fundamental ranging equations for separate suggested GPS and UWB implementations of LNS. Linearized sets of those ranging equations are the basis for iterative algorithms for positioning.

The environment in which the system is to be used will affect its design, both in terms of physical robustness and in identifying significant error sources. Multipath reflections will for example be of greater concern indoors than out in an open field.

While Chapter 2 also describes effects of multipath on receiver structures for GPS and UWB, Chapter 3 presents indoor and outdoor measurement of actual multipath. Multipath is characterized through statistical parameters, but the measurements also provide estimates of fundamental LNS cross-range errors.

The geometrical layout of a navigation system affects the accuracy it can provide in different locations. This effect is referred to as Dilution-of-Precision (DOP).

Chapter 4 uses DOP and cross-range errors to simulate the positioning accuracy of LNS. Position errors accumulate as navigation units are switched between their mobile and stationary states, and Chapter 4 provides bounds on total system range as a function of allowable absolute position error.

Combining all error sources with the description of hardware one can predict system performance in terms of accuracy, availability, range, etc. A final trade study should also include cost and time of development.

Chapter 5 in this thesis describes LNS hardware design choices. While UWB is inherently robust against multipath, unlike GPS, there is currently no off-the-shelf equipment available. Thus, a prototype LNS was implemented using GPSTs and results from field tests are presented in that chapter.

Planetary surface exploration is one of the target applications for the Leapfrog Navigation System. Such missions would put extreme requirements on LNS in terms of hardware, operations and integration with other systems. Thus, Chapter 6 is a systems-level design study of a possible Mars mission that employs LNS. A fresh look is taken on choosing and integrating HW with possible rovers. Techniques for augmenting LNS positioning are considered, and different operational scenarios are studied.

Chapter 7 summarizes contributions and results, and that final chapter suggests improvements to LNS and future research directions.

2 Theory

This chapter provides the necessary theoretical background for design of a Leapfrog Navigation System (LNS). Signal structures of both GPS and Ultra-WideBand will be described. Both fading and range errors result from multipath, and its effects on the two technologies will be studied in detail. While UWB is inherently robust against such signal reflections, little hardware currently exists for implementation. Plenty GPS equipment is readily available, but there is a question of how well the GPS signal structure deals with multipath. This chapter quantifies multipath-induced range errors for GPS and a typical UWB system through simulations.

Finally, the navigation equations and their solutions will be developed for both GPS-based and UWB-based LNS, although a prototype LNS was ultimately implemented using GPS. Unlike regular GPS positioning algorithms, the LNS ones contain ranges among mobile users in addition to ranges to fixed stations (the equivalent of satellites).

2.1 GPS Signal structure

GPS uses spread-spectrum technology, and is also referred to as a Code-Division Multiple Access (CDMA) system. GPS operates at two different carrier frequencies, L1 at 1575.42 MHz and L2 at 1227.6 MHz. The L2 frequency is binary-phase-shift key (bpsk) modulated with the military P/Y-code[2]. This code is based on a known Pseudo

---

[2] A new civilian signal should be available on L2 beginning sometime in 2004

Random Number (PRN) sequence, but is further encrypted for military use only. L1 is also modulated with the P/Y-code, but in addition contains the civilian C/A-code which is open to everybody. While the P/Y-code runs at a Chip rate of 10.23 MHz, the C/A-code runs at one tenth of that and it repeats every millisecond. On top of the C/A-code is modulated a navigation message at 50 bits-per-second (bps). A data message bit flip inverts the underlying C/A-code. Figures 2.1 and 2.2 show time and frequency-domain representations of the civilian signal on L1.

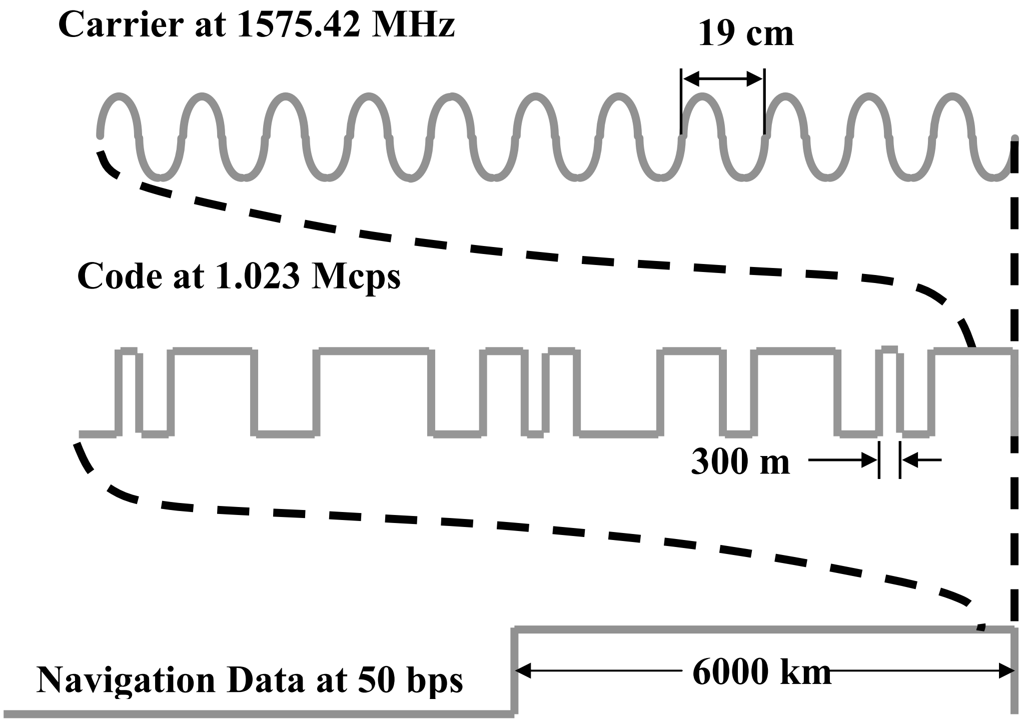

Figure 2.1 GPS SPS Time-Domain Signal Structure at L1 (Courtesy Per Enge)

The 1.023 MHz chipping rate gives 2.046 MHz spacing between the first nulls in the sinc envelope (as seen in Fig. 2.2).

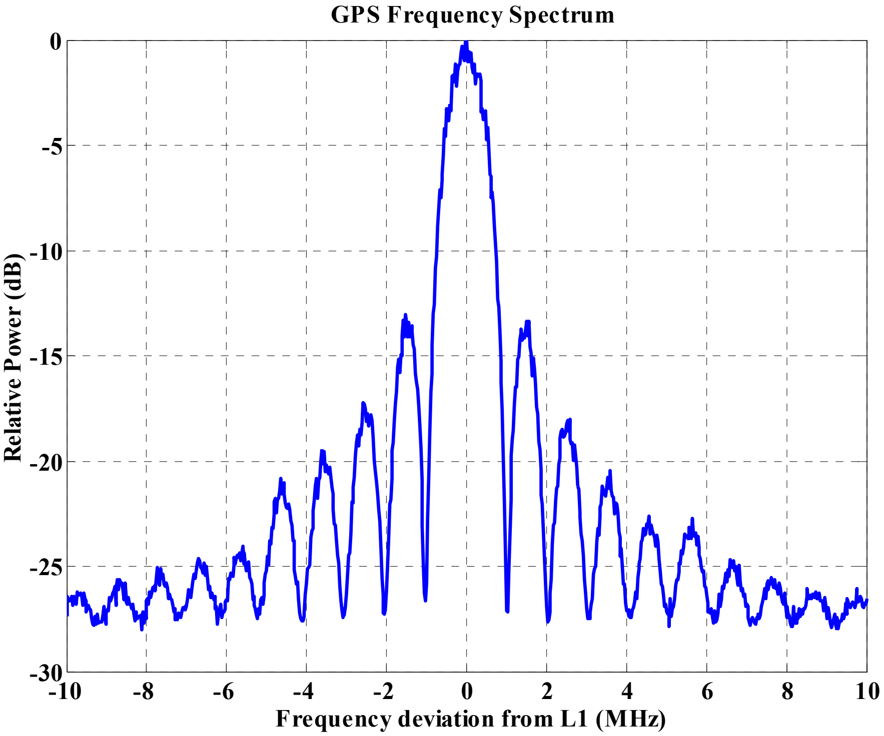

Figure 2.2 GPS SPS Frequency Domain Signal Structure

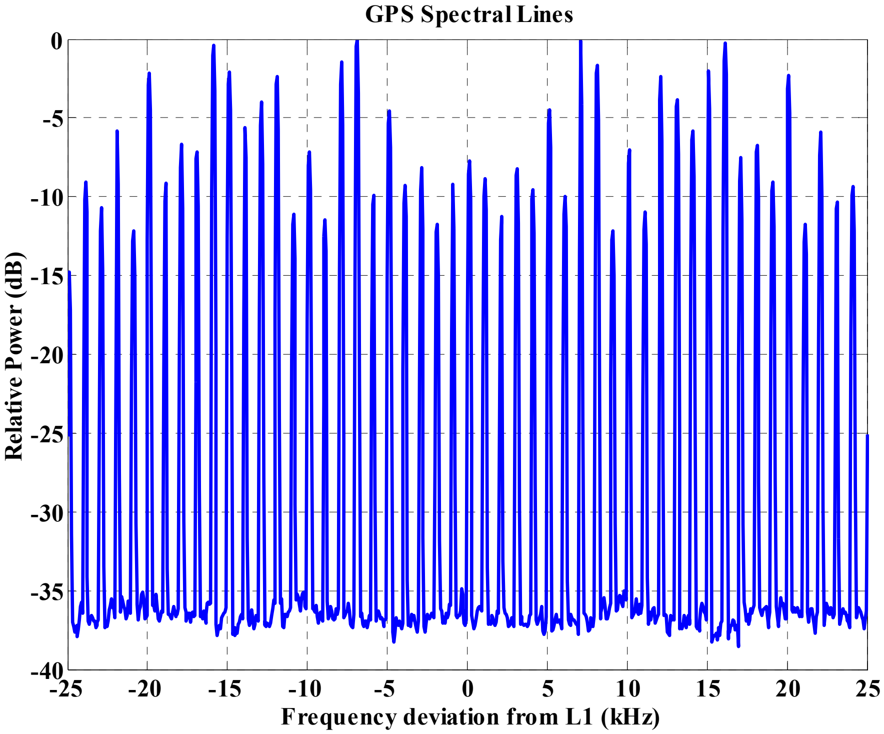

Figure 2.3 GPS SPS Frequency Domain Fine Structure

Figure 2.3 shows an expanded view of a C/A-code spectrum around L1. The spectral lines in the C/A-code spectrum come from the pseudo-random nature in which the code chips are distributed and the fact that there are 20 repeats of the C/A-code per navigation bit. The C/A-code repeats every 1 msec, and the corresponding 1 kHz line spacing can be easily observed in Fig. 2.3.

C/A-code tracking is typically done through correlating the received signal with a locally generated C/A-code sequence. In frequency domain the correlation operation is equivalent to a multiplication of the two spectra. Since the GPS signal energy lies in such spectral lines, interference on those specific frequencies can be very damaging to GPS operation [29].

2.2 UWB Signal Structure

Unlike GPS there is no unified signal structure for UWB. While some UWB devices are based on continuous envelope signals, most use pulsed signals. Such signals can be generated e.g. by rapidly switching a PIN diode on and off. Figures 2.4 and 2.5 show the time plot and frequency spectrum of a sample UWB pulser respectively (HyperLabs HL9200).

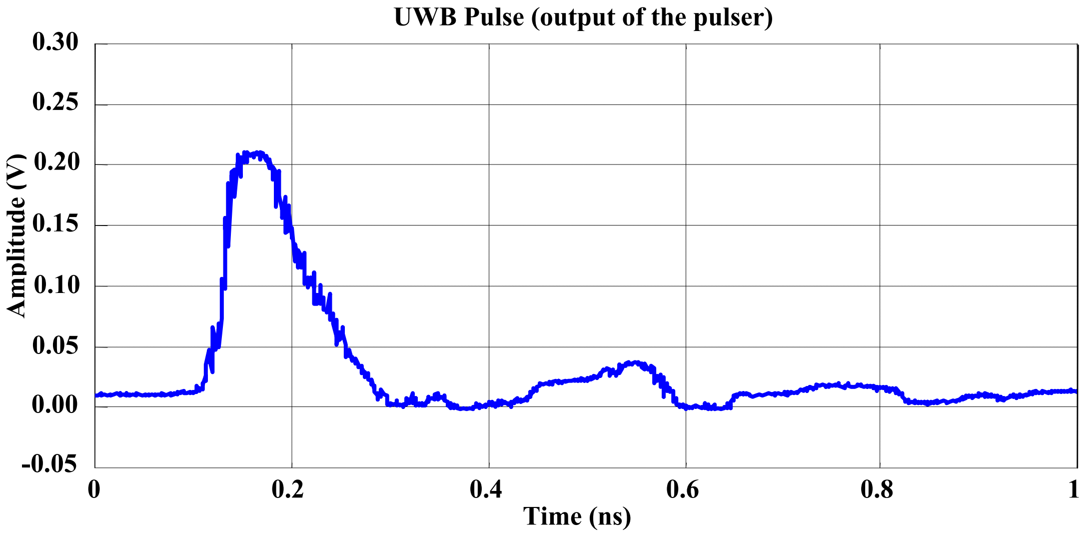

Figure 2.4 UWB Pulse (Courtesy Ming Luo)

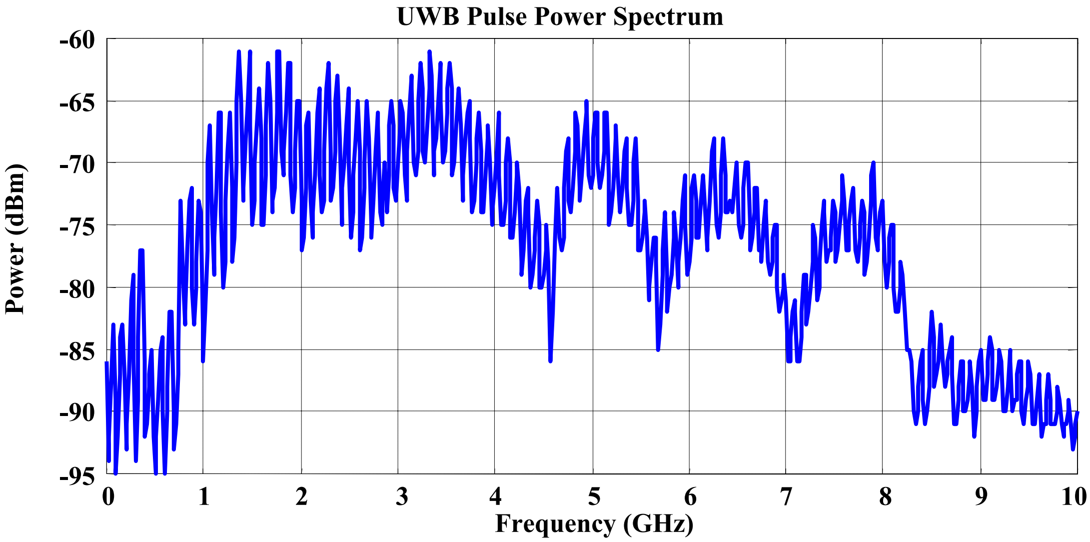

Figure 2.5 UWB Frequency Spectrum (Courtesy Ming Luo)

However, the signal that is transmitted through an antenna may differ significantly from the one shown in Figs 2.4 and 2.5. Figure 2.6 shows how a pulse changes after going through a filter and an amplifier successively.

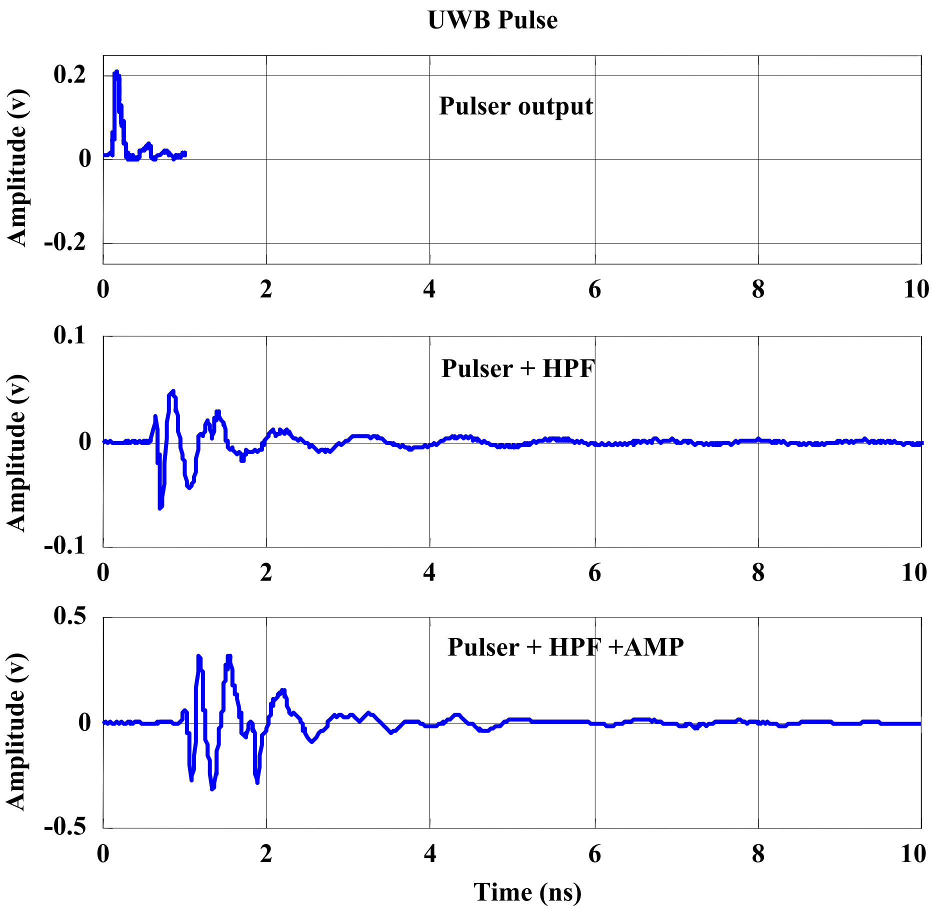

Figure 2.6 Effects of Filter and Amplifier on UWB Pulse (Courtesy Ming Luo)

The high-pass filter (HPF) and amplifier (AMP) smear out the original pulse, and the resulting signal is DC balanced since a high-pass filter was used. The two devices also introduce ringing in the resulting responses.

Since un-filtered UWB may have significant spectral content at lower frequencies used for e.g. radio and TV broadcast, only special ground/building penetrating radars will be allowed to operate in this mode [15].

The FCC has temporarily opened for unlicensed use of the 3.1-10.6 GHz band for indoor UWB communication devices [15], as long as these comply with FCC Part 15 regulations [11]. A final FCC decision on UWB use is expected by mid 2003. It is important to note that other radio systems operating at those frequencies may require several intermediate-frequency (IF) stages for down conversion due to oscillator phase-noise concerns. Detection and tracking of a UWB signal does not require phase lock of a carrier. The technology holds the promise of a non-complex and an inexpensive implementation. In its simplest form, a UWB receiver may be no more than an envelope detector, much like an AM receiver.

A single UWB pulse has a continuous and aperiodic frequency spectrum [30]. A train of such pulses yields an aperiodic spectrum with strong spectral lines. Random modulation of these pulses will tend to suppress the spectral lines and smear the spectrum back towards a continuous one.

Various modulation techniques for UWB systems have been suggested. The two main techniques used, are pulse-position modulation and pulse-polarity modulation. Pulse-position modulation works by varying the relative distance between transmission of pulses, and the figure below shows an example.

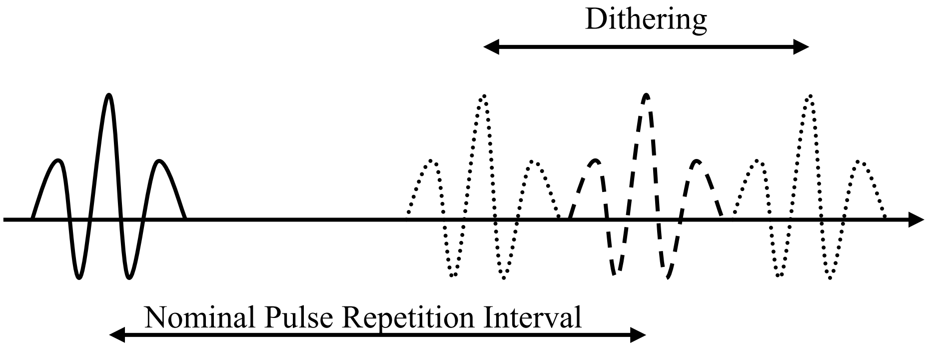

Figure 2.7 Pulse Position Modulation

Pulse-polarity modulations may come in many forms, but pulse-doublets are frequently used [31]. Figure 2.8 shows a typical example of pulse-doublet modulation where a sequence of bits is generated by changing the polarity of a transmitted pulse doublet.

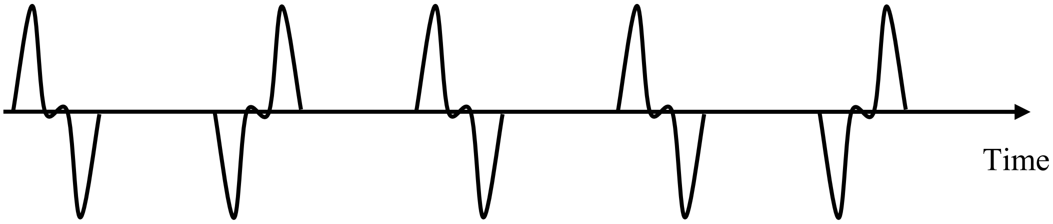

Figure 2.8 Pulse-Doublet Modulation (+ - + + -)

Pulse-doublets are similar to Manchester codes [32], used in other communication systems, because they are balanced. This is important in assuring that a signal has no DC component, which would be all but impossible to transmit through an antenna.

2.3 Cross-Range Navigation Equations

The Leapfrog Navigation System uses measurements of the distances among its units to calculate their positions. Such cross-range measurements may be provided by GPS Transceivers, but UWB based transponders could also be used for the same task.

The number of cross-range measurements available for a total of *N* units is

$$\frac{N \cdot (N-1)}{2} \text{ for } N \geq 2 \qquad \textbf{Eq. 2.1}$$

If LNS has *M* mobile units (and *S* stationary ones, $N = M + S$), the number of useful equations will be:

$$M \cdot (N-M) + M \cdot (M-1)/2 \text{ for } N \geq 2, N > M \geq 1 \qquad \textbf{Eq. 2.2}$$

The $M \cdot (N - M)$ term of Equation 2.2 gives the total number of cross ranges from all stationary units, to all mobile ones, and $M \cdot (M - 1)/2$ gives the number of cross ranges among the mobile units.

Equations 2.1 and 2.2 can also be used to find the minimum number of units required for operation. In a 2-D case, *N* units will have $2 \cdot N$ unknown position coordinates initially. If we are only interested in finding relative positions, we can reduce the requirements in two ways.

First, pick one (any) of the units to be at the origin of our coordinate system. This leaves $2 \cdot N - 2$ unknown positions, and yields the following equation.

$$\frac{N \cdot (N-1)}{2} \geq 2 \cdot (N-1) \qquad \textbf{Eq. 2.3}$$

In this case, 4 units are needed to solve the 2-D equation set.

Second, the previous requirement can be reduce further by cleverly mechanizing our coordinate system. Now, place one unit at the origin of a circular coordinate system, and another unit along the primary direction. The number of unknowns then reduces to $2 \cdot N - 3$. All measurements are used for initialization, thus

$$\frac{N \cdot (N-1)}{2} \geq 2 \cdot N - 3 \qquad \textbf{Eq. 2.4}$$

Although, the trivial case of *N* = 2 solves the equation, we find that a practical minimum of 3 units are needed in the 2-D case. In addition to our initial assumptions, we will also need to know if additional units have positive or negative angles with respect to the primary direction. This last condition can be found from Figure 2.9.

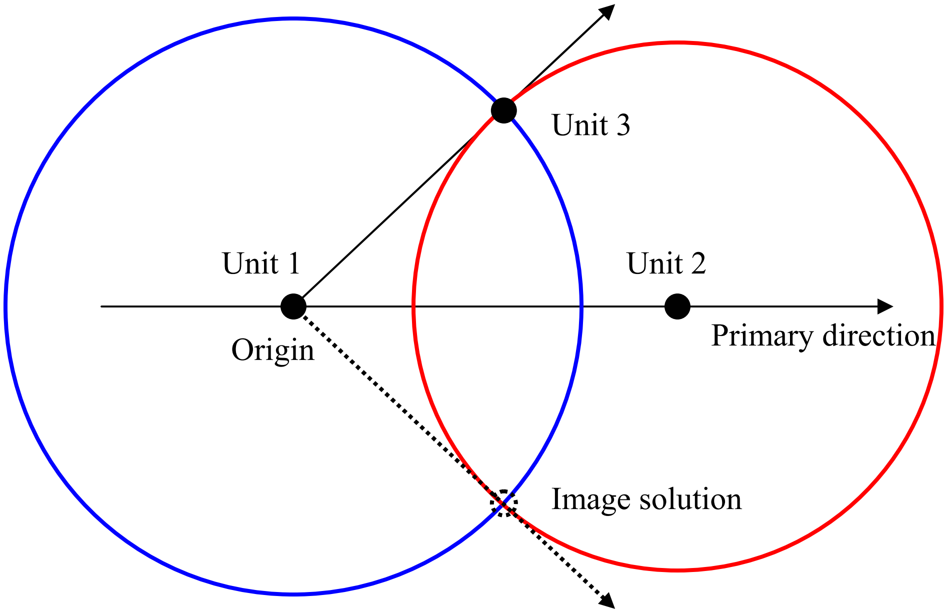

Figure 2.9 3-Unit LNS with Image Solution

GPS Transceivers

A GPS transceiver consists of a GPS receiver (RX) and transmitter (TX), known as a pseudolite, in addition to a radio for data exchange with other GPSTs. Figure 2.10 below shows a pair of GPS transceivers with non-collocated transmit and receive antennas.

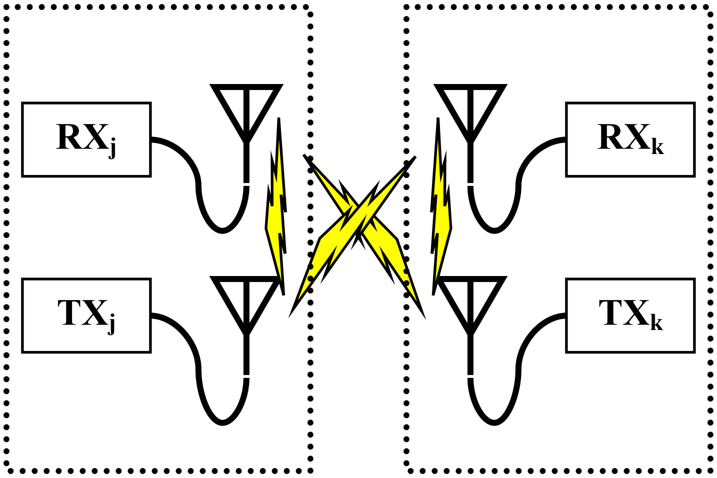

Figure 2.10 Dual Antenna GPS Transceivers

The fundamental navigation equations for a pair of GPSTs are given below.

$$\tau_j^{(k)} = d_j^{(k)} + \left(B^{(k)} - b_j\right) \cdot c + l_j^{(k)} + \upsilon_{\tau,j}^{(k)} \qquad \textbf{Eq. 2.5}$$

$$\phi_j^{(k)} = d_j^{(k)} + \left(B^{(k)} - b_j\right) \cdot c + l_j^{(k)} + N_j^{(k)} \cdot \lambda_{L1} + \upsilon_{\phi,j}^{(k)} \qquad \textbf{Eq. 2.6}$$

In the above equations, τ is code measurement and ϕ is carrier measurement. Furthermore, d is true distance between two antennas, $B^{(k)}$ is clock bias of transmit pseudolite k, b_j is clock bias of receiver j, c is the speed of light, N is the carrier cycle ambiguity, λ_{L1} is the carrier wavelength of L1, l is a cable bias and υ is a noise term. Superscripts denote transmitter terms, and subscripts denote receiver ones.

The lightning bolts in Figure 2.10 show the four individual range measurements given for a GPST pair (*j*-to-*j*, *j*-to-*k*, *k*-to-*j* and *k*-to-*k*). The following sum-of-differences operations on Equations 2.5 and 2.6 given those four measurements yield

$$\begin{aligned} \tau_{jk} &= \left(\tau_j^{(k)} - \tau_j^{(j)}\right) + \left(\tau_k^{(j)} - \tau_k^{(k)}\right) \\ &= 2 \cdot d_j^{(k)} + l_{jk} + \upsilon_{\tau,jk} \end{aligned} \qquad \textbf{Eq. 2.7}$$

$$\begin{aligned} \phi_{jk} &= \phi_j^{(k)} - \phi_j^{(j)} + \phi_k^{(j)} - \phi_k^{(k)} \\ &= 2 \cdot d_j^{(k)} + l_{jk} + N_{jk} \cdot \lambda_{L1} + \upsilon_{\phi,jk} \end{aligned} \qquad \textbf{Eq. 2.8}$$

The operation removed all clock terms from the equations. Here N_{jk} is a differential cycle ambiguity term, l_{jk} is a differential line bias term, and $\upsilon_{\tau,jk}$ and $\upsilon_{\phi,jk}$ are differential noise terms. While cycle ambiguities must be resolved each time signal tracking (re-)starts, the cable bias terms may not change significantly over time, and could be calibrated and removed initially.

2.3.1 UWB Transponder

UWB cross-ranging may lend itself to various multiple-access techniques. Several PRN sequences could be used, like GPS, but a simpler approach may be found in using transponders. Such devices work by measuring round-trip delays between pairs of units. A primary transponder may send out a query signal, which is received at a secondary unit. This unit will transmit a response after a given time-delay. The transponder concept is already widely used, e.g. in Distance Measuring Equipment (DME) [33] for aircraft navigation.

Figure 2.11 shows a block diagram of a transponder configuration.

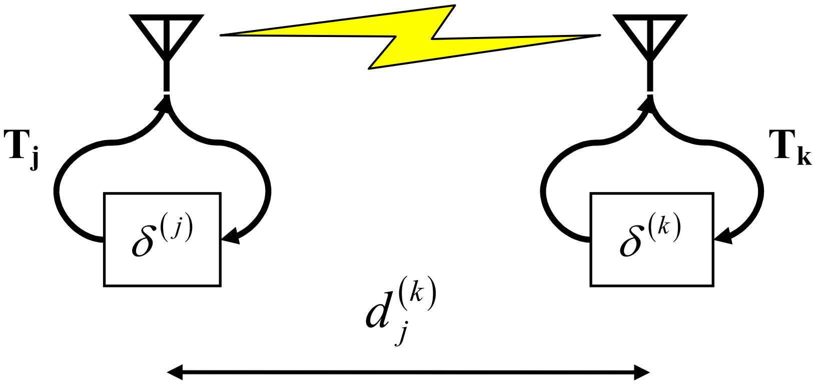

Figure 2.11 UWB Transponders

The fundamental navigation equation for a pair of transponders may be written:

$$\varphi_{jk} = 2 \cdot d_j^{(k)} + \delta^{(k)} + \upsilon_{\varphi,jk} \qquad \textbf{Eq. 2.9}$$

In the above equation, φ is the round-trip measurement, d is true distance between units j and k, δ is the secondary transponder processing delay, and υ is a noise term. A line bias term also exists due to antenna cabling, but this term is compounded with the processing delay.

The main advantage of using transponders over radars is the fact that free-space range is limited by $1/d^2$ instead of $1/d^4$ [34]. Furthermore, there is no need to solve any clock terms, provided that oscillator stabilities are good over the time interval of the ranging transaction. A simple UWB transponder would not transmit and receive at the same time, and their capacity would be limited by the total number of units in a network.

2.3.2 Linearized Sets of Navigation Equations

Iteratively solving sets of linearized equations is a frequently used technique for obtaining position fixes from fundamental ranging-equations [35]. The same sets of linearized equations may also be used in predicting accuracies of a navigation system based on its geometric layout and its fundamental ranging errors.

2.3.2.1 GPS Transceivers

We will only consider GPS carrier phase techniques for use with LNS. There are various ways of removing cable biases and carrier cycle ambiguities [36], and calibration leaves multipath as the potentially largest error term in the fundamental navigation equations. After making all the corrections, we can Taylor-series expand Equation 2.8 around the estimated location of the mobile unit (Equation 2.10). Our expansion includes the linear term, and higher order terms (HOT) are assumed to be significantly small. Appendix A analyses how sensitive the 2-D version of Equation 2.10 is to the impact of HOT.

$$\hat{\phi}_{m_1 s_1} \simeq 2 \cdot \left(d_{m_1,0}^{(s_1)} + \frac{\partial d_{m_1}^{(s_1)}}{\partial x_{m_1}} \cdot \Delta x_{m_1} + \frac{\partial d_{m_1}^{(s_1)}}{\partial y_{m_1}} \cdot \Delta y_{m_1} + \frac{\partial d_{m_1}^{(s_1)}}{\partial z_{m_1}} \cdot \Delta z_{m_1} \right) \qquad \textbf{Eq. 2.10}$$

In Eq. 2.10, $\hat{\phi}_{m_1 s_1}$ is the corrected cross-range measurement between mobile unit m_1 and stationary unit s_1. $d_{m_1,0}^{(s_1)}$ is the current estimate of true cross-range, and Δx_{m_1}, Δy_{m_1} and Δz_{m_1} are perturbations of the position of m_1 around its current estimate. We can further reduce the equation to

$$\frac{\hat{\phi}_{m_1 s_1}}{2} - d_{m_1,0}^{(s_1)} = \mathbf{los}_{m_1}^{(s_1)} \cdot \begin{bmatrix} \Delta x_{m_1} \\ \Delta y_{m_1} \\ \Delta z_{m_1} \end{bmatrix} \qquad \textbf{Eq. 2.11}$$

$\mathbf{los}_{m_1}^{(s_1)}$ is the line-of-sight (LOS) unit vector between the two GPSTs. For ranging between two mobile units, m_1 and m_2, perturbations around both positions must be found. Thus, Equation 2.11 changes to

$$\frac{\hat{\phi}_{m_1 m_2}}{2} - d_{m_1,0}^{(m_2)} = \mathbf{los}_{m_1}^{(m_2)} \cdot \begin{bmatrix} \Delta x_{m_2} \\ \Delta y_{m_2} \\ \Delta z_{m_2} \end{bmatrix} - \mathbf{los}_{m_1}^{(m_2)} \cdot \begin{bmatrix} \Delta x_{m_1} \\ \Delta y_{m_1} \\ \Delta z_{m_1} \end{bmatrix} \qquad \textbf{Eq. 2.12}$$

A 2-D case with 4 transceivers gives the following equation set:

$$\frac{1}{2}\begin{bmatrix} \hat{\phi}_{m_1 s_1} \\ \hat{\phi}_{m_1 s_2} \\ \hat{\phi}_{m_2 s_1} \\ \hat{\phi}_{m_2 s_2} \\ \hat{\phi}_{m_1 m_2} \end{bmatrix} - \begin{bmatrix} d_{m_1,0}^{(s_1)} \\ d_{m_1,0}^{(s_2)} \\ d_{m_2,0}^{(s_1)} \\ d_{m_2,0}^{(s_2)} \\ d_{m_1,0}^{(m_2)} \end{bmatrix} = \left[\begin{array}{c:c} \mathbf{los}_{m_1}^{(s_1)} & \mathbf{0} \\ \mathbf{los}_{m_1}^{(s_2)} & \mathbf{0} \\ \mathbf{0} & \mathbf{los}_{m_2}^{(s_1)} \\ \mathbf{0} & \mathbf{los}_{m_2}^{(s_2)} \\ \mathbf{-los}_{m_1}^{(m_2)} & \mathbf{los}_{m_1}^{(m_2)} \end{array}\right] \left[\begin{array}{c} \Delta x_{m_1} \\ \Delta y_{m_1} \\ \hdashline \Delta x_{m_2} \\ \Delta y_{m_2} \end{array}\right] \qquad \textbf{Eq. 2.13}$$

Matlab code for stacking up equation sets of arbitrary size is given in Appendix B.

2.3.2.2 UWB Transponder

The navigation equation for transponders can be linearized the same way as Equation 2.10 for GPSTs. In addition, an average of the two cross-ranges between a pair of UWB transponders can be used to reduce measurement variation. The two equations below are the UWB transponder equivalents of Equations 2.11 and 2.12.

$$\frac{\varphi_{m_1 s_1} + \varphi_{s_1 m_1}}{4} - \frac{\delta^{(s_1)} + \delta^{(m_1)}}{4} - d_{m_1,0}^{(s_1)} = \mathbf{los}_{m_1}^{(s_1)} \cdot \begin{bmatrix} \Delta x_{m_1} \\ \Delta y_{m_1} \\ \Delta z_{m_1} \end{bmatrix} \qquad \textbf{Eq. 2.14}$$

$$\frac{\varphi_{m_1 m_2} + \varphi_{m_2 m_1}}{4} - \frac{\delta^{(m_1)} + \delta^{(m_2)}}{4} - d_{m_1,0}^{(m_2)} = \mathbf{los}_{m_1}^{(m_2)} \cdot \begin{bmatrix} \Delta x_{m_2} \\ \Delta y_{m_2} \\ \Delta z_{m_2} \end{bmatrix} - \mathbf{los}_{m_1}^{(m_2)} \cdot \begin{bmatrix} \Delta x_{m_1} \\ \Delta y_{m_1} \\ \Delta z_{m_1} \end{bmatrix} \qquad \textbf{Eq. 2.15}$$

In these equations, φ is a measurement, d is the true distance between units, and δ is a processing delay. The bias part of this delay should remain constant over the lifetime of a transponder and could be calibrated upon production of the unit. There may still be variations in δ and the term is kept in the equations to remind us of that uncertainty.

The 2-D case described in Chapter 2.3.3.1 gives the equation set below:

$$\frac{1}{4}\begin{bmatrix} \varphi_{m_1 s_1} + \varphi_{s_1 m_1} \\ \varphi_{m_1 s_2} + \varphi_{s_2 m_1} \\ \varphi_{m_2 s_1} + \varphi_{s_1 m_2} \\ \varphi_{m_2 s_2} + \varphi_{s_2 m_2} \\ \varphi_{m_1 m_2} + \varphi_{m_2 m_1} \end{bmatrix} - \frac{1}{4}\begin{bmatrix} \delta^{(m_1)} + \delta^{(s_1)} \\ \delta^{(m_1)} + \delta^{(s_2)} \\ \delta^{(m_2)} + \delta^{(s_1)} \\ \delta^{(m_2)} + \delta^{(s_2)} \\ \delta^{(m_1)} + \delta^{(m_2)} \end{bmatrix} - \begin{bmatrix} d_{m_1,0}^{(s_1)} \\ d_{m_1,0}^{(s_2)} \\ d_{m_2,0}^{(s_1)} \\ d_{m_2,0}^{(s_2)} \\ d_{m_1,0}^{(m_2)} \end{bmatrix} = \left[\begin{array}{c|c} \mathbf{los}_{m_1}^{(s_1)} & \mathbf{0} \\ \mathbf{los}_{m_1}^{(s_2)} & \mathbf{0} \\ \mathbf{0} & \mathbf{los}_{m_2}^{(s_1)} \\ \mathbf{0} & \mathbf{los}_{m_2}^{(s_2)} \\ \mathbf{-los}_{m_1}^{(m_2)} & \mathbf{los}_{m_1}^{(m_2)} \end{array}\right] \left[\begin{array}{c} \Delta x_{m_1} \\ \Delta y_{m_1} \\ \hline \Delta x_{m_2} \\ \Delta y_{m_2} \end{array}\right] \qquad \textbf{Eq. 2.16}$$

2.4 Multipath Effects

Multipath is likely to be the most significant error source for a ground-based navigation system, and its effects on LNS must be understood. A simple multipath model has one reflection in addition to the direct signal.

$$S_{rx}(t) = S_{tx}(t) + \alpha \cdot S_{tx}(t - \delta t) \qquad \textbf{Eq. 2.17}$$

In the equation above, S_{rx} and S_{tx} are received and transmitted signals respectively. α is the reflection coefficient and δt is the relative delay.

2.4.1 GPS Code Phase

The GPS C/A-code is generally tracked using a Delay-Locked Loop (DLL). Figure 2.12 shows the block diagram of a DLL.

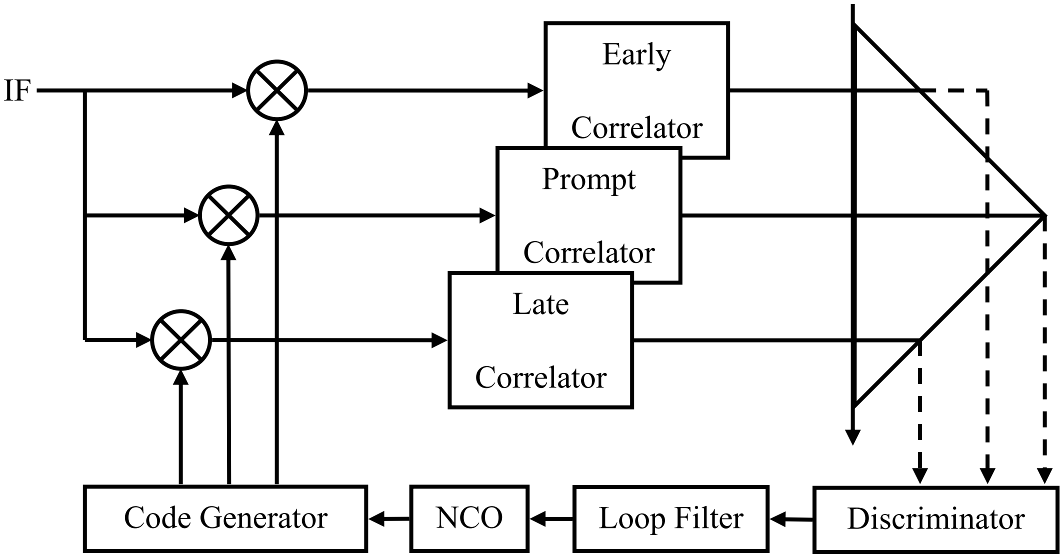

Figure 2.12 C/A-code Delay Locked Loop

The three parallel elements of the DLL give an early, a prompt, and a late measurement of the corresponding C/A-code correlation peak. Tracking is done by straddling the correlation peak (triangle to the right in Figure 2.12) with the early and late measurements and servoing their difference to zero.

Cyclic correlation operations between measurements of the incoming signal (at intermediate frequency, IF) and locally generated C/A-codes are used in the tracking loop.

$$r_{x_{local}x_{SV}}(n) = \sum_{i=0}^{1022} x_{local}(i+n) \cdot x_{SV}(i) \qquad \textbf{Eq. 2.18}$$

For Equation 2.18, r is the cross correlation between the local, x_{local}, and the received, x_{SV}, C/A-codes.

The Gold codes [37] used to generate GPS C/A-codes have the interesting properties of virtually no cross-correlation among codes, and having only one peak of significant strength for auto-correlation. Figure 2.13 on the next page shows the auto-correlation function of PRN 1.

Correlation is a linear process, and multiple signal components will superpose in correlation domain. The relative phasing of multipath components on the carrier level will decide how those signals will be added to the direct signal. The two worst cases are if multipath components are fully added or fully subtracted from the main signal. Figures 2.14a and 2.14b on the next page show the two corresponding correlation peaks in the presence of multipath. Thick dashed lines indicate direct signal components, dotted lines show multipath and the black solid lines are the combinations of the two. The pairs of thin dashed lines show locations of the early and late samples. The multipath component chosen in this example has a reflection coefficient of ±0.5. This would be considered a severe multipath condition, and the shape of the total correlation peaks differs significantly from the original ones (thick dashed lines).

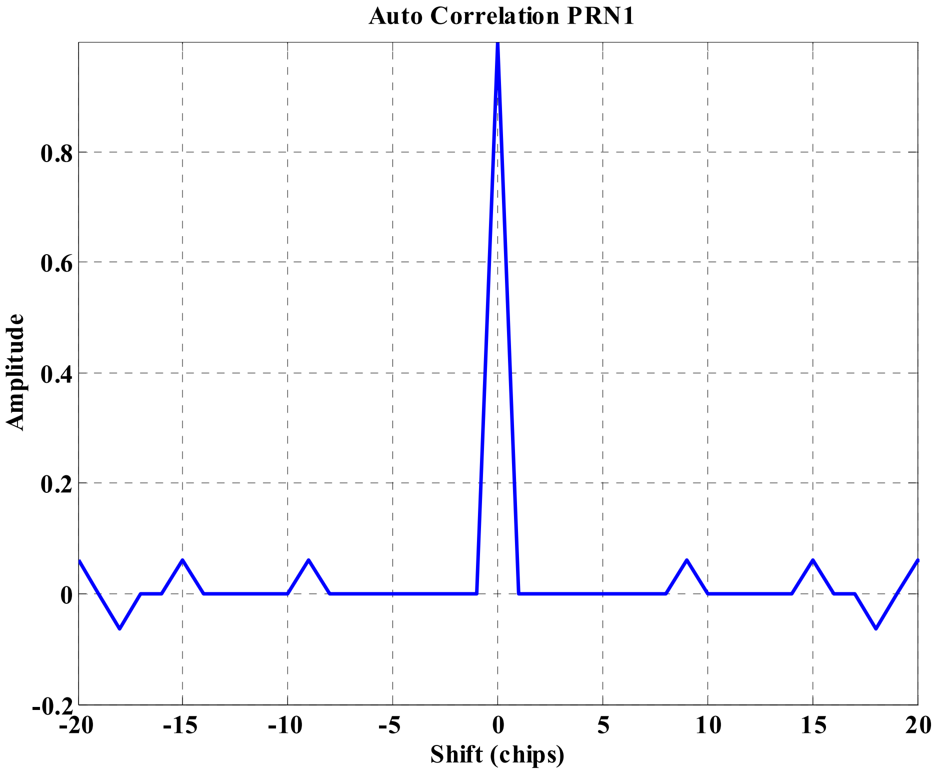

Figure 2.13 Auto-Correlation PRN 1

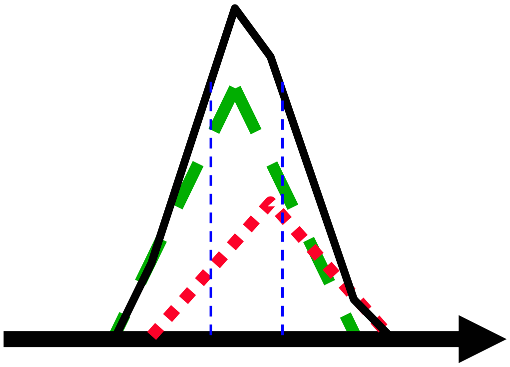

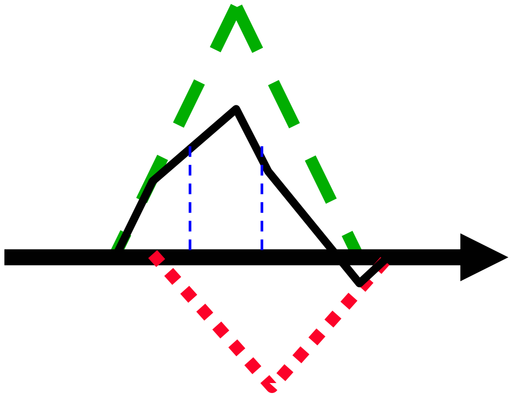

Figure 2.14a Positive Correlation Peak **Figure 2.14b Negative Correlation Peak**

We seek the worst case ranging biases introduced by multipath, as its delay is increased from zero. The next figure shows the resulting ranging errors as a multipath component of amplitude ±0.5 is swept across a direct signal.

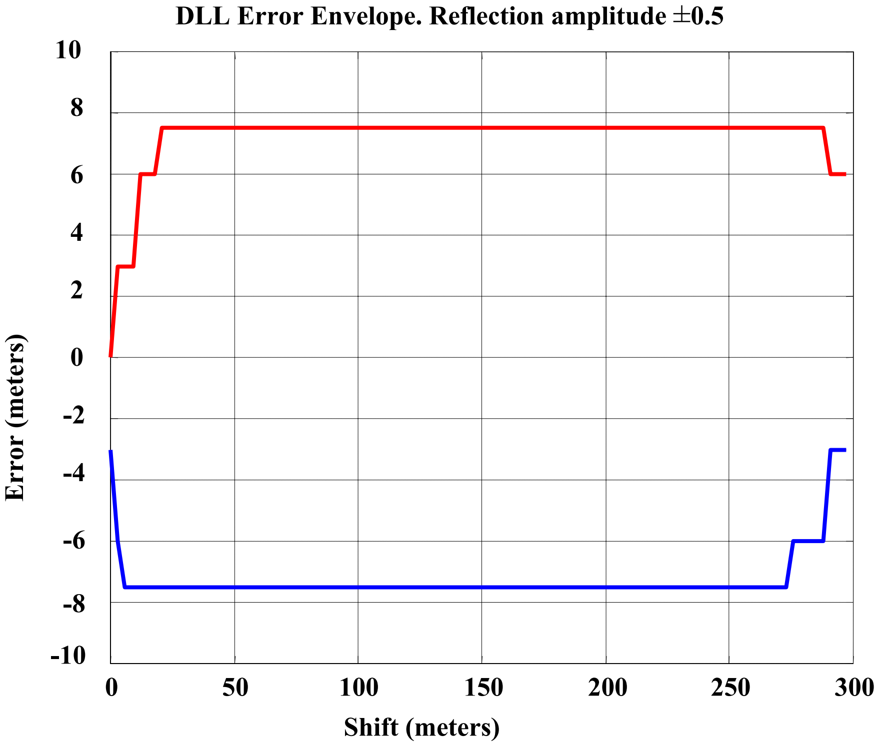

Figure 2.15 C/A-Code DLL Error Envelope

A 1/10-chip width correlator spacing between the early and late samples was used, and the worst case error is in the order of ± 8 meters. Wider correlator spacing would inflate the error envelope in Figure 2.15. This magnitude of error makes GPS code phase measurements unsuited for use with LNS.

2.4.2 GPS Carrier Phase

GPS carrier phase is generally tracked in a Phase-Locked Loop (PLL), and Figure 2.16 on the next page shows a high-level block diagram of a PLL.

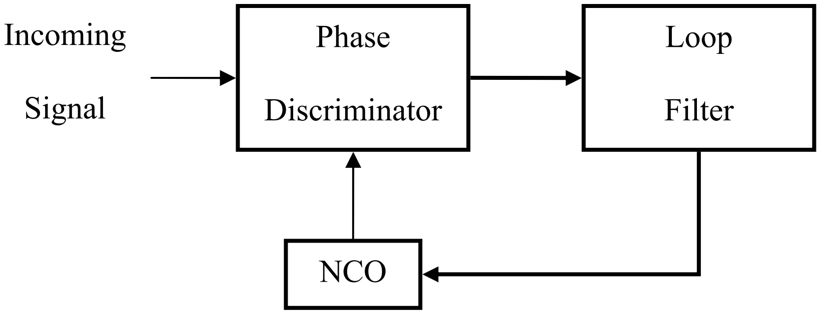

Figure 2.16 Phase Locked Loop

The three main elements of the PLL are the phase discriminator, the loop filter and the Numerically Controlled Oscillator (NCO). The phase discriminator provides a measurement of the phase offset between an incoming signal and the NCO (at IF); the loop filter sets the bandwidth for tracking loop dynamics, and the NCO tries to match its frequency to the one received from the satellite.

Phase discrimination may be done with In-phase and Quadrature-phase sampling in digital receivers. The next figure shows the relation between waveform and phase measurement.

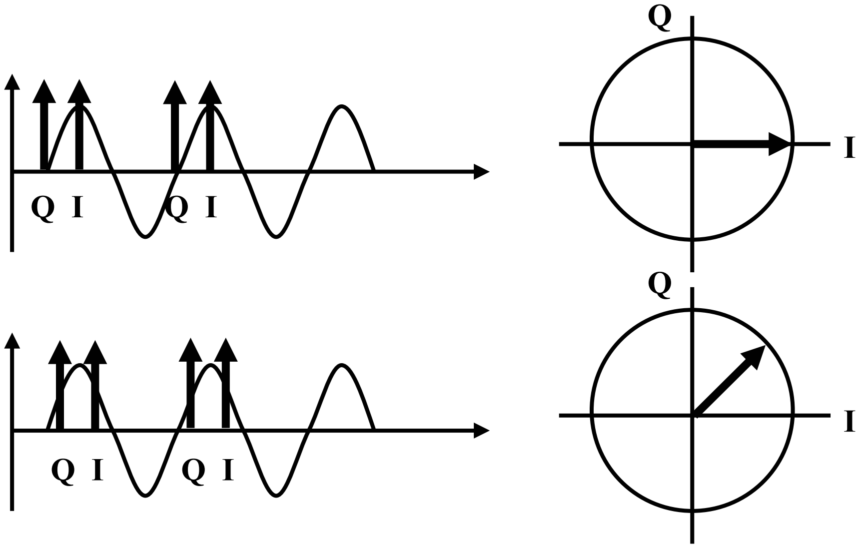

Figure 2.17 I and Q Samples with Corresponding Phasors in IQ-Plane

A 4-quadrant arctan function could be used to get the phase measurement from the IQ samples. However, receivers often use arctan look-up tables instead of spending their strained computational resources on calculating trigonometric functions [5].

Multiple signal components will add like vectors in the IQ-plane, and the figure below shows an example of how multipath, dotted arrow, adds to a direct signal, solid arrow.

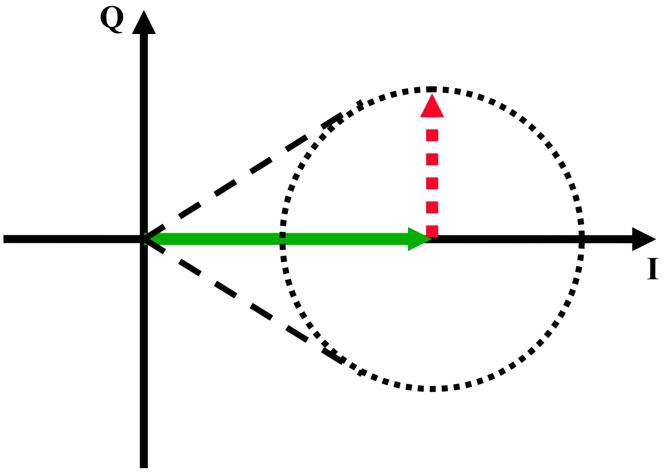

Figure 2.18 Direct and Reflected Signal in IQ-Plane

The direct signal has twice the amplitude of its reflection in the example above. Figure 2.19 on the next page shows the carrier phase error as the reflection delay sweeps through one wavelength (i.e. traverses the dotted circle in Figure 2.18). While the C/A-code error envelope will be virtually zero for multipath delays of more than the 300-m chip width, its carrier phase counterpart repeats for every additional wavelength of delay. Luckily, Figure 2.19 only shows a maximum of 1.6 cm phase error for the given case, compared to the ±8 m error for C/A-code phase.

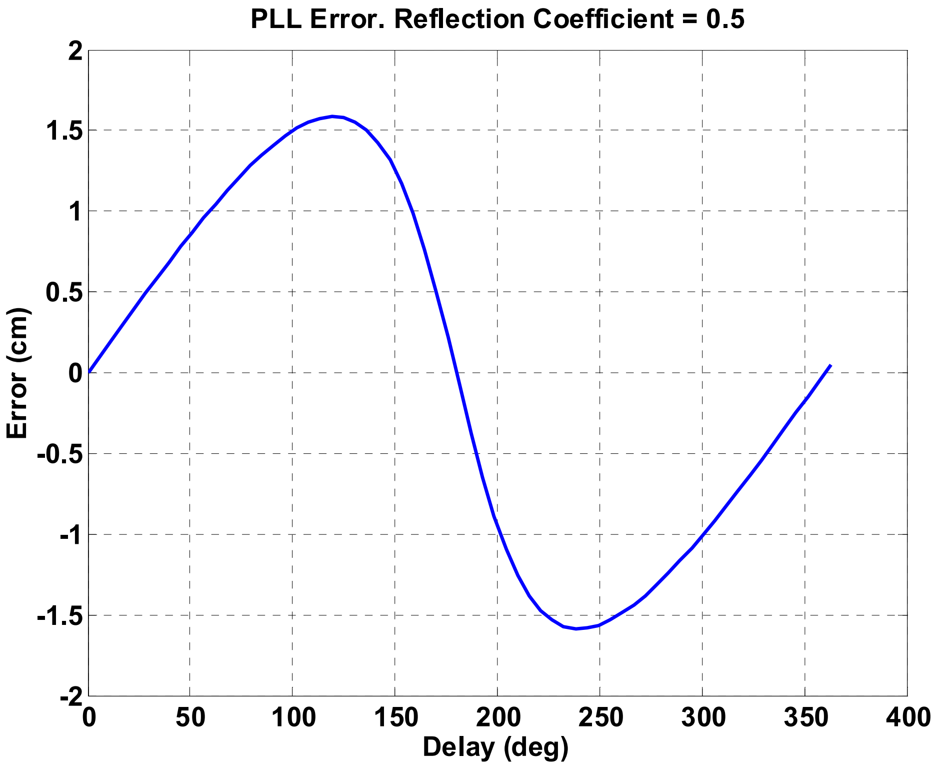

Figure 2.19 L1 Carrier Phase Error from Reflection with α = 0.5

2.4.3 UWB

UWB signals have the potential of completely rejecting multipath with delays of more than the pulse width. Figure 2.20 has a high-level block diagram of a UWB transmitter.

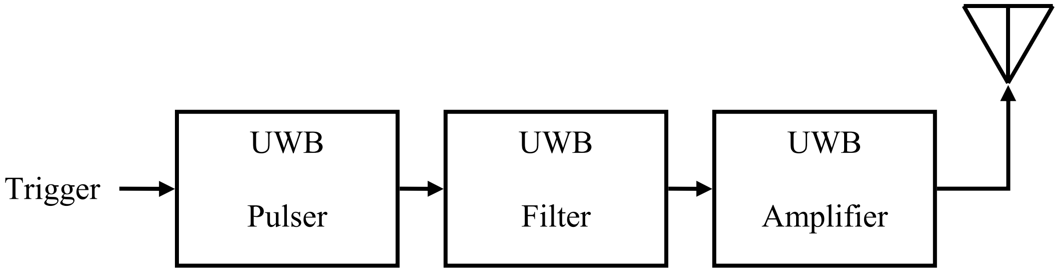

Figure 2.20 UWB Transmitter

There are few references on UWB receivers, but I suggest one possible implementation of a UWB receiver in the figure below.

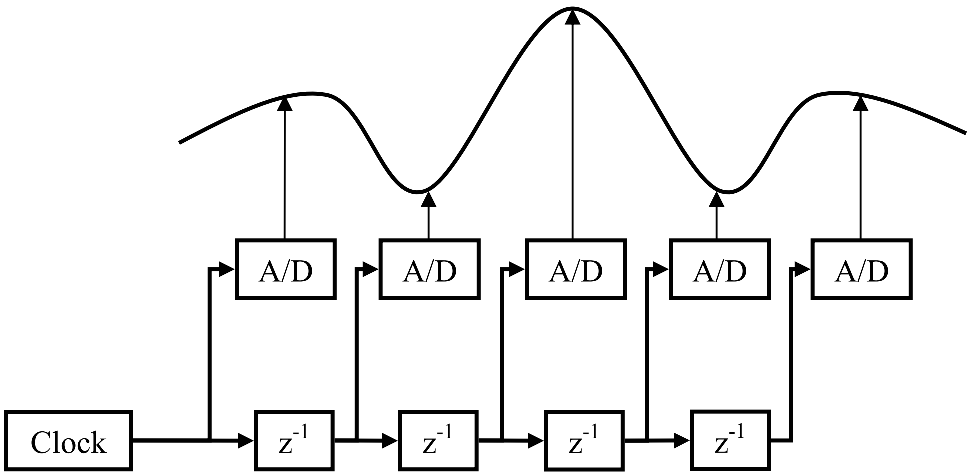

Figure 2.21 Strobe-Sampled UWB Receiver Structure

Even if there was a way to sample multi-GHz bandwidth UWB pulses directly, this would be wasteful since all the information is contained in short bursts of energy. Instead, an array of fairly inexpensive analog to digital converters (ADC) could be used. The individual ADC sample rates need only be as great as the UWB pulse-repetition-frequency (PRF). The ADC triggers would be offset in time, so the array would envelope the full span of the UWB waveform. Acquisition could be done by slewing the array across one period between pulses.

Figure 2.6 showed the shapes of a UWB pulse as it went through the different stages of a transmitter. The resulting signal shape was limited by the bandwidths of the filter and amplifier. In a similar way, we can model UWB as the impulse response of a Butterworth filter for use in our simulations.

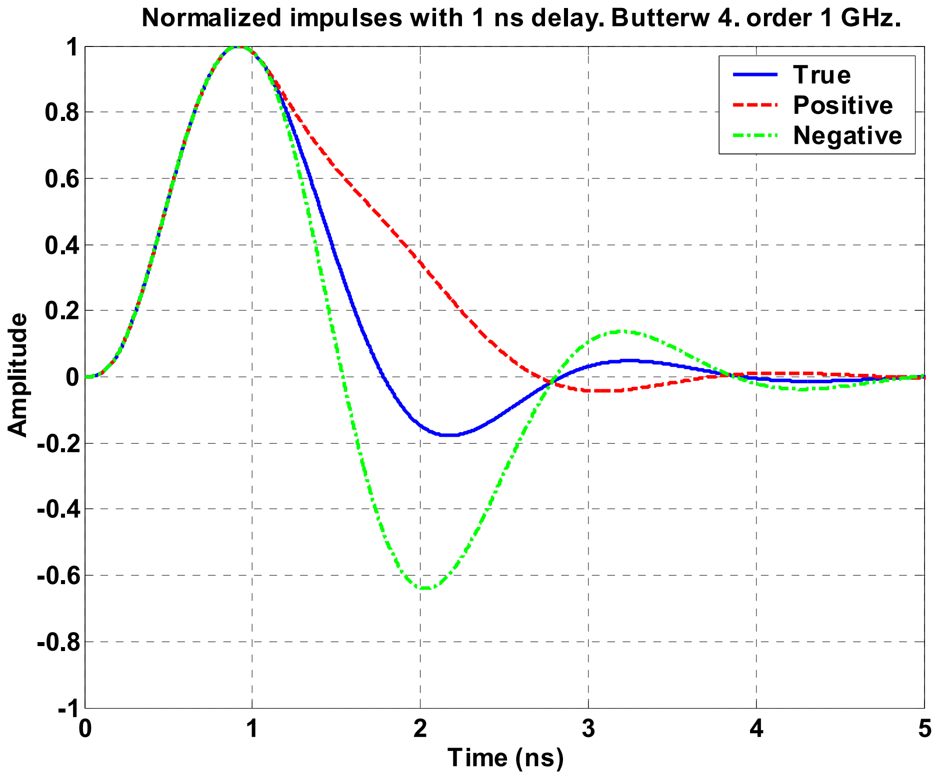

Figure 2.22 Normalized Impulse Response with Pos. and Neg. Reflections

The solid line in Figure 2.22 is the nominal impulse response of the following 4. order Butterworth filter with 1 GHz bandwidth (1 ps equivalent sampling rate).

$$\frac{6.063\text{e-}012\, z^4 + 2.425\text{e-}011\, z^3 + 3.638\text{e-}011\, z^2 + 2.425\text{e-}011\, z + 6.064\text{e-}012}{z^4 - 3.992\, z^3 + 5.975\, z^2 - 3.975\, z + 0.9918} \qquad \textbf{Eq. 2.19}$$

The dashed and dotted lines show how the combined impulse responses change in presence of multipath with 1 ns additional delay and reflection coefficients of ±0.5.

Like GPS, a UWB receiver would also be based on correlating a known waveform with a received one. This is the optimal way of detecting and tracking a signal of known shape. Figure 2.23 on the next page shows a normalized view of the correlation peaks for the impulse responses in Figure 2.22. Note how positive multipath (dashed line) delays the correlation peak, while negative multipath (dash-dotted line) advances it.

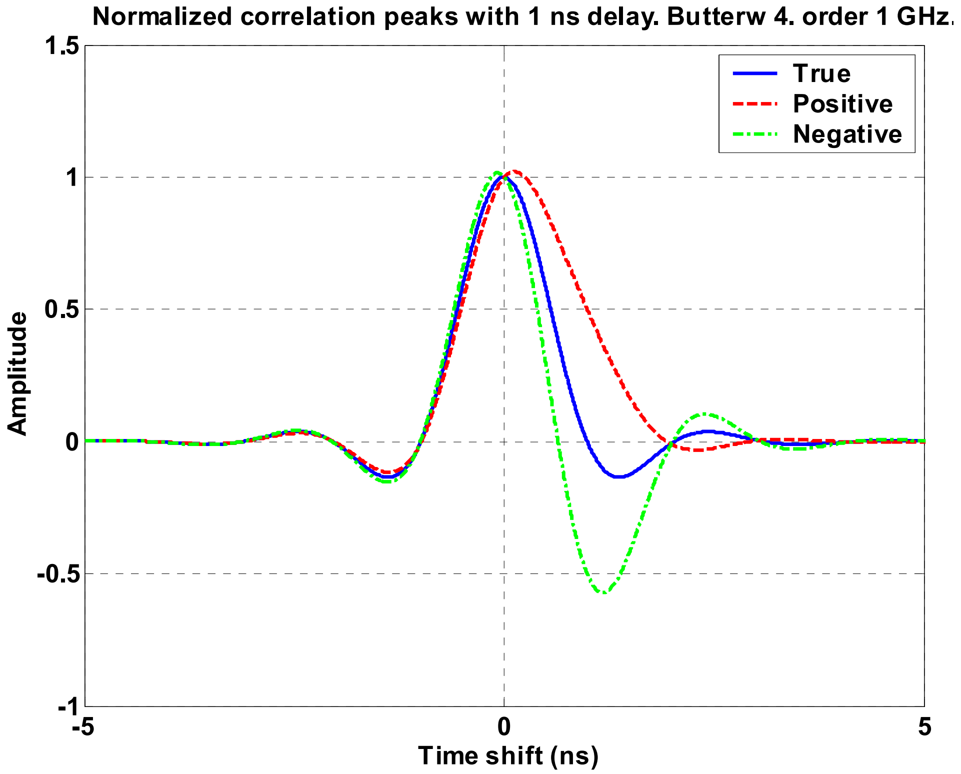

Figure 2.23 Normalized Correlation Peaks

We seek to find how the bandwidth of a signal affects its robustness towards multipath. Thus, two cases were studied in simulating multipath effects: 1 GHz and 10 GHz. A simple maximum-peak finder was used to mark arrival of the pulses. Figures 2.24a and 2.24b on the next page contain the results of the simulation for the 1 GHz and 10 GHz cases respectively. Notice the difference in spans of the two figures. All of the leftmost figure can fit inside the dashed box on the rightmost one.

The solid lines show range errors from positive reflections and the dashed lines show the resulting errors from negative ones. Whereas the 1 GHz case had maximum ranging errors of ~6 cm, the 10 GHz case only showed ~6 mm maximum errors. Furthermore, there is virtually no effect on ranging if a reflection has more than ~2 pulse-widths of delay. The jagged shape of Figure 2.24a is purely due to sampling rate artifacts.

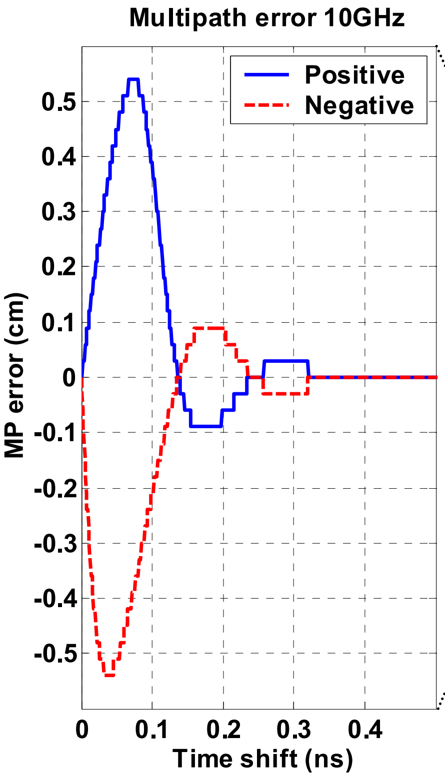

Figure 2.24a 10 GHz Case

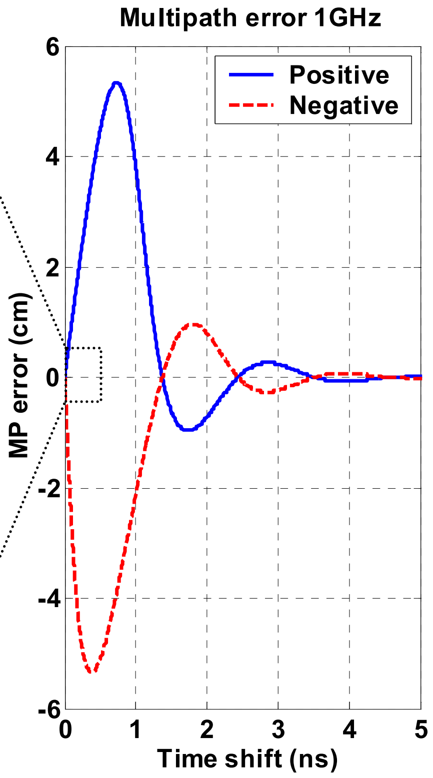

Figure 2.24b 1 GHz Case

2.5 Summary

This chapter laid down the ground rules for GPS and UWB in terms of their signal structures. GPS is based on spread-spectrum technology, with a (civilian) carrier at 1575.42 GHz. A 1.023 Mcps C/A-code is modulated on top of that carrier signal. UWB has no unified signal structure, but is classified as such if a signal has more than 0.2 fractional bandwidth or more than 500 MHz of total bandwidth. Most current uses of UWB employ pulses instead of modulating a carrier with another signal.

Signal reflections (multipath) that arrive after a direct signal may bias the cross-range measurements used in LNS. A signal reflection of half the amplitude of a line-of-sight signal may bias GPS code phase measurements by several meters if that reflection is within one chip length (~300 m) of additional delay. GPS carrier phase measurements may only be changed by a couple of cm for the same case. UWB also proves robust towards multipath, and there is a strong correlation between bandwidth and worst case multipath bias. Bandwidths of 1 and 10 GHz gave worst case errors of ~6 cm and ~6 mm respectively for the multipath scenario above.

This chapter also presented fundamental cross-range navigation equations both for GPS transceiver and UWB transponder implementations of the Leapfrog Navigation System. Linearized sets of those equations were developed for later use in solving LNS positions and analyzing LNS covariances.

~

3 The Navigation Channel

This Chapter will focus on characterizing the RF propagation environment for navigation systems. Such navigation channel models will help explain the effects of multipath reflections, which is likely the most significant error source in short-range ground-based radio-navigation (R-NAV) systems.

While Chapter 2 predicts the magnitudes of range errors for GPS and UWB given a level of multipath, Chapter 3 attempts to quantify the severity of multipath itself. Combining the two ultimately leads to bounds on ranging accuracies for GPS or UWB systems that are to operate in a given environment.

The first section of this chapter introduces metrics for modeling RF environments, and the second part looks at two common methods for measuring such navigation channels. The third and fourth sub-chapters are devoted to indoor and outdoor navigation channel measurements respectively. These tests were performed in representative environments for LNS use (rescue workers in building, or Mars exploration), and the results gave some of the parameters needed for predicting LNS positioning performance.

3.1 Metrics for Navigation Channel Modeling

A radio system is fundamentally governed by its Signal-to-Noise Ratio (SNR). Signal power will fluctuate when signal reflections with varying amplitudes and path lengths (i.e. phase) add together with a direct signal at a receiver. Such power fluctuations, or fading, have spurred much research in the area of communication systems [38,39]. The quality of a radio service can partially be described by its availability, percent of time it is up and running, and continuity, time between drop-outs. These parameters are often quantified through the statistical properties of a channel model. Several metrics used by these models have been introduced; such as average delay, delay spread and Doppler spread.

Fading can be as malevolent for communication systems (e.g. GSM) as for radio-navigation systems (e.g. GPS) due to SNR concerns. However, navigation systems are further vulnerable to multipath because it introduces biases in their fundamental ranging measurements.

In the following I will study the pertinent communication system metrics for terrestrial low-dynamics systems, as well as introduce a first-order metric for estimating range biases based on navigation channel measurements. Such ranging error estimates will be needed in later chapters for predicting total LNS range.

3.1.1 Average Delay

Average delay describes the time it takes from when a signal is transmitted until half the total power from all signal components are received at another location. Average delay can be calculated as

$$\overline{\tau} = \frac{\int_{-\infty}^{\infty} t \cdot P(t) dt}{\int_{-\infty}^{\infty} P(t) dt} \qquad \textbf{Eq. 3.1}$$

P(t) is the power delay profile and *t* is time.

Figure 3.1 shows a power delay profile (*P(t)*), with arrival time and relative power of all received signal components. The average delay is marked with the dashed vertical line in the figure.

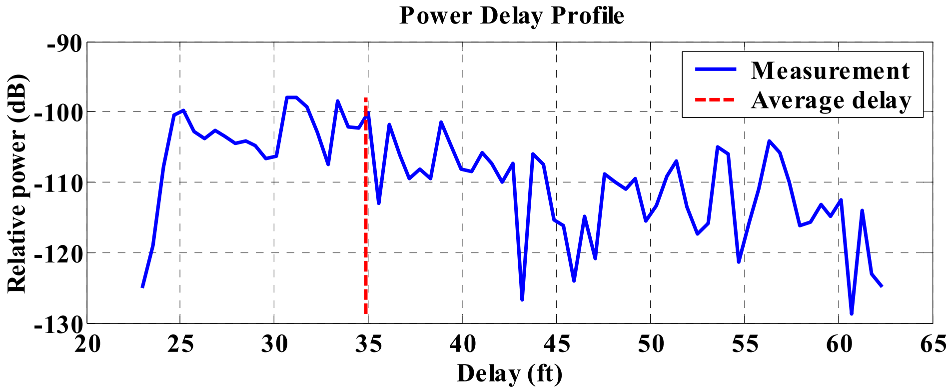

Figure 3.1 Power Delay Profile with Average Delay

3.1.2 Delay Spread

Delay spread describes the dispersion of total received power away from average delay. Delay spread tells us how smeared the received signal is in the time domain, and delay spread is calculated as.

$$\sigma = \sqrt{\frac{\int_{-\infty}^{\infty} (t - \overline{\tau})^2 \cdot P(t) dt}{\int_{-\infty}^{\infty} P(t) dt}} \qquad \textbf{Eq. 3.2}$$

P(t) is the power delay profile, *t* is time, and $\overline{\tau}$ is the average delay.

Figure 3.2 shows a power delay profile with both average delay (dashed vertical line), and delay spread (dash-dotted vertical lines).

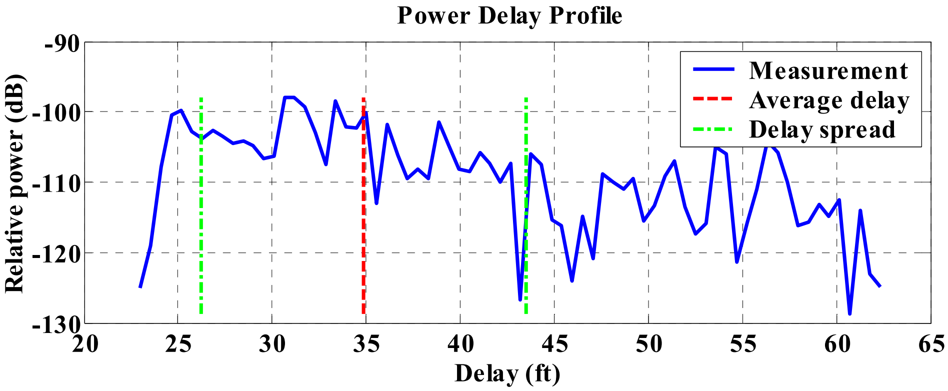

Figure 3.2 Power Delay Profile with Average Delay and Delay Spread

3.1.3 Strongest Arrival Delay

While true range is always sought in R-NAV systems, un-biased range measurements are rarely available in the presence of multipath. Ultra-severe multipath conditions may be characterized by having reflections that are stronger than the line-of-sight (LOS) signal. This could happen if e.g. a LOS path is attenuated by a wall, while a multipath component may take the "taxi cab" path through un-obstructed space. This case is shown in Figure 3.3.

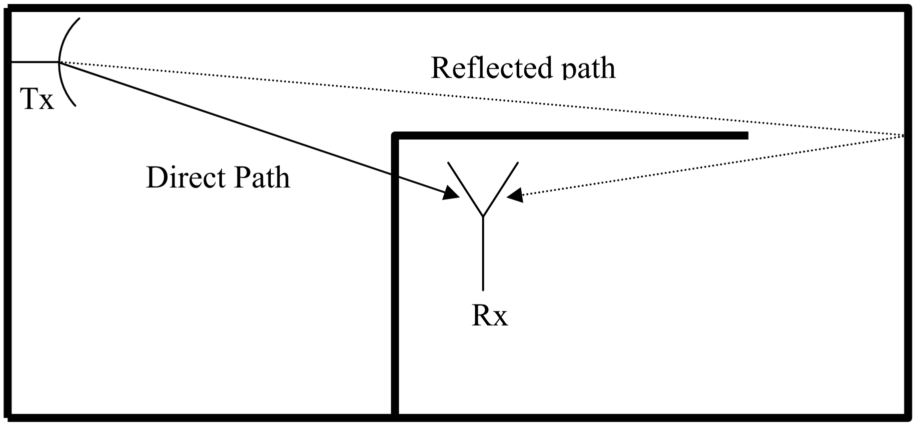

Figure 3.3 Direct and Reflected Distances

The corresponding power delay profile of the above case may look like Figure 3.4 on the next page. This figure also shows the strongest arrival delay (SAD), and it is defined as the time-delay (distance) from the LOS (true) arrival until the arrival of the strongest signal component. In Figure 3.4 the direct component arrived at 25 ft, while the strongest one occurred at 32.5 ft. Thus, the SAD is 7.5 ft.

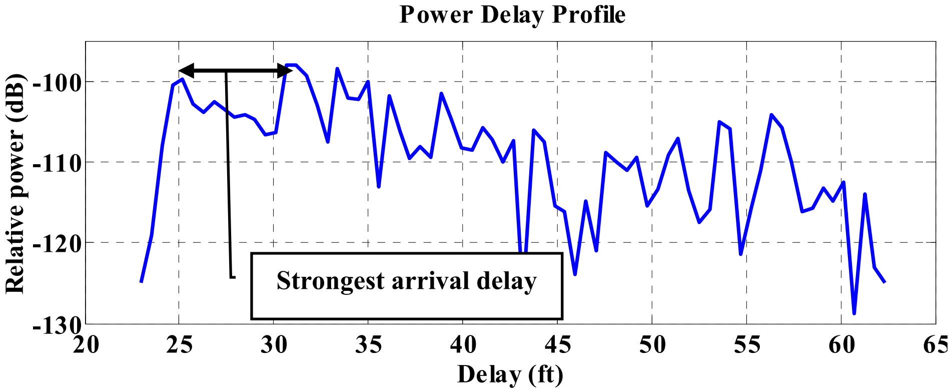

Figure 3.4 Power Delay Profile with Strongest Arrival Delay

3.2 Measuring the Navigation Channel

There are several methods for measuring RF channels [40,41], but they are in general divided into time-domain and frequency-domain methods. Time-domain techniques directly show delays and amplitudes of a line-of-sight signal and its reflections, and frequency domain ones easily show frequency selective fading. In the following we will consider both techniques.

3.2.1 Swept Carrier-Wave (CW)

This method works by sweeping a carrier signal of given power over the frequency range of interest, and measure the received signal strengths at all frequencies. Essentially, this method yields the frequency response of the given channel (propagation environment). Note that the impulse response of the channel can be generated by the inverse Fourier transform (IFT) of the frequency response.

Figure 3.5 below shows an example of a swept CW measurement.

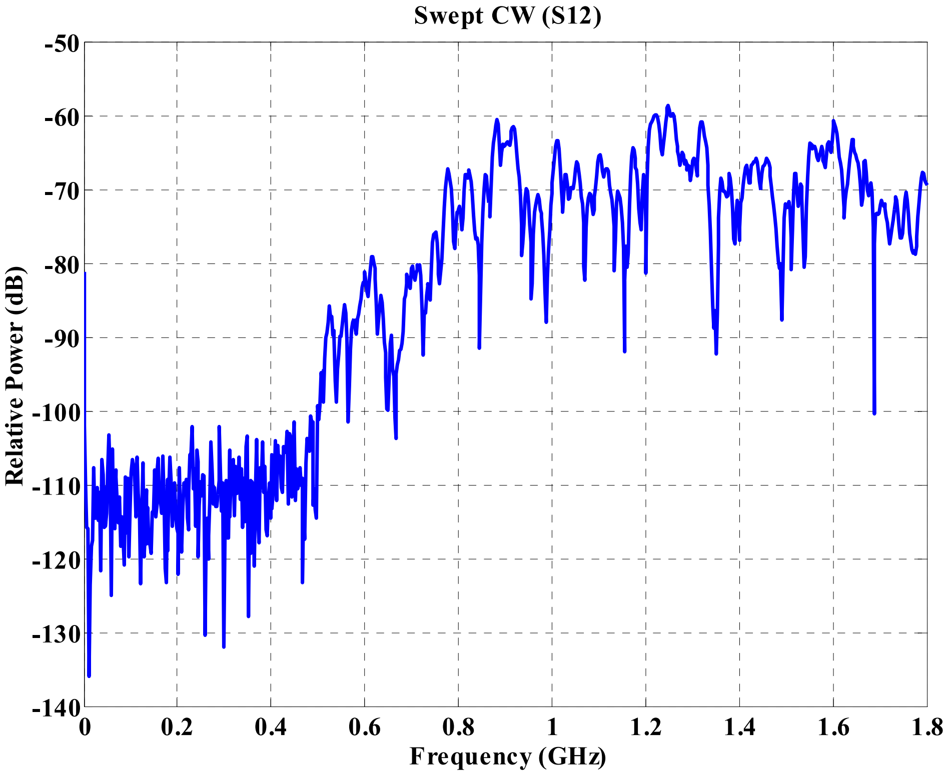

Figure 3.5 Swept CW Channel Measurement

The figure above was generated using the experimental setup shown in Figure 3.6 on the next page. An HP 4396A network analyzer with an HP 85046A 2-port S-parameter test set was used to measure the S_{12} and S_{21} transmission parameters between two UWB antennas[3]. S_{12} and S_{21} are swept CW measurements of signal transmissions from port 1 to 2 and from port 2 to 1 respectively.

---

[3] Two antennas were donated to the lab by Fantasma Networks, but no antenna specs were given. A transmission pattern for the antenna was generated off-line, and it is presented in Appendix C.

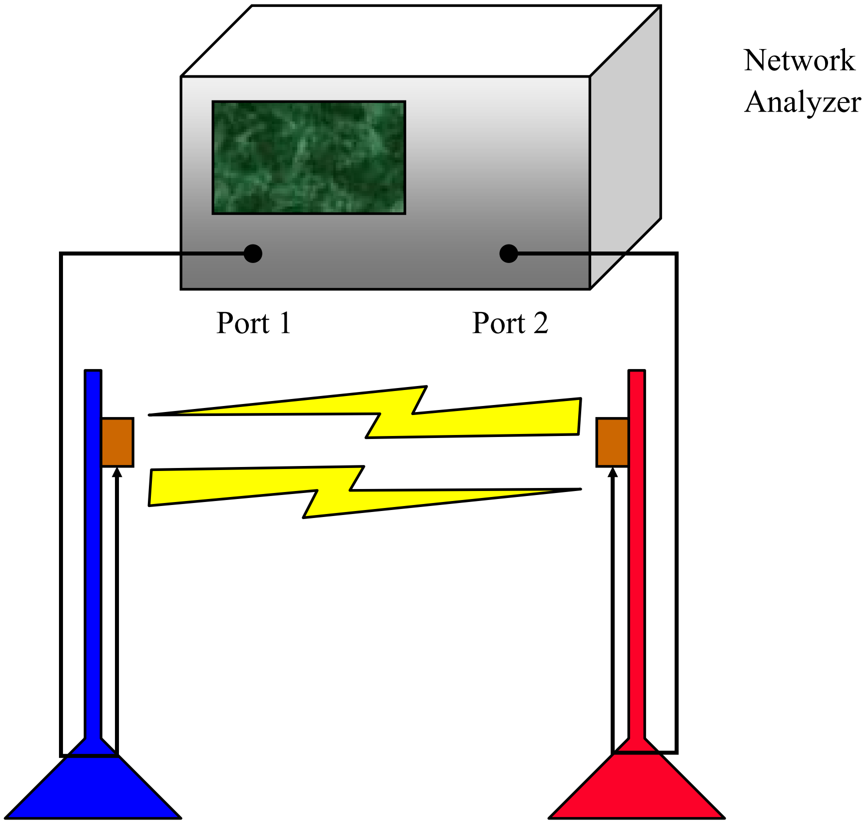

Figure 3.6 Swept CW Experimental Setup

3.2.2 UWB Sounding Pulses

Since UWB signals are very robust towards multipath, UWB is an excellent choice for actually measuring multipath. This technique works by transmitting short UWB sounding pulses and measuring arrival times and signal strengths of all signal components at a different location. In essence, this method directly generates the time-domain impulse response of a channel. Figure 3.7 on the next page shows an example of such a measurement.

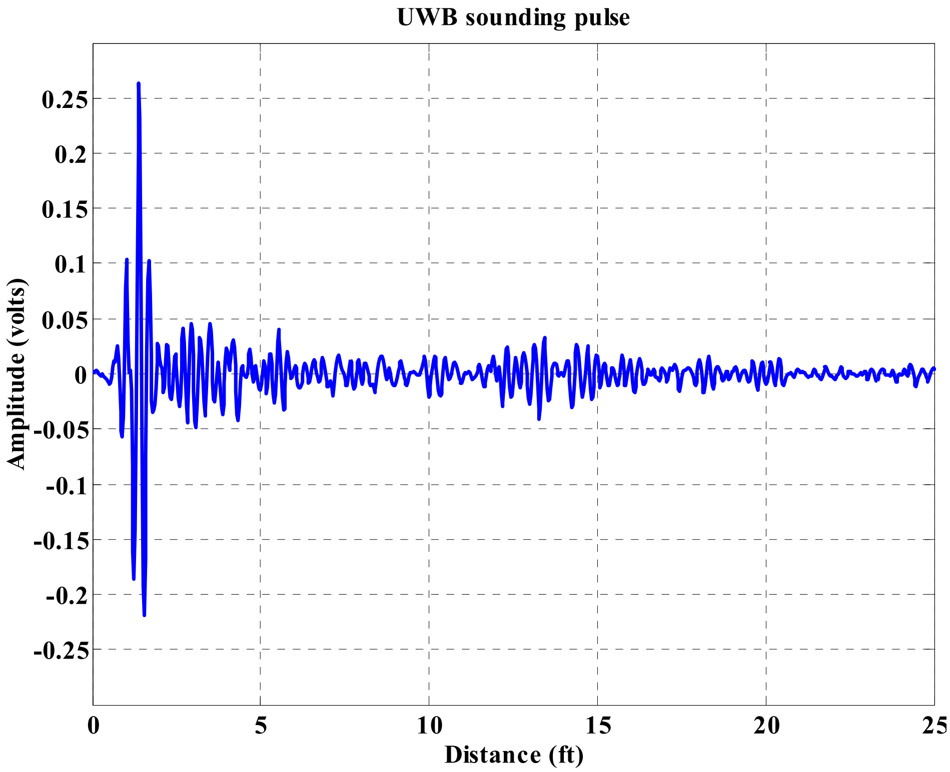

Figure 3.7 UWB Sounding Pulse Channel Measurement

Figure 3.8 below has the overview of the UWB sounding pulse experimental setup that was used to generate Figure 3.7.

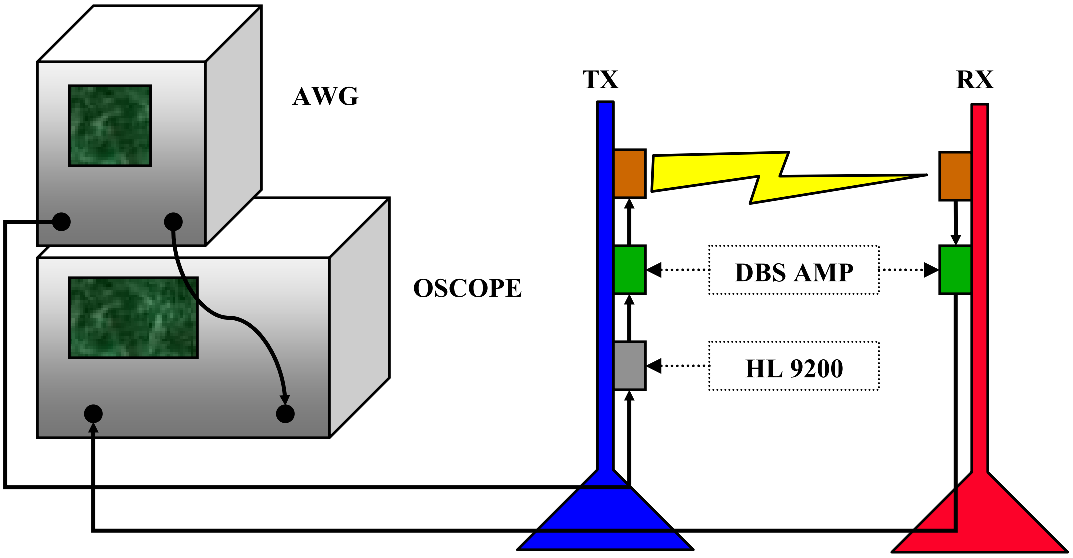

Figure 3.8 UWB Sounding Pulse Experimental Setup

Measurements of the navigation channel were generated by sending a 1 MHz trigger signal from a Tektronix 2021 Arbitrary Waveform Generator (AWG) to a HyperLabs HL 9200 UWB pulser. The pulser generated UWB waveforms, which were then sent through coax cables to a DBS-0208N220 amplifier, and finally transmitted from a UWB antenna. A similar antenna/amplifier combination was used on the receiving end, and the signal was then input to an Agilent 86100A fast sampling oscilloscope with an Agilent 54754A TDR/TDT module. The AWG provided the oscilloscope with synchronization, and it output 1350 amplitude measurements over a 40 ns time span.

3.3 Indoor Experiments

The building housing the Stanford University LAAS Laboratory was deemed an appropriate location for realistic measurements of a complex indoor multipath environment. The outside walls of the building are made of re-enforced concrete blocks, and there is a 5-inch thick wall partitioning the building. Figure 3.9 shows a top-down view of the building including projections of significant metallic objects (file cabinets, air-conditioning, shelves etc.).

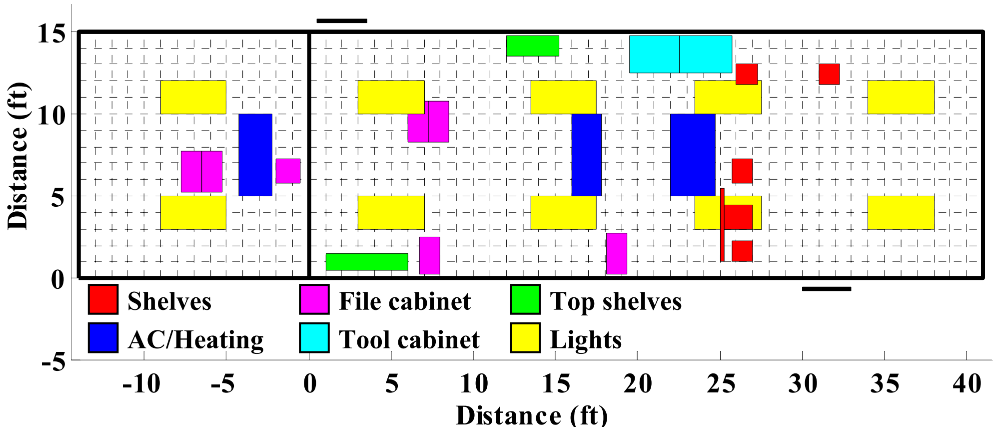

Figure 3.9 LAAS Lab with Metallic Objects

3.3.1 Experimental Setup

The indoor navigation channel at the LAAS Lab was measured using both UWB sounding pulses (Ch 3.2.2) and swept CW (Ch 3.2.1).

For the UWB sounding pulse measurement campaign, a transmit antenna was set up in the middle of the largest room of the LAAS Lab (location (20,7)), and the receive antenna (triangles) was moved around to 97 different locations all around the building. Figure 3.10 shows measurement locations at the LAAS Lab.

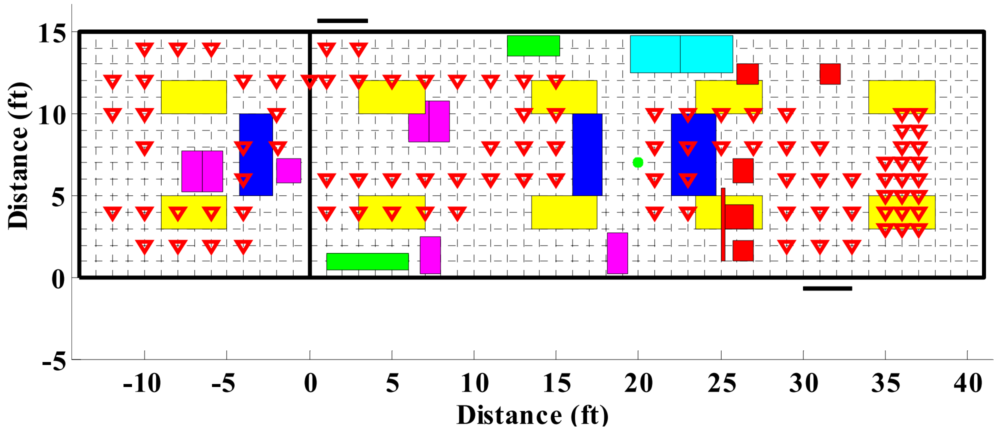

Figure 3.10 UWB Sounding Pulse Measurement Locations

Figure 3.11 show the sub-set 35 locations measured using swept CW.

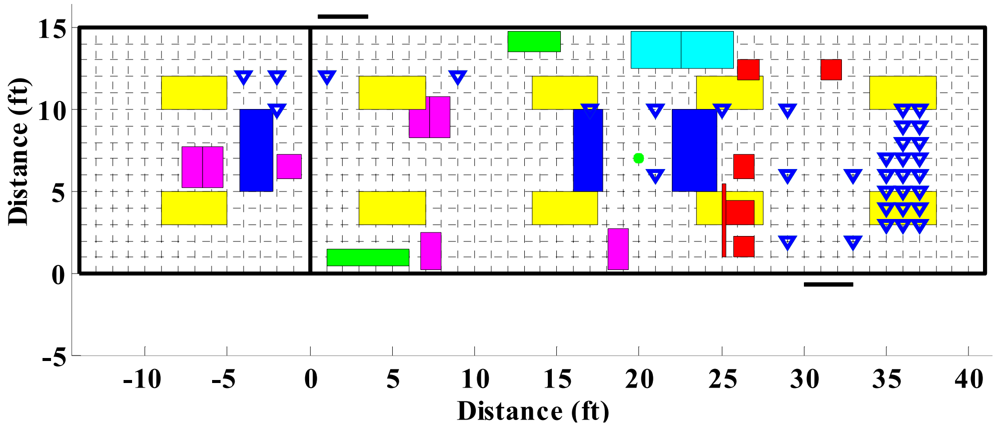

Figure 3.11 Swept CW Measurement Locations

3.3.2 Truth System

The Stanford University LAAS Lab is covered with floor tiles that measure 1 ft by 1 ft. Both antennas were mounted 4' 10" off the floor on plastic poles, and plumb bobs and wire guides were used to align the antennas with the floor tiles, as shown in the picture 3.12.

Figure 3.12 Plumb Bob and Wire Guide with Floor Tiles

Using plumb bobs and wire guides I believe my actual measurement locations to be within about 1 cm of my floor-tile truth. I compared one UWB and one CW measurement with my truth, and I used those values to calibrate out all cable biases.

3.3.3 Experimental Results

Figures 3.13 shows two sets of power delay profiles, with dashed lines for UWB sounding pulse measurements and solid lines for the CW ones.

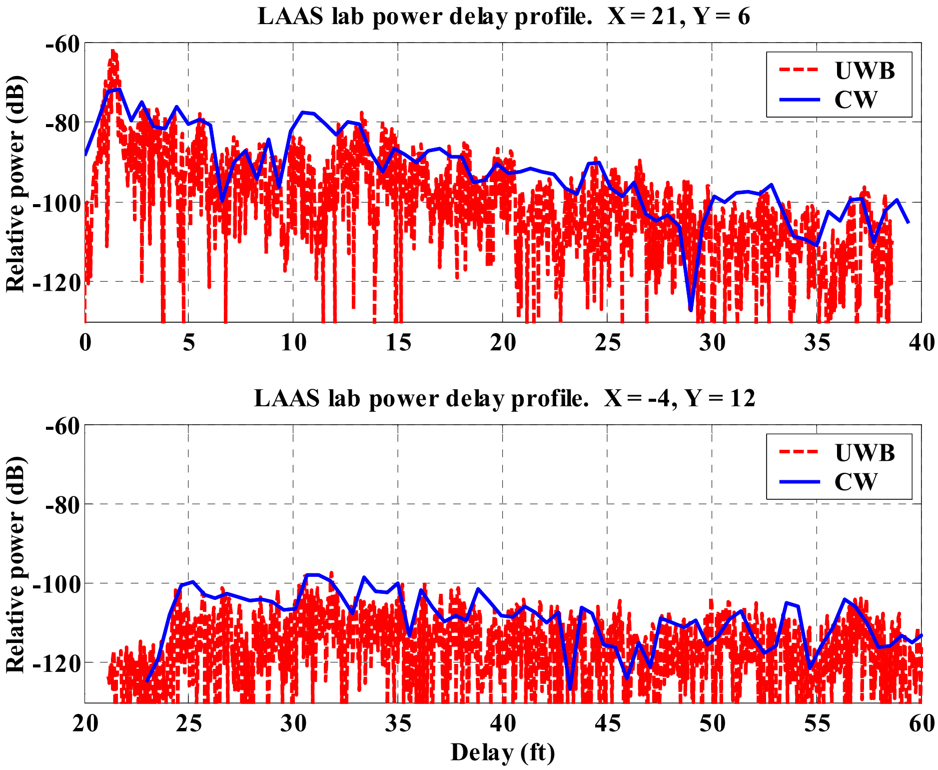

Figure 3.13 Two Power Delay Profiles

The top plot is taken 1.4 ft from the transmit antenna, while the bottom one is behind a wall 25.5 ft from the transmit antenna (note the difference in x-axis labels). The two figures show the extremes of the measurement campaign; the first has very weak multipath relative to the direct path while the other has multipath as the strongest signal component.

3.3.3.1 *Received Power vs. Distance*

In order to reduce the measurement data, total received power is plotted versus distance in Figure 3.14. This parameter was calculated by accumulating all power samples for each measurement location.

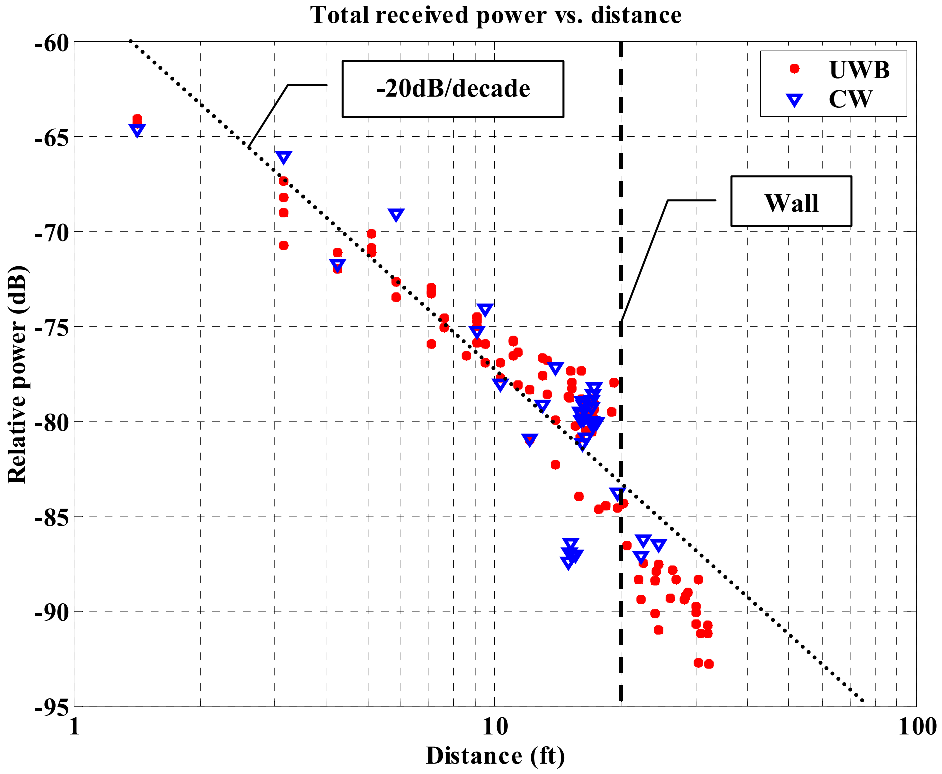

Figure 3.14 Power vs. Distance

Dots are UWB measurements, and triangles are CW measurements. The diagonal black dotted line signifies free-space loss. The general trend of the plot shows less loss than in free space, and that discrepancy is due to the addition of received signal power carried through multipath. The vertical dashed line at 20 ft shows the location of the wall, and a significant drop in received power coincides with the location of that obstacle.

3.3.3.2 *Average Delay vs. Distance*

In the next figure is plotted average delay (calibrated) as function of distance (UWB dots, CW triangles).

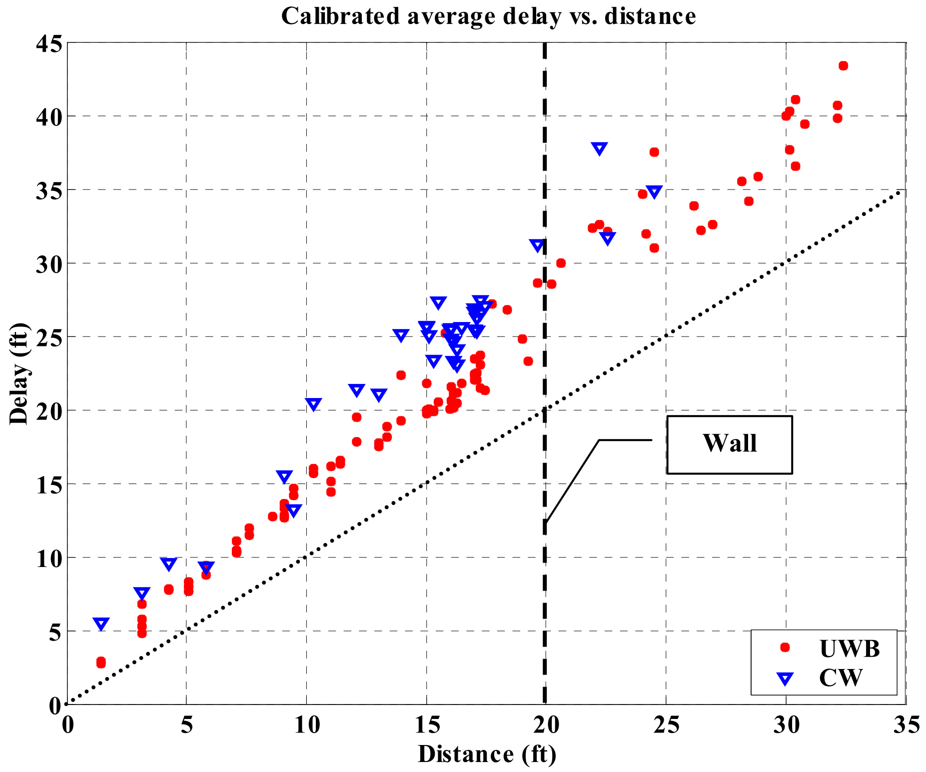

Figure 3.15 Average Delay vs. Distance

There is a linearly increasing trend in average delay deviations from the line of true distance (dotted diagonal line in the figure above). This may be explained by an ever increasing number of significant multipath arrivals as one moves farther and farther away from the transmit antenna. The slight discrepancy in the trends between the UWB and CW measurements is most likely due to differences in effective noise floors of the two equipment setups. The deviation between truth and average delay may also be used as an indicator of ranging bias due to multipath.

3.3.3.3 Delay Spread vs. Distance

The following figure gives the results for delay spread as function of distance (UWB dots, CW triangles).

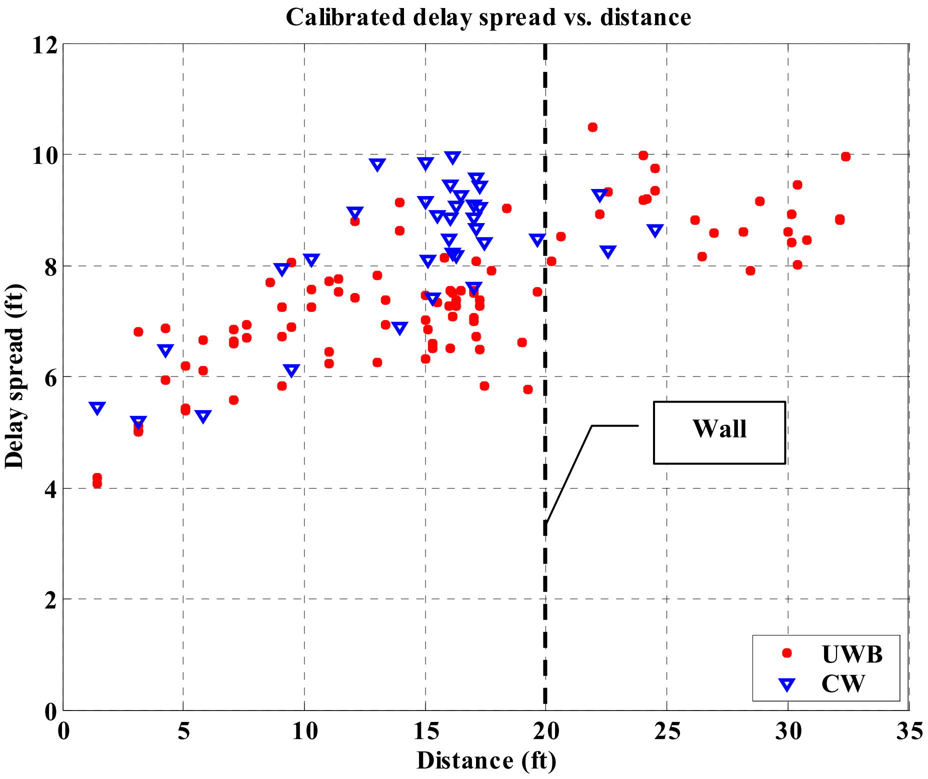

Figure 3.16 Delay Spread vs. Distance

The delay spread initially ramps up, but it approaches a constant value as the distance is increased towards 20 ft. This effect may be caused by having the direct signal amplitude approach the ones from multipath. In this case there would be "many" signals of similar amplitudes with various delays (essentially Raleigh fading). Furthermore, the delay spread has a slight increase at the location of the wall. This may be explained by noise floor issues. Transmit power for these experiments was very limited, and the measurements were only as good as the sensitivity of the instruments used.

3.3.3.4 Strongest Arrival Delay vs. Distance

Figure 3.16 shows strongest arrival delay as function of distance (UWB dots, CW triangles).

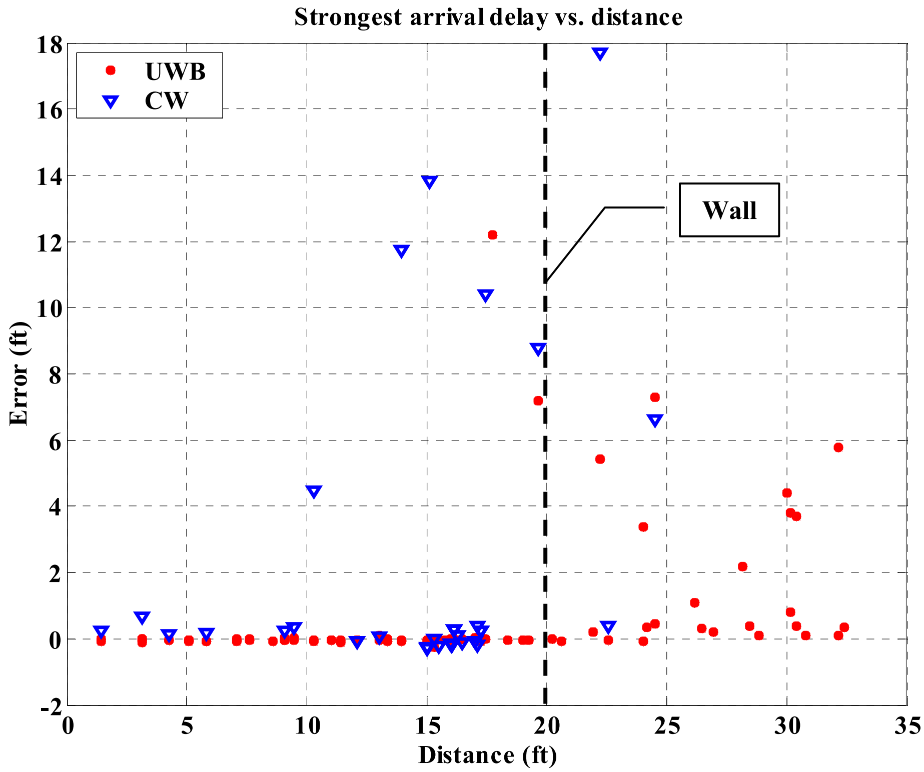

Figure 3.17 Strongest Arrival Delay

Although the most severe biases are found in the area around the wall, the frequency of significant biases generally increases with distance. Part of the reason is the fact that a signal that takes the "taxi cab" path through a door opening may be stronger than a direct signal that is attenuated by a wall. The significant strongest arrival delays in front of the wall may result from the radiation pattern of the UWB antenna. Appendix C contains a plot of that antenna pattern, which is less than isotropic. Thus, a direct signal may arrive at the antenna from a direction that has less gain than a reflected signal. Although the antenna is not isotropic, the results are still significant since a realistic antenna was used.

Since ranging systems, like GPS, tend to track whichever signal component is the strongest, the strongest arrival delay can be used as a first order estimate of ranging bias. Figure 3.17 suggests worst-case biases of almost 18 ft.

The situation for carrier phase tracking is shown in the figure below.

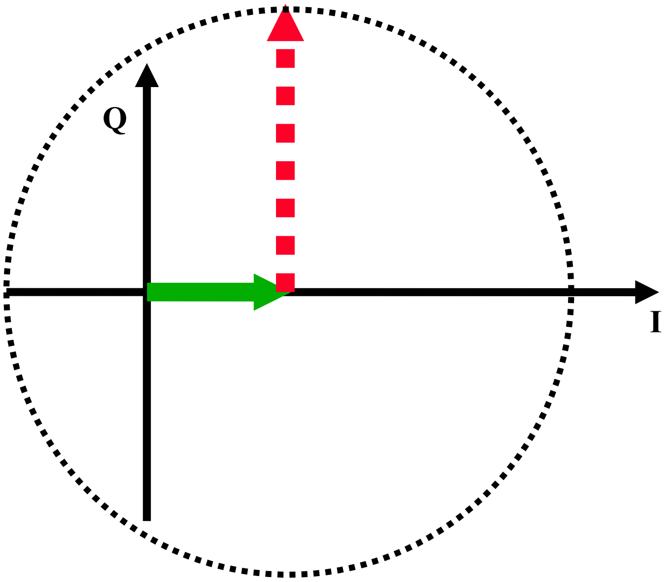

Figure 3.18 Weak Direct and Strong Reflected Signal in IQ-Plane

The solid arrow is the direct signal and the dashed arrow is the reflection. Compared to Figure 2.18 of a less harsh multipath environment there is no bound on tracking error in this case, as the signal resultant encircles the center of the IQ-plane. Since the multipath is stronger than the direct signal, this scenario is equivalent to having the "tail wag the dog."

3.4 Outdoor Experiments

For comparison with the indoor results, similar navigation channel experiments were performed on an outdoor open field. The outdoor propagation environment used was also thought to be reasonably close to what might be experienced on Mars, and the tests yielded results needed for predicting LNS performance in a Martian scenario.

3.4.1 Experimental Setup

One antenna was set up in a fixed location, while another one was moved along a straight line diagonally across the field, like shown in the figure below. The different distance markers were surveyed using a long tape measure.

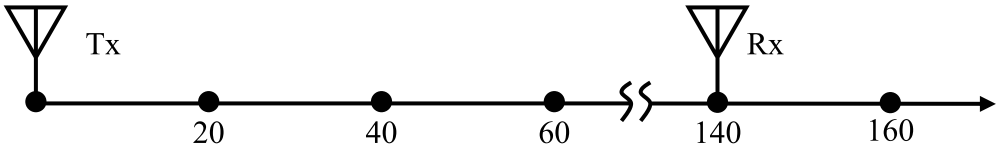

Figure 3.19 Outdoor Experimental Setup

Figure 3.20 on the next page shows a picture of the antenna setup. The navigation channel was measured using the same UWB and CW equipment as in the previous chapter, although longer coax cables had to be used. UWB sounding pulse measurements were made at 10 meter intervals up to 160 meters. This distance was limited by transmitted power levels and receiver sensitivity of the equipment in use. The CW measurements were extremely time-consuming, and they were performed in 20 meter intervals (plus one at 10 meters).

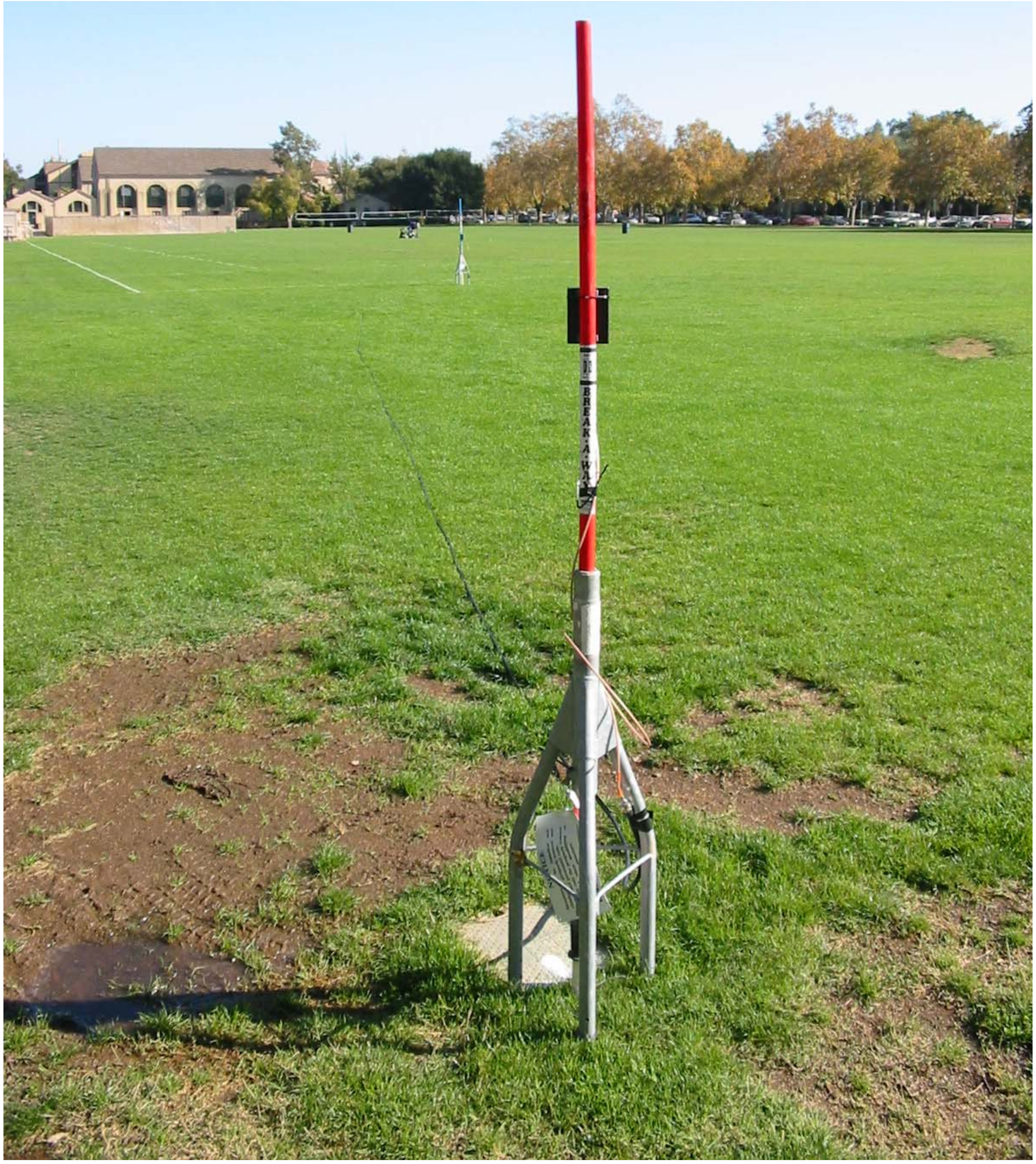

Figure 3.20 Roble Field Experimental Setup

Figure 3.21 on the next page shows raw impulse responses of the navigation channel at 10 and 160 meters.

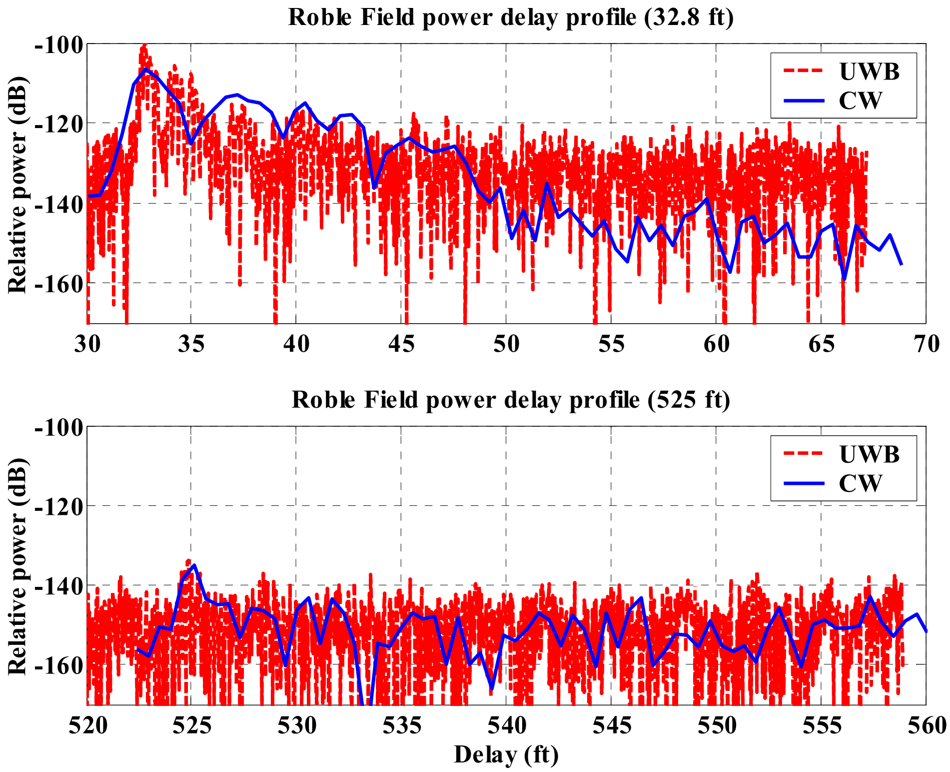

Figure 3.21 Outdoor Power Delay Profiles

The UWB sounding pulse measurements have finer detail than the CW ones. However, the UWB tests also “ring,” which eventually limit their dynamic range.

3.4.2 Experimental Results

3.4.2.1 Received Power vs. Distance

Total received power is plotted versus distance in Figure 3.22. Dots are UWB measurements and triangles are CW measurements. There is good correlation between the two measurement techniques. The diagonal black dotted line signifies free-space loss, and the trend of the plot matches $1/d^2$ fairly well. Unlike the cluttered indoor environment, the outdoor one has only one major reflection source, the ground.

However, the results indicate that the level of ground reflections is less than significant in this case.

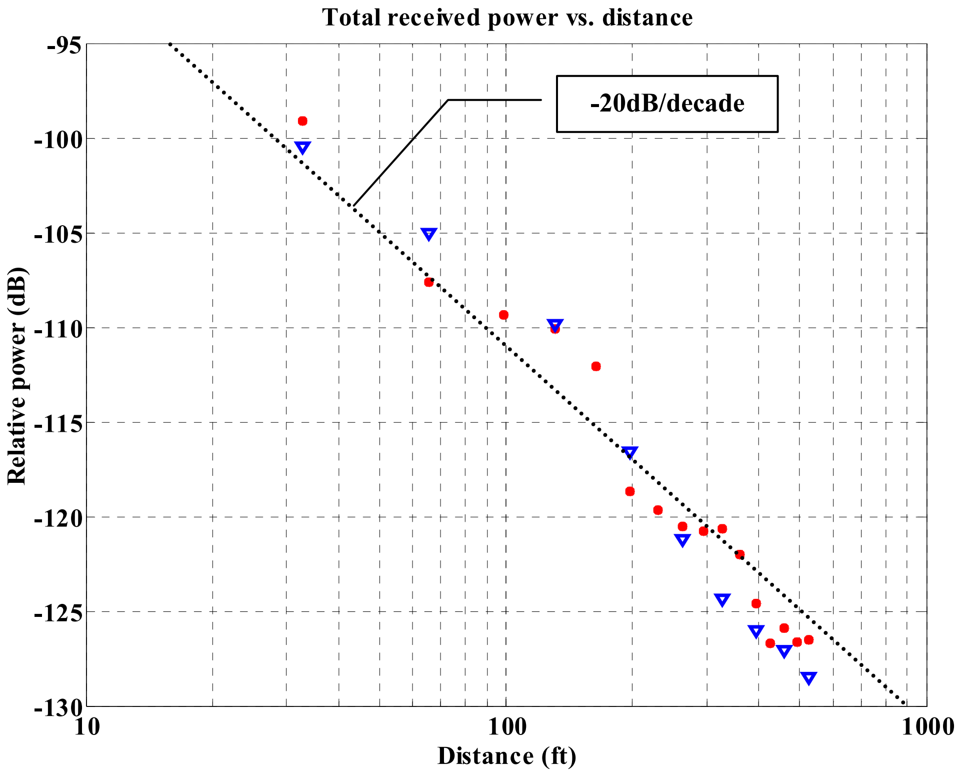

Figure 3.22 Total Received Power vs. Distance

Average Delay vs. Distance

Average delay (calibrated) is plotted vs. distance in Figure 3.23 on the next page. There is a similar linearly increasing trend in average delay difference from true delay (dotted diagonal line) as for the indoor case. However, the two cases have different physical explanation. Whereas the indoor case saw an ever increasing number of multipath arrivals with distance, the outdoor ones have signals that are gradually engulfed by the noise floor as distance increases. Eventually, there would be only noise, and the average delay would approach the value of the midpoint of the measurement span.

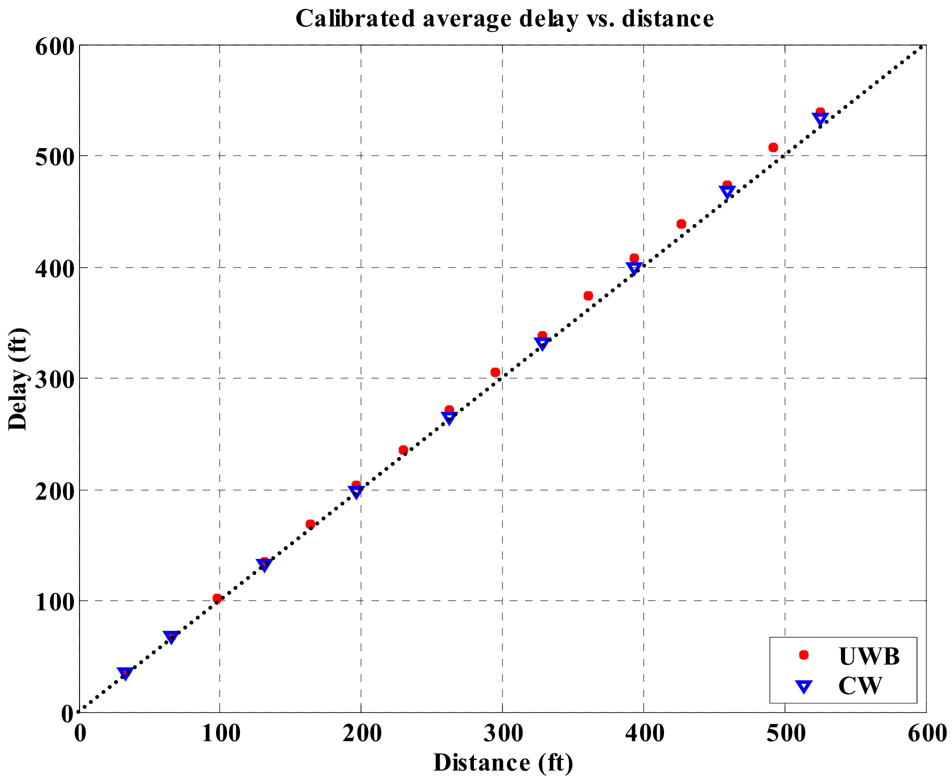

Figure 3.23 Average Delay vs. Distance

3.4.2.2 Delay Spread vs. Distance

Delay spread (calibrated) is plotted as function of distance in Figure 3.24. UWB sounding pulse measurements are plotted in red and the CW ones in blue, and there is a discrepancy between the two measurement techniques. The UWB one shows delay spread increasing linearly up to a distance of 300 ft, after which it is constant. The CW approach has DS constant up to 200 ft, then increase linearly up to 450 ft, and finally approach a constant value.

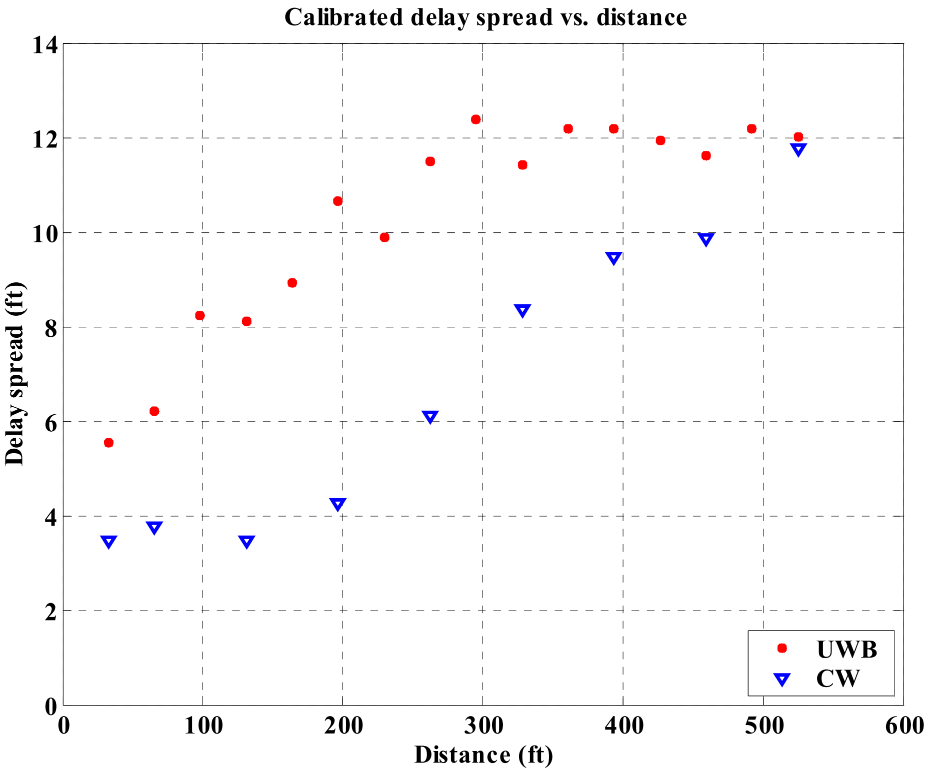

Figure 3.24 Delay Spread vs. Distance

The UWB approach has a lot of ringing in the measurements, and any peaks in the signal gradually sink into this ringing noise level. At 300 ft the peaks become insignificant relative to that noise floor. For comparison, a completely flat power delay profile over the same 40 ns span yields delay spread of 11.4 ft. This corresponds well to the ~12 ft limit in the figure above.

For the CW case, any peaks in the measurements are significantly greater than the corresponding noise floor up to 200 ft. Since such a large portion of the signal energy is concentrated in the peaks, the residual energy outside the peaks contributes marginally to the integral in Equation 3.2. However, the noise floor starts to flood the peaks at 200 ft, and they become all but washed away at 450 ft.

3.4.2.3 Strongest Arrival Delay vs. Distance

Figure 3.25 shows a plot of Strongest Arrival Delay as function of distance for the outdoor tests. The measurements at 10 m were used to calibrate cable biases, so their SADs are exactly zero. This is also the reason why some SADs appear to be less than zero.

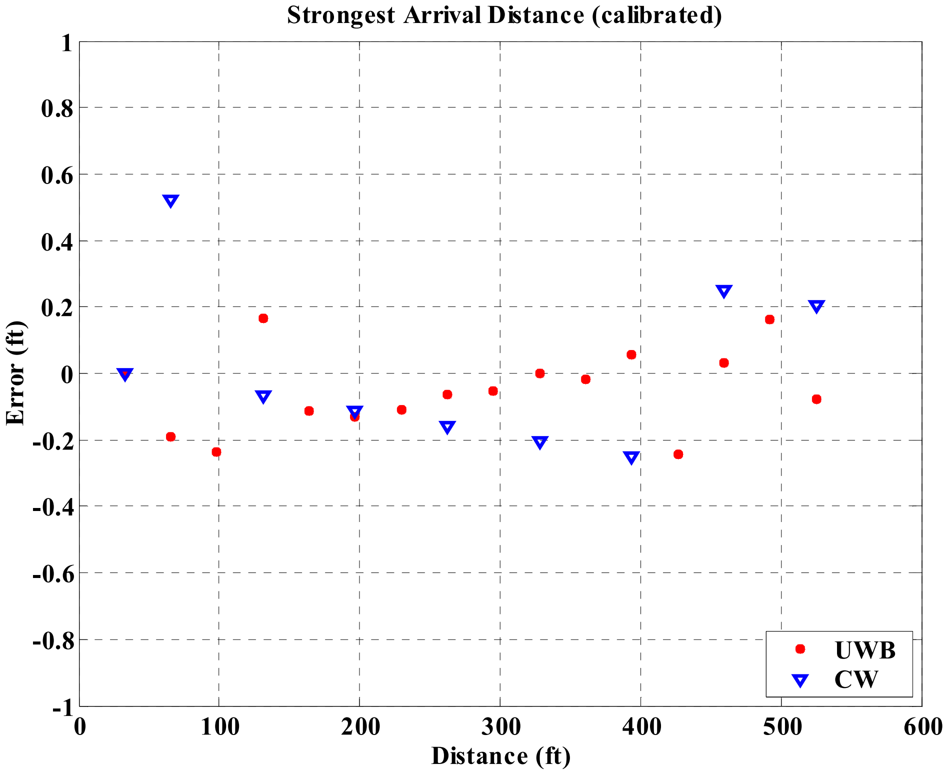

Figure 3.25 Strongest Arrival Delay (SAD)

Except for one outlier at ~66 ft distance, SAD is bounded by ± .25 ft. SAD was expected to have little variation, since the outdoor environment has more benign multipath characteristics than the indoor one tested earlier.

3.5 GPST Experiments

A set of GPS transceivers were used to measure GPS carrier phase ranging variations. Three GPSTs (T1-T3) were placed in stationary positions, and a fourth one (T4) was moved in 10m increments along a straight line up to 240 meters (~790 ft). Figure 3.26 shows the GPST setup.

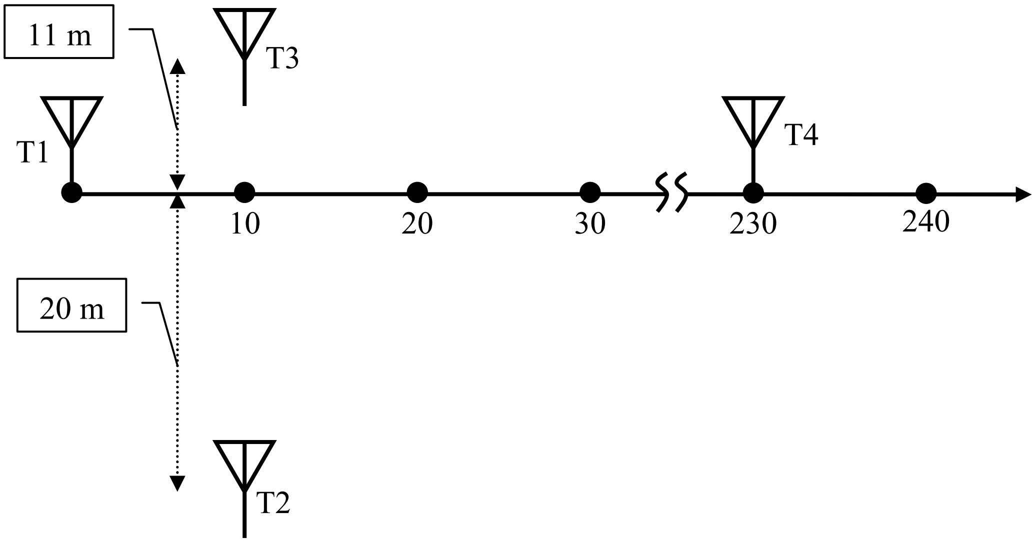

Figure 3.26 Outdoor Measurement Setup and Spacing

The measurement locations were surveyed using a regular tape measure, and excess delay (cable biases etc.) was removed from the original measurements.

GPST double-difference carrier phase standard deviations are plotted vs. distance in Figure 3.27 on the next page. The standard deviations were calculated based on 2 minutes of measurements, or ~1200 individual sample points (10Hz). Several of the cross-range measurements experienced cycle slips, but these were corrected for manually. The number of cycle slips was greatest below 200 ft and above 600 ft.

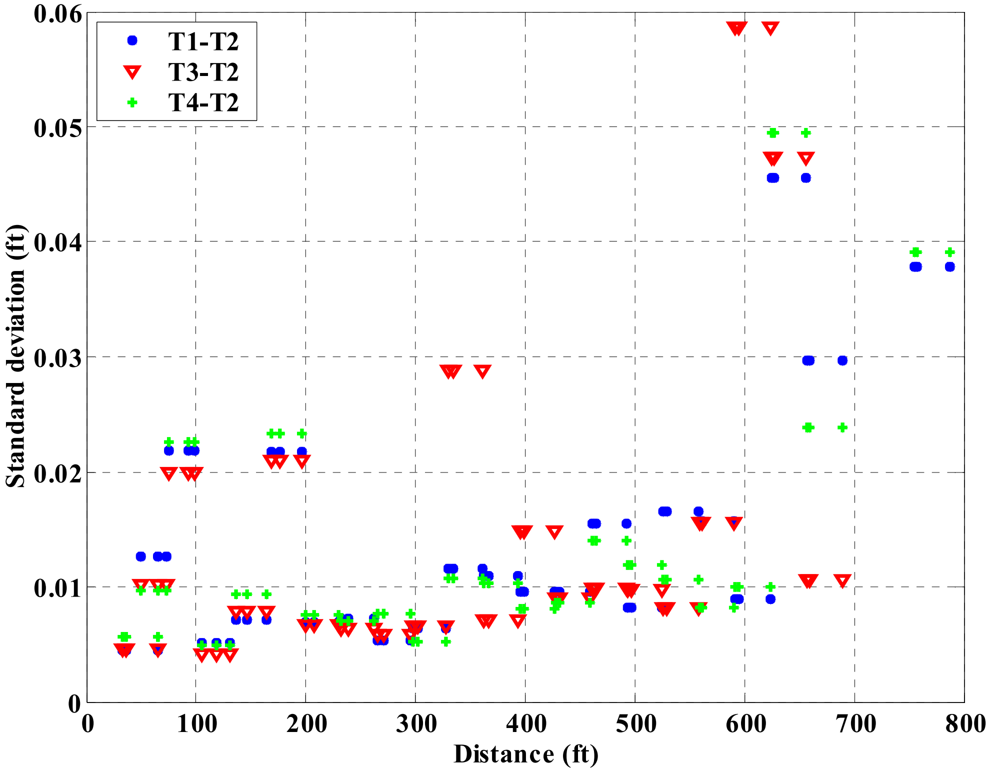

Figure 3.27 GPST Cross-Range Carrier Phase Standard Deviation

The general trend of the measurements is slightly increasing but almost constant around 0.01 ft up to a distance of 600-700 ft. Although measurements become scarce beyond 600 ft (the field was less than 800 ft across), this area indicates a general increase in standard deviation.

Variation of carrier phase measurements in the presence of white noise has the following trend [42]:

$$\operatorname{var}(\phi) \propto \frac{1}{S/N} = \frac{N}{S} \qquad \textbf{Eq. 3.3}$$

S/N is the signal-to-noise ratio. Noise terms would add linearly if the equation were to be expanded to include single or double differences.

Comparing Equation 3.3 with Figure 3.27, we conclude that the GPS receivers most likely were saturated by the pseudolite signals up to ~ 600 ft of distance. If we assume that the noise floor is constant, then SNR is constant, and so is the standard deviation (as seen in the figure). Beyond 600 ft the receivers descend into the upper ends of their dynamic ranges, and the cross-range variation begins to increase.

Although no measurements are presented beyond ~ 800 ft, we can extrapolate the effects of distance on cross-range variation in several ways.

Figure 3.22 shows that the outdoor navigation channel measurements for the same locations follow a $1/d^2$ trend (at least up to 525 ft). Thus, one option would be to use that trend in received signal power with Equation 3.3.

Another option for received signal power trend at greater distances can be found from the figure below.

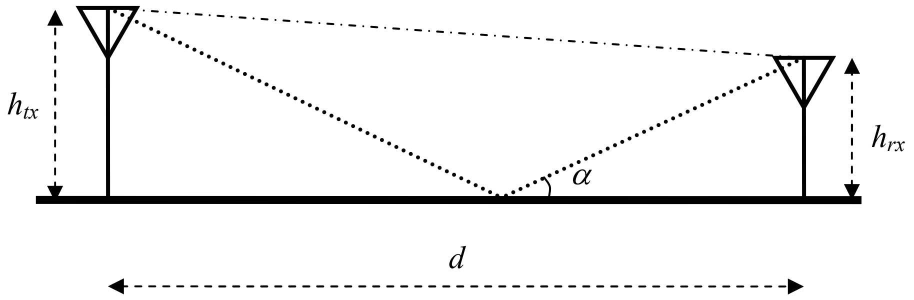

Figure 3.28 Single Reflection Model

A signal is transmitted form an antenna at height h_{tx} above ground and received at an antenna with height h_{rx}. The two antennas are separated by a distance, d, along the ground. At shallow ground reflection angles, α, the reflection coefficient of a signal will be close to -1 [42]. Equation 3.4 holds the relation between received power, antenna heights and antenna separation, and the equation is deduced in [43].

$$P_{rx} \propto \frac{h_{rx}^2 \cdot h_{tx}^2}{d^4} \qquad \textbf{Eq. 3.4}$$

In the above equation P_{rx} is received power, while h_{rx}, h_{tx}, and d correspond to the values given in Figure 3.27.

The results from the outdoor field tests and the two trends above suggest the following two models for GPST measurement variance as function of distance.

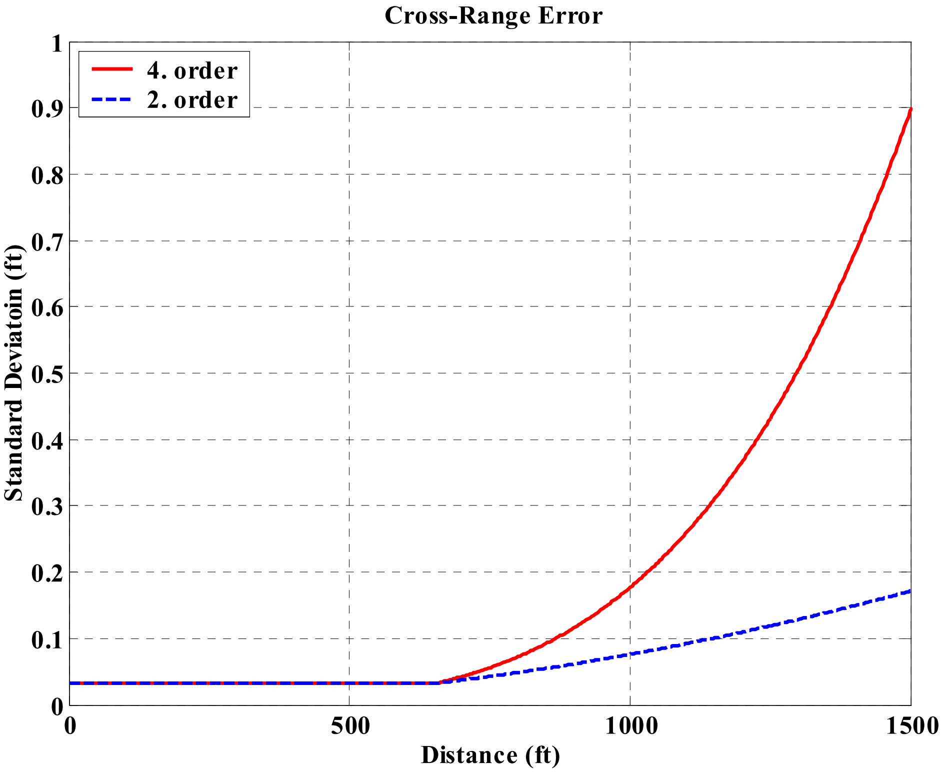

Figure 3.29 Models for Cross-Range Variation

The graphs follow the equations below, where d is distance between units and N is the model order.

$$\sigma = \begin{cases} 0.03 & \text{if } d \le 650 \text{ ft} \\ 0.03 \cdot \left(d/650 \right)^{\mathrm{N}}, \ \mathrm{N} \in \{2,4\} & \text{if } d > 650 \text{ ft} \end{cases} \qquad \textbf{Eq. 3.5}$$

The model on the previous page was based on measurements for a given set of antenna heights. Using other antenna heights would only change the location of the breakpoint of the model. Since the breakpoint most likely coincides with the point of saturation of the GPS receiver, Equations 3.3 and 3.4 can be used to infer the location of the knee in the curve for other antenna heights. As an example, doubling the antenna heights would mean doubling the distance for a given power level, i.e. the breakpoint distance would also double.

3.6 Summary

This chapter described metrics and methods for characterizing RF propagation environments, or RF/navigation channels. Sweeping a signal of given amplitude across a frequency band produces the channel frequency response. In a similar way, use of UWB sounding pulses directly generates the time-domain impulse response of a channel.

Average delay and delay spread are metrics that describe when the bulk of a transmitted signal is received and how “smeared” in time that signal is due to multipath. Additionally, the Strongest Arrival Delay (SAD) measures the time between arrivals of a direct signal and whichever signal component is the strongest. SAD is a first order measure of range bias for spread-spectrum based navigation systems. Indoor tests measured SAD values up to 18 ft, but outdoor tests only returned SAD values of less than 0.6 ft.

The results show that GPS may be less than suited for LNS use in cluttered indoor environments. GPS systems tend to track whichever signal component is the strongest, and SADs of 18 ft would result in unacceptably large cross-range errors. However, UWB systems can discern direct signals from multipath and may be attractive for indoor LNS use. The results from the outdoor experiments indicate that both GPS carrier and UWB may be used for LNS.

The outdoor navigation channel measurements and measurements of GPST cross-range variations were used to generate models for GPST accuracy as function of distance. These models will be used later in analyzing covariances of the position solutions from the Leapfrog Navigation System.

4 Leapfrog Covariance Analysis and Simulation

This chapter introduces statistical methods for analyzing the accuracy and the total range of the Leapfrog Navigation System (LNS). The linearized sets of navigation equations for GPS transceivers and UWB transponders from Chapter 2 will be used in developing the pertinent LNS covariances. Expressions for position covariances of the pre-leap, post-leap and multi-leap cases will be found.

There are two factors driving the absolute positioning accuracy of LNS: ranging accuracies (Chapter 3), and geometry. Total system range can now be predicted through simulations of representative LNS topologies, given a bound on absolute position errors.

4.1 Statistical Preliminaries

The following equation describes the covariance operation on a row-vector of random variables, $\mathbf{\Delta y}$.

$$\begin{aligned} \operatorname{var}(\mathbf{\Delta y}) &= E\left(\left(\mathbf{\Delta y}-\boldsymbol{\mu}_{\mathbf{\Delta y}}\right)\cdot\left(\mathbf{\Delta y}-\boldsymbol{\mu}_{\mathbf{\Delta y}}\right)^T\right) \\ &= E\left(\mathbf{\Delta y}\cdot\mathbf{\Delta y}^T\right)-\boldsymbol{\mu}_{\mathbf{\Delta y}}\cdot\boldsymbol{\mu}_{\mathbf{\Delta y}}^T \end{aligned} \qquad \textbf{Eq. 4.1}$$

$\boldsymbol{\mu}_{\mathbf{\Delta y}}$ is the expected-value-vector, whose elements (*i*) can be calculated as follows

$$\mu_{\Delta y_i} = E\left(\Delta y_i\right) = \int_{-\infty}^{\infty}\cdots\int_{-\infty}^{-\infty} y_i \cdot f_{\Delta y_i}\left(y_1,\cdots,y_N\right)\cdot dy_1\cdots dy_N \qquad \textbf{Eq. 4.2}$$

In Equation 4.2, $f_{\Delta y_i}$ is the probability-density-function (PDF) that describes Δy_i.

4.1.1 GPST

The notation for Equation 2.12 for GPST cross-ranges can be simplified as follows

$$\boldsymbol{\Delta}\mathbf{y} = \underset{\sim}{\mathbf{G}}_m \cdot \boldsymbol{\Delta}\mathbf{x}_m \qquad \textbf{Eq. 4.3}$$

In the above equation, $\underset{\sim}{\mathbf{G}}_m$ is the geometry matrix containing zeros and line-of-sight unit vectors at the "true" position, and $\boldsymbol{\Delta}\mathbf{x}_m$ is the vector of (clock-free) position perturbations of the mobile units. $\boldsymbol{\Delta}\mathbf{y}$ holds the differences between the calibrated measurements ($\hat{\phi}$) and the estimated distances (d_0). We assume that the calibrated measurements are unbiased, and that their means equal the estimated distances. Thus, $\boldsymbol{\Delta}\mathbf{y}$ is unbiased ($\boldsymbol{\mu}_{\boldsymbol{\Delta}\mathbf{y}} = \mathbf{0}$).

Let us apply Equation 4.1 to Equation 4.3.

$$\begin{aligned} E\left(\boldsymbol{\Delta}\mathbf{y} \cdot \boldsymbol{\Delta}\mathbf{y}^T\right) &= E\left(\left(\underset{\sim}{\mathbf{G}}_m \boldsymbol{\Delta}\mathbf{x}_m\right) \cdot \left(\underset{\sim}{\mathbf{G}}_m \boldsymbol{\Delta}\mathbf{x}_m\right)^T\right) \\ &= \underset{\sim}{\mathbf{G}}_m \cdot E\left(\boldsymbol{\Delta}\mathbf{x}_m \cdot \boldsymbol{\Delta}\mathbf{x}_m^T\right) \cdot \underset{\sim}{\mathbf{G}}_m^T \end{aligned} \qquad \textbf{Eq. 4.4}$$

We are ultimately interested in having the position errors of the rovers be a function of geometry and ranging errors, and after some algebra on Equation 4.4 we find

$$\begin{aligned} E\left(\boldsymbol{\Delta}\mathbf{x}_m \cdot \boldsymbol{\Delta}\mathbf{x}_m^T\right) &= \left(\underset{\sim}{\mathbf{G}}_m^T \underset{\sim}{\mathbf{G}}_m\right)^{-1} \underset{\sim}{\mathbf{G}}_m^T E\left(\boldsymbol{\Delta}\mathbf{y} \cdot \boldsymbol{\Delta}\mathbf{y}^T\right) \underset{\sim}{\mathbf{G}}_m \left(\underset{\sim}{\mathbf{G}}_m^T \underset{\sim}{\mathbf{G}}_m\right)^{-1} \\ &= \underset{\sim}{\mathbf{G}}_m^\dagger E\left(\boldsymbol{\Delta}\mathbf{y} \cdot \boldsymbol{\Delta}\mathbf{y}^T\right)\left(\underset{\sim}{\mathbf{G}}_m^\dagger\right)^T \end{aligned} \qquad \textbf{Eq. 4.5}$$

$\underset{\sim}{\mathbf{G}}_m^\dagger = \left(\underset{\sim}{\mathbf{G}}_m^T \underset{\sim}{\mathbf{G}}_m\right)^{-1} \underset{\sim}{\mathbf{G}}_m^T$ is the pseudo-inverse of matrix $\underset{\sim}{\mathbf{G}}_m$.

Furthermore, if all ranging measurements are uncorrelated but have the same variance (σ_m^2), Equation 4.5 condenses in the following way:

$$\begin{aligned} E\left(\Delta\mathbf{x}_m \cdot \Delta\mathbf{x}_m^T\right) &= \left(\underset{\sim}{\mathbf{G}}{}_m^T \underset{\sim}{\mathbf{G}}{}_m\right)^{-1} \underset{\sim}{\mathbf{G}}{}_m^T \cdot \underset{\sim}{\mathbf{I}} \cdot \sigma_m^2 \cdot \underset{\sim}{\mathbf{G}}{}_m \left(\underset{\sim}{\mathbf{G}}{}_m^T \underset{\sim}{\mathbf{G}}{}_m\right)^{-1} \\ &= \left(\underset{\sim}{\mathbf{G}}{}_m^T \underset{\sim}{\mathbf{G}}{}_m\right)^{-1} \cdot \sigma_m^2 \\ &= \mathbf{DOP} \cdot \sigma_m^2 \end{aligned} \tag*{\textbf{Eq. 4.6}}$$

In Equation 4.6 **DOP** is the dilution-of-precision (DOP) matrix. Looking at the elements along the diagonal of Equation 4.6 for a 2-D 4-unit case, we find that

$$\begin{aligned} &\begin{bmatrix} \sigma_{\Delta x_{m_1}}^2 & . & . & . \\ . & \sigma_{\Delta y_{m_1}}^2 & . & . \\ . & . & \sigma_{\Delta x_{m_2}}^2 & . \\ . & . & . & \sigma_{\Delta y_{m_2}}^2 \end{bmatrix} = \\ &= \begin{bmatrix} X_1 DOP^2 & . & . & . \\ . & Y_1 DOP^2 & . & . \\ . & . & X_2 DOP^2 & . \\ . & . & . & Y_2 DOP^2 \end{bmatrix} \cdot \sigma_m^2 \end{aligned} \tag*{\textbf{Eq. 4.7}}$$

Thus, dilution-of-precision acts as an "error amplification" term between fundamental ranging error and position accuracy.

4.1.2 UWB Transponder

Equation 2.15 may be formulated as

$$\Delta\mathbf{y} - \boldsymbol{\delta} = \underset{\sim}{\mathbf{G}}{}_m \cdot \Delta\mathbf{x}_m \tag*{\textbf{Eq. 4.8}}$$

$\Delta\mathbf{y}$ holds the differences between the averaged measurements (φ) and the estimated distances (d_0) and δ is a vector of processing delays. $\underset{\sim}{\mathbf{G}}{}_m$ and $\Delta\mathbf{x}_m$ are identical to those in Equation 4.3.

We will apply Equation 4.1 to Equation 4.8

$$
\begin{aligned}
E\left(\left(\Delta\mathbf{y}-\boldsymbol{\delta}\right)\cdot\left(\Delta\mathbf{y}-\boldsymbol{\delta}\right)^{T}\right) &= E\left(\left(\underset{\sim}{\mathbf{G}}_{m}\Delta\mathbf{x}_{m}\right)\cdot\left(\underset{\sim}{\mathbf{G}}_{m}\Delta\mathbf{x}_{m}\right)^{T}\right) \\
&= \underset{\sim}{\mathbf{G}}_{m}\cdot E\left(\Delta\mathbf{x}_{m}\cdot\Delta\mathbf{x}_{m}^{T}\right)\cdot\underset{\sim}{\mathbf{G}}_{m}^{T}
\end{aligned}
\qquad \textbf{Eq. 4.9}
$$

Assume that $\Delta\mathbf{y}$ and δ are uncorrelated, but have equal biases (for algebraic simplicity).

$$
\begin{aligned}
E\left(\Delta\mathbf{x}_{m}\cdot\Delta\mathbf{x}_{m}^{T}\right) &= \underset{\sim}{\mathbf{G}}_{m}^{\dagger}E\left(\Delta\mathbf{y}\cdot\Delta\mathbf{y}^{T}\right)\left(\underset{\sim}{\mathbf{G}}_{m}^{\dagger}\right)^{T}+\underset{\sim}{\mathbf{G}}_{m}^{\dagger}E\left(\boldsymbol{\delta}\cdot\boldsymbol{\delta}^{T}\right)\left(\underset{\sim}{\mathbf{G}}_{m}^{\dagger}\right)^{T} \\
&= \underset{\sim}{\mathbf{G}}_{m}^{\dagger}\left[E\left(\Delta\mathbf{y}\cdot\Delta\mathbf{y}^{T}\right)+E\left(\boldsymbol{\delta}\cdot\boldsymbol{\delta}^{T}\right)\right]\left(\underset{\sim}{\mathbf{G}}_{m}^{\dagger}\right)^{T}
\end{aligned}
\qquad \textbf{Eq. 4.10}
$$

Equation 4.10 shows that UWB transponder position solutions both depend on variation in the cross-range measurements and on variation in the transponder processing delay. This latter term is the only structural difference between Equation 4.10 for UWB transponders and Equation 4.5 for GPS transceivers. In the GPS case, processing delays are compounded with the user clock bias terms, which are removed for GPSTs.

4.2 Pre-Leap Covariance

We will consider a case where two stationary (solid red) GPS transceivers are placed side by side with a pair of mobile ones (striped green). These rovers are then moved in parallel away from the stationary units, as shown in Figure 4.1.

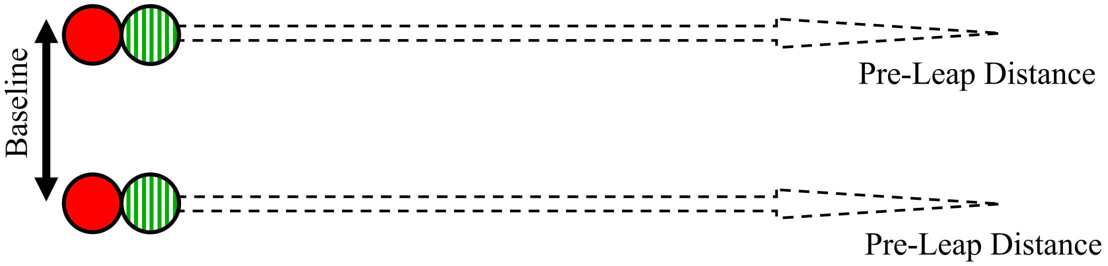

Figure 4.1 Pre-Leap Covariance Setup

Dilution-of-precision of the two mobile units will be the same by symmetry, and Across-DOP (baseline direction in Figure 4.1), Along-DOP (pre-leap direction in Figure 4.1), and HDOP are plotted in the next figure.

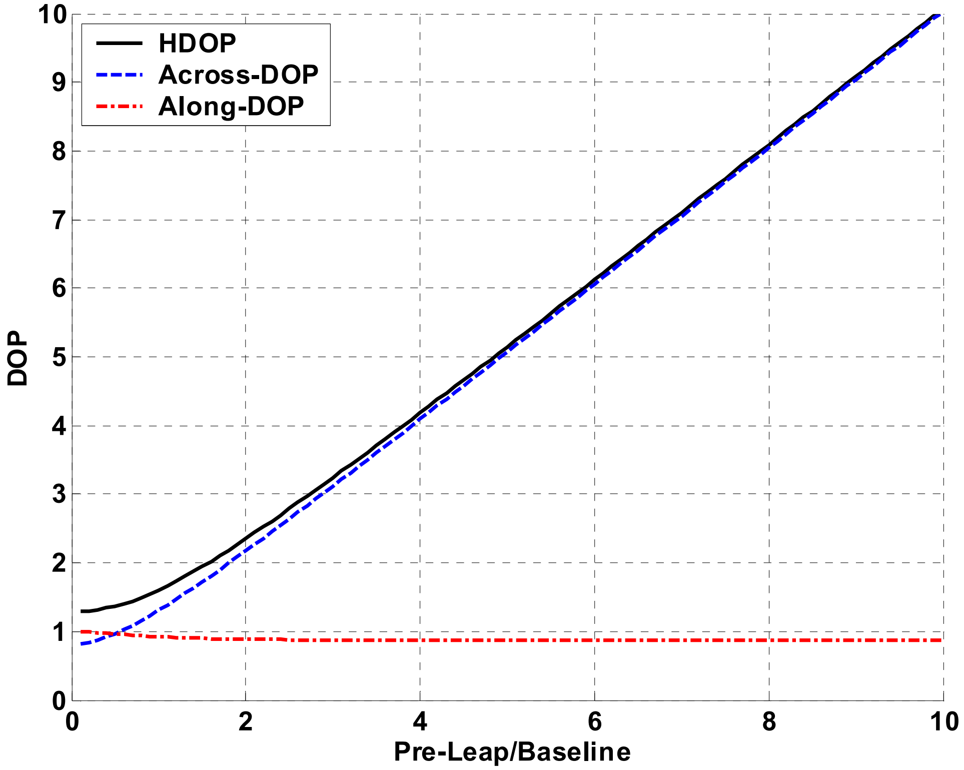

Figure 4.2 Dilution-of-Precision vs. Pre-Leap/Baseline Distance

We notice that the DOP component along the direction of travel hardly changes with the normalized pre-leap distance. Across-DOP, however, asymptotically approaches a constant gradient. The above effects may be better understood by looking at error ellipses for intersecting wave fronts from the two GPS transceivers (T_1, T_2) in Figure 4.3. The dashed lines show expected values for the cross-ranges at two different locations, and the dotted lines signify measurement variations. Error ellipses can be quickly sketched based on the intersecting lines.

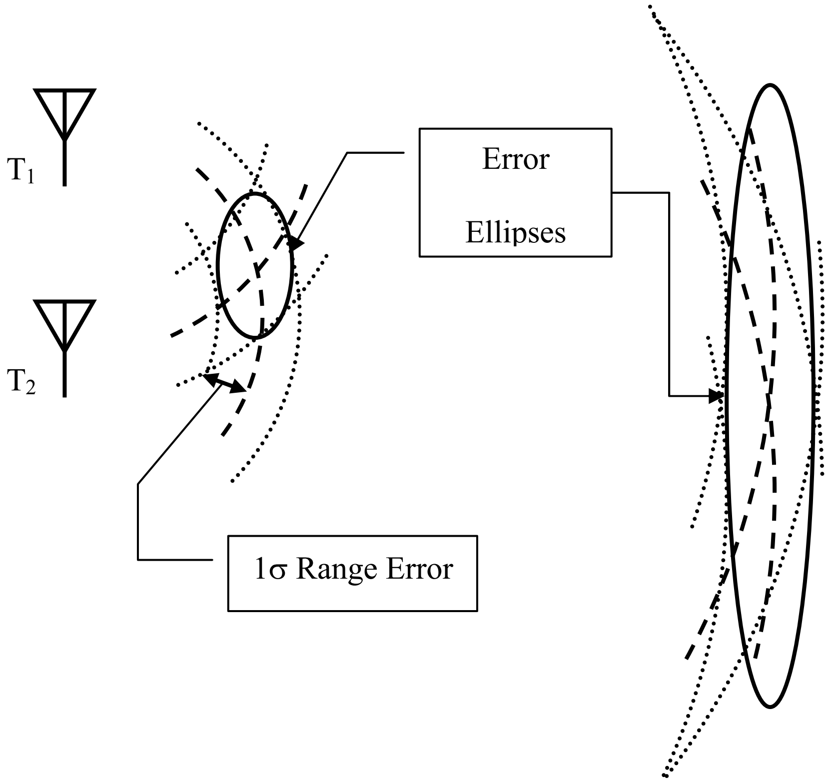

Figure 4.3 Cross-Range Error Ellipses

The models for cross-range variations in Chapter 3 were comprised of one constant and one range-dependent term. The 4 GPSTs used in the field measurements had good spatial diversity, so all the measurements should be uncorrelated. At ranges below ~200 meters both our assumptions for Equation 4.6 hold, and we can use the concept of DOP to go from measurement error to position error. Beyond ~200 meters measurement errors depend on cross-range distance, and Equation 4.5 must be used for those scenarios.

4.3 Post-Leap Covariance

To understand how uncertainty propagates after switching a set of LNS units from stationary to mobile status, we must first go back to the fundamental cross-range navigation equation.

4.3.1 GPST

In addition to linearizing Equation 2.7 around the mobile position, we must do the same around the position of the stationary unit because its position is no longer perfectly known. The 2-D case is shown in Equation 4.11.

$$\frac{\hat{\phi}_{m_1 s_1}}{2} \simeq d_{m_1,0}^{(s_1)} + \frac{\partial d_{m_1}^{(s_1)}}{\partial x_{m_1}} \cdot \Delta x_{m_1} + \frac{\partial d_{m_1}^{(s_1)}}{\partial y_{m_1}} \cdot \Delta y_{m_1} + \frac{\partial d_{m_1}^{(s_1)}}{\partial x_{s_1}} \cdot \Delta x_{s_1} + \frac{\partial d_{m_1}^{(s_1)}}{\partial y_{s_1}} \cdot \Delta y_{s_1} \qquad \textbf{Eq. 4.11}$$

A 2-D 4-unit set of GPSTs gives the following linearized set of equations.

$$\frac{1}{2}\begin{bmatrix} \hat{\phi}_{m_1 s_1} \\ \hat{\phi}_{m_1 s_2} \\ \hat{\phi}_{m_2 s_1} \\ \hat{\phi}_{m_2 s_2} \\ \hat{\phi}_{m_1 m_2} \end{bmatrix} - \begin{bmatrix} d_{m_1,0}^{(s_1)} \\ d_{m_1,0}^{(s_2)} \\ d_{m_2,0}^{(s_1)} \\ d_{m_2,0}^{(s_2)} \\ d_{m_1,0}^{(m_2)} \end{bmatrix} + \begin{bmatrix} \mathbf{los}_{m_1}^{(s_1)} & \mathbf{0} \\ \mathbf{0} & \mathbf{los}_{m_1}^{(s_2)} \\ \mathbf{los}_{m_2}^{(s_1)} & \mathbf{0} \\ \mathbf{0} & \mathbf{los}_{m_2}^{(s_2)} \\ \mathbf{0} & \mathbf{0} \end{bmatrix} \begin{bmatrix} \Delta x_{s_1} \\ \Delta y_{s_1} \\ \hline \Delta x_{s_2} \\ \Delta y_{s_2} \end{bmatrix} = \begin{bmatrix} \mathbf{los}_{m_1}^{(s_1)} & \mathbf{0} \\ \mathbf{los}_{m_1}^{(s_2)} & \mathbf{0} \\ \mathbf{0} & \mathbf{los}_{m_2}^{(s_1)} \\ \mathbf{0} & \mathbf{los}_{m_2}^{(s_2)} \\ \mathbf{-los}_{m_1}^{(m_2)} & \mathbf{los}_{m_1}^{(m_2)} \end{bmatrix} \begin{bmatrix} \Delta x_{m_1} \\ \Delta y_{m_1} \\ \hline \Delta x_{m_2} \\ \Delta y_{m_2} \end{bmatrix} \qquad \textbf{Eq. 4.12}$$

Notice the new left-hand term (compared to Equation 2.12) with a matrix of LOS vectors and zeros, multiplied by perturbations in the positions of the stationary positions. In simplified notation form, the previous equation can be written as.

$$\Delta \mathbf{y} + \underset{\sim}{\mathbf{G}}_s \cdot \Delta \mathbf{x}_s = \underset{\sim}{\mathbf{G}}_m \cdot \Delta \mathbf{x}_m \qquad \textbf{Eq. 4.13}$$

The Matlab routine for stacking $\underset{\sim}{\mathbf{G}}_s$ with an arbitrary number of mobile and stationary units is given in Appendix B. Let us apply the equation for covariance to the above equation.

$$E\left(\left(\Delta \mathbf{y} + \underset{\sim}{\mathbf{G}}_s \cdot \Delta \mathbf{x}_s\right) \cdot \left(\Delta \mathbf{y} + \underset{\sim}{\mathbf{G}}_s \cdot \Delta \mathbf{x}_s\right)^T\right) = E\left(\left(\underset{\sim}{\mathbf{G}}_m \Delta \mathbf{x}_m\right) \cdot \left(\underset{\sim}{\mathbf{G}}_m \Delta \mathbf{x}_m\right)^T\right) \qquad \textbf{Eq. 4.14}$$

The measurements contained in $\Delta\mathbf{y}$ are the driving terms in the above equation. If we assume $\Delta\mathbf{y}$ is unbiased, algebra yields the following solution for post-leap covariance.

$$E\left(\Delta\mathbf{x}_m \cdot \Delta\mathbf{x}_m^T\right) = \underset{\sim}{\mathbf{G}}_m^{\dagger} \cdot E\left(\Delta\mathbf{y} \cdot \Delta\mathbf{y}^T\right) \cdot \left(\underset{\sim}{\mathbf{G}}_m^{\dagger}\right)^T + \underset{\sim}{\mathbf{G}}_m^{\dagger} \cdot \underset{\sim}{\mathbf{G}}_s E\left(\Delta\mathbf{x}_s \cdot \Delta\mathbf{x}_s^T\right) \underset{\sim}{\mathbf{G}}_s^T \cdot \left(\underset{\sim}{\mathbf{G}}_m^{\dagger}\right)^T \qquad \textbf{Eq. 4.15}$$

Notice that the first right-side term in Equation 4.15 is the same as in the pre-leap case, and it describes position uncertainty of the rovers relative to the stationary units. The second and new term in the equation describes the uncertainty of the stationary positions with respect to the initial position. Thus, Equation 4.15 gives the absolute error of the mobiles relative to the original locations of the units.

The same equation could also be used in initializing LNS with an external reference, say GPS. The GPS position covariance matrix could be projected into the LNS frame, and those projections would initialize the LNS error model. Thus, total rover position errors would be estimated with respect to WGS-84.

4.3.2 UWB Transponder

The UWB transponder equivalent to Equation 4.12 is given below.

$$\frac{1}{4}\begin{bmatrix} \varphi_{m_1 s_1} + \varphi_{s_1 m_1} \\ \varphi_{m_1 s_2} + \varphi_{s_2 m_1} \\ \varphi_{m_2 s_1} + \varphi_{s_1 m_2} \\ \varphi_{m_2 s_2} + \varphi_{s_2 m_2} \\ \varphi_{m_1 m_2} + \varphi_{m_2 m_1} \end{bmatrix} - \frac{1}{4}\begin{bmatrix} \delta^{(m_1)} + \delta^{(s_1)} \\ \delta^{(m_1)} + \delta^{(s_2)} \\ \delta^{(m_2)} + \delta^{(s_1)} \\ \delta^{(m_2)} + \delta^{(s_2)} \\ \delta^{(m_1)} + \delta^{(m_2)} \end{bmatrix} - \begin{bmatrix} d_{m_1,0}^{(s_1)} \\ d_{m_1,0}^{(s_2)} \\ d_{m_2,0}^{(s_1)} \\ d_{m_2,0}^{(s_2)} \\ d_{m_1,0}^{(m_2)} \end{bmatrix} + \begin{bmatrix} \mathbf{los}_{m_1}^{(s_1)} & \mathbf{0} \\ \mathbf{0} & \mathbf{los}_{m_1}^{(s_2)} \\ \mathbf{los}_{m_2}^{(s_1)} & \mathbf{0} \\ \mathbf{0} & \mathbf{los}_{m_2}^{(s_2)} \\ \mathbf{0} & \mathbf{0} \end{bmatrix} \left[\begin{array}{c} \Delta x_{s_1} \\ \Delta y_{s_1} \\ \hline \Delta x_{s_2} \\ \Delta y_{s_2} \end{array}\right] \qquad \textbf{Eq. 4.16}$$

$$= \left[\begin{array}{c|c} \mathbf{los}_{m_1}^{(s_1)} & \mathbf{0} \\ \mathbf{los}_{m_1}^{(s_2)} & \mathbf{0} \\ \mathbf{0} & \mathbf{los}_{m_2}^{(s_1)} \\ \mathbf{0} & \mathbf{los}_{m_2}^{(s_2)} \\ \textbf{-los}_{m_1}^{(m_2)} & \mathbf{los}_{m_1}^{(m_2)} \end{array}\right] \left[\begin{array}{c} \Delta x_{m_1} \\ \Delta y_{m_1} \\ \hline \Delta x_{m_2} \\ \Delta y_{m_2} \end{array}\right]$$

In simplified notation the above equation reads

$$\Delta\mathbf{y} - \boldsymbol{\delta} + \underset{\sim}{\mathbf{G}}_s \cdot \Delta\mathbf{x}_s = \underset{\sim}{\mathbf{G}}_m \cdot \Delta\mathbf{x}_m \qquad \textbf{Eq. 4.17}$$

We can input Equation 4.17 into the equation for calculating variance, and after some algebra to following result appears

$$\begin{aligned} E\left(\Delta\mathbf{x}_m \cdot \Delta\mathbf{x}_m^T\right) &= \underset{\sim}{\mathbf{G}}_m^{\dagger} \cdot \left[E\left(\Delta\mathbf{y} \cdot \Delta\mathbf{y}^T\right) + E\left(\boldsymbol{\delta} \cdot \boldsymbol{\delta}^T\right)\right] \cdot \left(\underset{\sim}{\mathbf{G}}_m^{\dagger}\right)^T \\ &\quad + \underset{\sim}{\mathbf{G}}_m^{\dagger} \cdot \underset{\sim}{\mathbf{G}}_s E\left(\Delta\mathbf{x}_s \cdot \Delta\mathbf{x}_s^T\right) \underset{\sim}{\mathbf{G}}_s^T \cdot \left(\underset{\sim}{\mathbf{G}}_m^{\dagger}\right)^T \end{aligned} \qquad \textbf{Eq. 4.18}$$

Again, the only structural difference between the above equation and Equation 4.15 for GPS transceivers is the inclusion of a term for variation of processing delay of a transponder. The effects of this additional driving term in the equation is offset by the ability to average measurements going both ways between pairs of transponders, unlike GPSTs where 4 individual measurements are needed to calculate each cross-range.

4.4 Bounding of Position Error Growth

We are interested in finding how position errors grow after "many" leaps. While Equation 4.12 gave the solution for one leap with GPSTs, the following gives the recursive algorithm for *N* leaps.

$$\begin{aligned} E\left(\Delta\mathbf{x}_m \cdot \Delta\mathbf{x}_m^T\right)_0 &= \underset{\sim}{\mathbf{G}}_{m,0}^{\dagger} \cdot E\left(\Delta\mathbf{y} \cdot \Delta\mathbf{y}^T\right)_0 \cdot \left(\underset{\sim}{\mathbf{G}}_{m,0}^{\dagger}\right)^T \\ &\vdots \\ E\left(\Delta\mathbf{x}_m \cdot \Delta\mathbf{x}_m^T\right)_N &= \underset{\sim}{\mathbf{G}}_{m,N}^{\dagger} \cdot E\left(\Delta\mathbf{y} \cdot \Delta\mathbf{y}^T\right)_N \cdot \left(\underset{\sim}{\mathbf{G}}_{m,N}^{\dagger}\right)^T \\ &\quad + \underset{\sim}{\mathbf{G}}_{m,N}^{\dagger} \cdot \underset{\sim}{\mathbf{G}}_{s,N} E\left(\Delta\mathbf{x}_m \cdot \Delta\mathbf{x}_m^T\right)_{N-1} \underset{\sim}{\mathbf{G}}_{s,N}^T \cdot \left(\underset{\sim}{\mathbf{G}}_{m,N}^{\dagger}\right)^T \end{aligned} \qquad \textbf{Eq. 4.19}$$

Note that last (*N*-1) mobile positions are the current (*N*) stationary positions.

Similarly, Equation 4.20 gives the UWB equivalent to Equation 4.19.

$$\begin{aligned}
E\left(\Delta\mathbf{x}_m \cdot \Delta\mathbf{x}_m^T\right)_0 &= \underset{\sim}{\mathbf{G}}_{m,0}^{\dagger} \cdot \left[E\left(\Delta\mathbf{y} \cdot \Delta\mathbf{y}^T\right)_0 + E\left(\boldsymbol{\delta} \cdot \boldsymbol{\delta}^T\right)_0\right] \cdot \left(\underset{\sim}{\mathbf{G}}_{m,0}^{\dagger}\right)^T \\
&\vdots \\
E\left(\Delta\mathbf{x}_m \cdot \Delta\mathbf{x}_m^T\right)_N &= \underset{\sim}{\mathbf{G}}_{m,N}^{\dagger} \cdot \left[E\left(\Delta\mathbf{y} \cdot \Delta\mathbf{y}^T\right)_N + E\left(\boldsymbol{\delta} \cdot \boldsymbol{\delta}^T\right)_N\right] \cdot \left(\underset{\sim}{\mathbf{G}}_{m,N}^{\dagger}\right)^T \\
&\quad + \underset{\sim}{\mathbf{G}}_{m,N}^{\dagger} \cdot \underset{\sim}{\mathbf{G}}_{s,N} E\left(\Delta\mathbf{x}_m \cdot \Delta\mathbf{x}_m^T\right)_{N-1} \underset{\sim}{\mathbf{G}}_{s,N}^T \cdot \left(\underset{\sim}{\mathbf{G}}_{m,N}^{\dagger}\right)^T
\end{aligned} \qquad \textbf{Eq. 4.20}$$

We note the additional driving term, $E\left(\boldsymbol{\delta} \cdot \boldsymbol{\delta}^T\right)$, stemming from uncertainty in processing delay.

4.4.1 Simulation Setup

We will consider three different simulation scenarios with 4 LNS units: a 2.5-m baseline indoor case, a 10-m baseline outdoor case and a 100-m baseline outdoor case. Two of the LNS units (red circles) are initially stationary with known positions. The two initially mobile units are marked with (green) stripes in Figure 4.4.

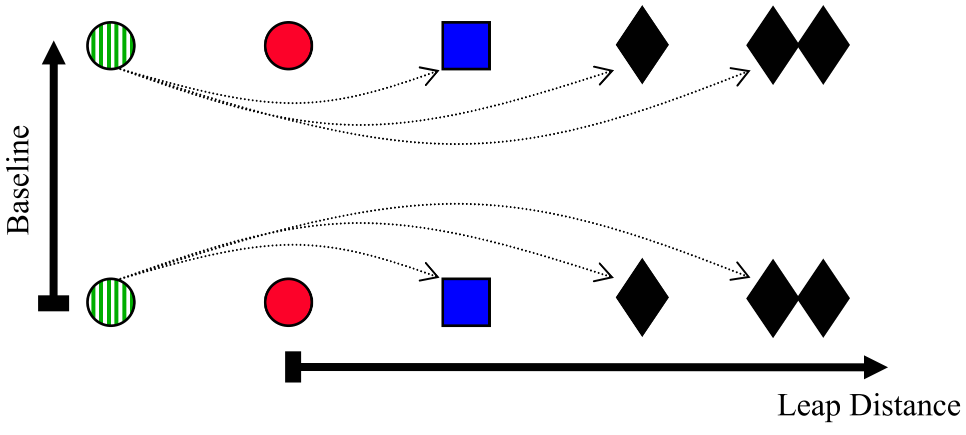

Figure 4.4 Simulation Setup

We will constrain the units to follow a constant heading, and we will keep the baseline distance between stationary units constant at the points of transition. We are interested in finding how the total positioning error grows for each leap, and leap-distance is the free parameter in our simulations. In Figure 4.4 this means having the choice of next time moving the mobiles to the blue squares, the black diamonds, or hitting the double-black diamonds.

While the previous paragraph described the geometry of the setup, we also need a model of ranging errors. For the 2.5-m baseline indoor case we will assume the use of UWB transponders. We will use rather conservative 6 cm ranging errors for the 1 GHz bandwidth case from Chapter 2.4.3. Furthermore, we will use a similar 6 cm standard deviation of the transponder processing delays (δ). Finally, we will constrain our simulations to an area of size 2.5m x 20m.

The models of GPST outdoor cross-range errors can be found in Figure 3.29, and the models consist of a constant term and a range-dependent one.

The 10-m baseline outdoor case will be simulated using GPSTs, and the maximum leap distance will be limited to 40 meters. These simulations all lie within the constant-error region of the GPST error model.

The 100-m baseline case will also be simulated using GPSTs with leap-distances between 100 m and 400 m. The worst-case error model with d^4 range dependence will be used.

4.4.2 Simulation Results

4.4.2.1 Indoor UWB with 2-m Baseline

Figure 4.5 below shows the results for the indoor case with leap distances varying from 2.5 to 10 meters.

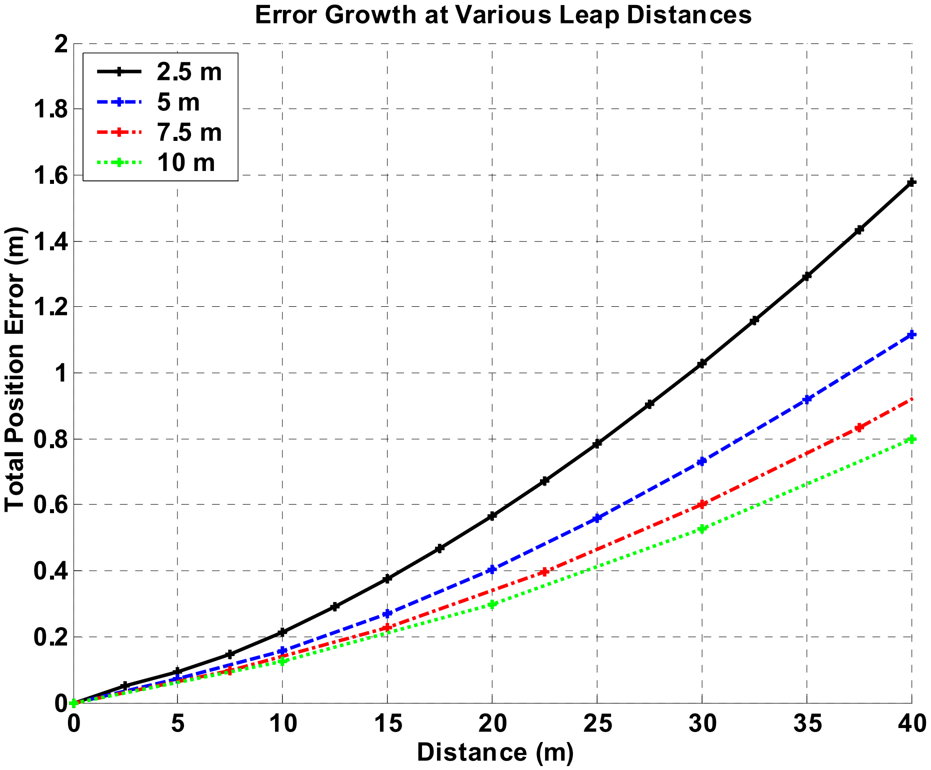

Figure 4.5 Indoor UWB with 2.5m Baseline

Since we assumed that cross-ranging error was independent of range for the limited simulation scenario, the plot indicates that increasing leap-distance leads to less error growth. The area used in the simulation was only 20 meters long, but results are given for a total distance of 40 meters. This range includes the option of round-trip travel.

4.4.2.2 Outdoor GPST with 10-m Baseline

The results for the short-baseline outdoor case with leap distances varying from 10 to 40 meters are plotted In Figure 4.6.

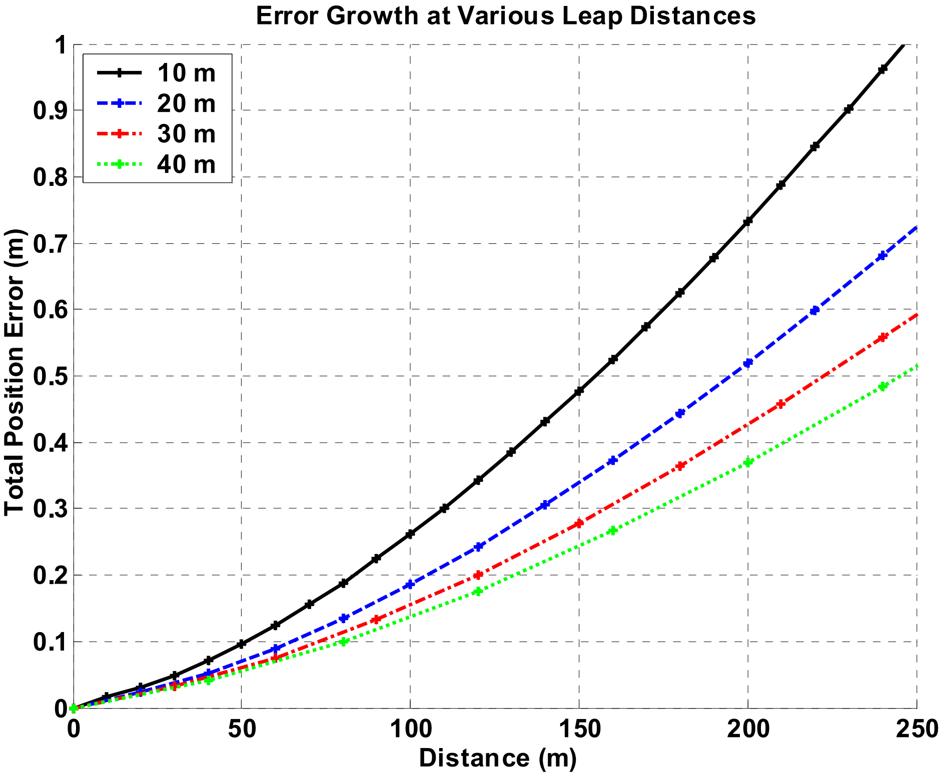

Figure 4.6 Outdoor GPST with 10m Baseline

With cross-range errors constant, we see the same trend as before, i.e. decreasing absolute position error growth with increasing leap distance. The more benign outdoor multipath environment also leads to less error accumulation for the same distances traveled compared to the indoor case.

4.4.2.3 Outdoor GPST with 100-m Baseline

Figure 4.7 on the next page contains the results for the long-baseline outdoor GPST case with leap distances from 100 m to 400 m.

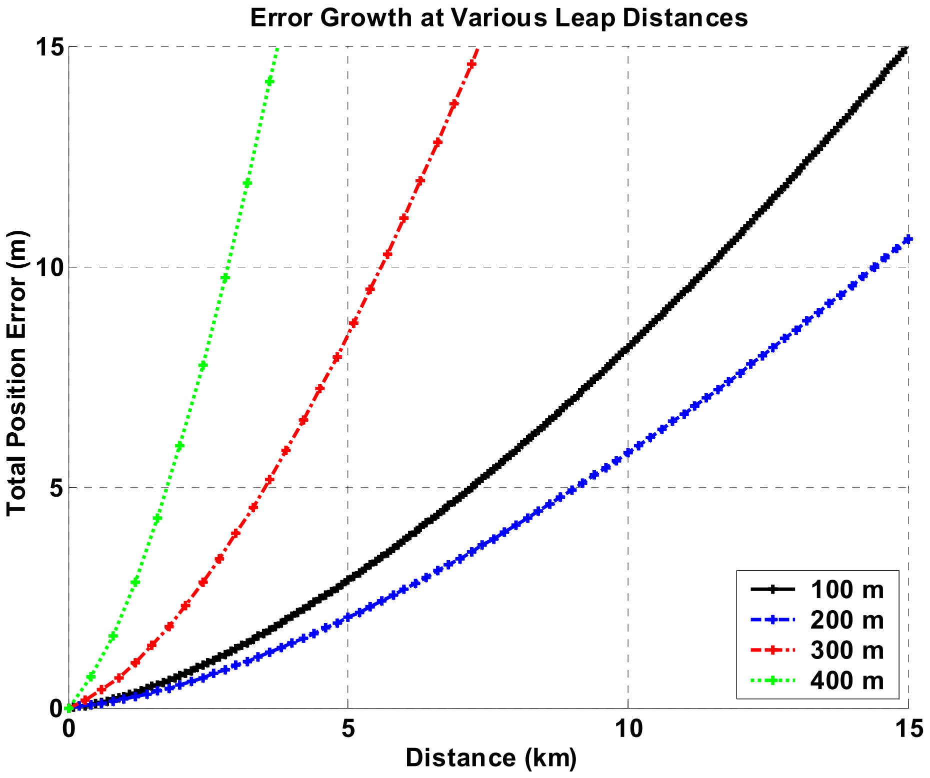

Figure 4.7 Outdoor GPST with 100m Baseline

We find that the optimum leap distance coincides with the "knee" in the curve for cross-range error (Figure 3.29). Up to 200 meters, the relative position error term in Equation 4.15 grows like DOP in Figure 4.2. Although this driving error term increases with distance, less total error is accumulated when making increasingly longer leaps. Beyond 200 meters, cross-range error is a very strong function of distance (d^4). Thus, the cost of making longer leaps far outweighs the benefits of the incremental distance gained in each leap.

The most important result that can be read from the above figure, is the total bound on position error. Given that a 10 meter total position error can be tolerated, Figure 4.7 shows that a 300-m leap-distance system has a total range of more than 5 km. The corresponding 200-m system could go almost 15 km. In terms of a round-trip mission, this would limit exploration to an area within ~7.5 km from the initial location.

4.4.3 Simulation Error Sources

One of our previous assumptions was of unbiased measurements. Although all radio navigation systems have biases in their fundamental measurements (e.g. from multipath), these errors may not be perfectly corrected even if error models exist. Practically speaking, this means that the confidence bound on the variability of those measurements must be inflated in order to envelop such biases.

Another bias term arises from using non-collocated transmit and receive antennas as described by Figure 4.8.

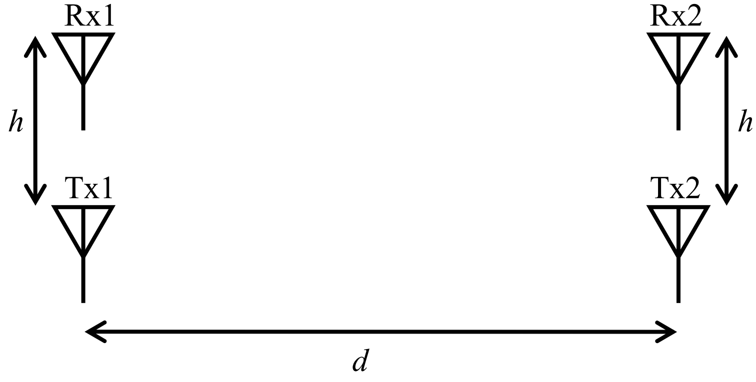

Figure 4.8 Non-Collocated TX/RX Antennas

We seek to find the true distance, *d*, along ground, but we are in fact measuring $\sqrt{d^2 + h^2}$.

The error induced by the out-of-plane component is calculated in Equation 4.21 on the next page.

$$\delta = d - \sqrt{d^2 + h^2} \qquad \textbf{Eq. 4.21}$$

Here, δ is range error, d is 2-D true range and h is TX/RX antenna spacing. At 100 meter baseline distance and 60 cm antenna spacing this error is only 1.9 mm. However, the error is 1.8 cm if the baseline were to be reduced to 10 meters.

4.5 Summary

In this chapter, I developed expressions for position covariances for pre-leap, post-leap and multi-leap cases both for LNS implementations using UWB transponders and for GPS transceivers. The equations for the two implementation options look very similar, except for an additional term needed to describe variability of processing delay through a UWB transponder.

Fundamentally, the position covariances of either LNS implementation are functions of cross-ranging errors, current geometry, and previous position uncertainty of the stationary units.

Three LNS scenarios were simulated, one indoor UWB transponder and two outdoor GPS transceiver ones. The indoor case and a short-range outdoor one showed that increasing the leap-distance always was beneficial since a constant-range-error model was used. A long-range simulation showed that the optimum leap-distance coincided with the "knee" in the range-error model (Figure 3.29). Using that model, the total range of a 100-m baseline LNS was estimated to ~15 km if an absolute position error of 10 meters could be tolerated.

In the next chapter, I will try to validate the above simulations through actual field tests of LNS.

5 Leapfrog Experimental Setup and Results

This chapter describes the field test campaign that was undertaken to prove the concept of leapfrog navigation. The chapter starts off with a discussion of hardware considerations for designing GPS transceivers and their antenna systems. Next is a description of the radio system used to exchange/log measurements from the GPSTs.

A prototype LNS was built using off-the-shelf parts and Sub-Chapter 5.2 lays out an outdoor LNS test scenario. The final field test results are presented in Sub-Chapter 5.3, and actual position errors are compared to simulated ones from Chapter 4.

5.1 Hardware Design Choices and Description

5.1.1 GPS Transceiver

Previous research on Self Calibration Pseudolite Arrays (SCPA) at Stanford University used a student-designed GPS receiver (Mitel-Orion) [44]. While this receiver was wonderfully flexible as far as modifying firmware went, it was unfortunately less than user-friendly and had limited signal tracking dynamics. Thus, several off-the-shelf OEM receivers were considered as a replacement, and Canadian Marconi Corporation (CMC) Allstar receivers were ultimately chosen for use with LNS. These are single-frequency GPS receivers that are fairly inexpensive (~$500), but still provide carrier phase tracking at output rates of 10 Hz. Furthermore, Allstar receivers provide a mode of operation where all measurements are aligned with GPS time. This feature proves vital in synchronizing the measurements among multiple receivers used for carrier phase differential GPS (CP-DGPS) positioning.

CMC Allstar receivers ship in the form of OEM boards, ready for integration with other equipment. The receiver runs off 5V DC power and has an RS-422 [45] data interface. The rest of my equipment ran off 12V batteries and required RS-232 [45] communications. To accommodate the Allstars I designed a printed circuit board (PCB) containing a 5V DC power regulator and an RS-422 to RS-232 level changer. The PCB also had jumpers to enable 5V, 12V or no power to the coax antenna connector on the Allstar (for powering RX antenna low-noise amplifiers (LNA)). The PCB layout is plotted in Appendix D.

Extra care was taken in order to RF-isolate each receiver since it would be in intimate proximity to a pseudolite and its transmit antenna. The pseudolites used in this work were the Integrinautics IN 200c models. Under license from the FCC [46] these pseudolites were operated at 1μW of transmit power. The PLs use an RTCM pulsing scheme with a duty cycle of approximately 3 %. Even with this low duty cycle, the transmitted power levels are tremendously strong compared to the -130dBm power level received from GPS satellites. Un-checked RF-leakage could potentially be devastating to system operation. To alleviate such concerns, each receiver was enclosed in a metal box with screws every 2-3 cm along the openings. All important external cabling was outfitted with ferrite beads to choke off RF even further. Finally, the boxes were sealed with copper tape. The picture on the next page shows an open box with the CMC Allstar receiver, the interface board and all internal cabling.

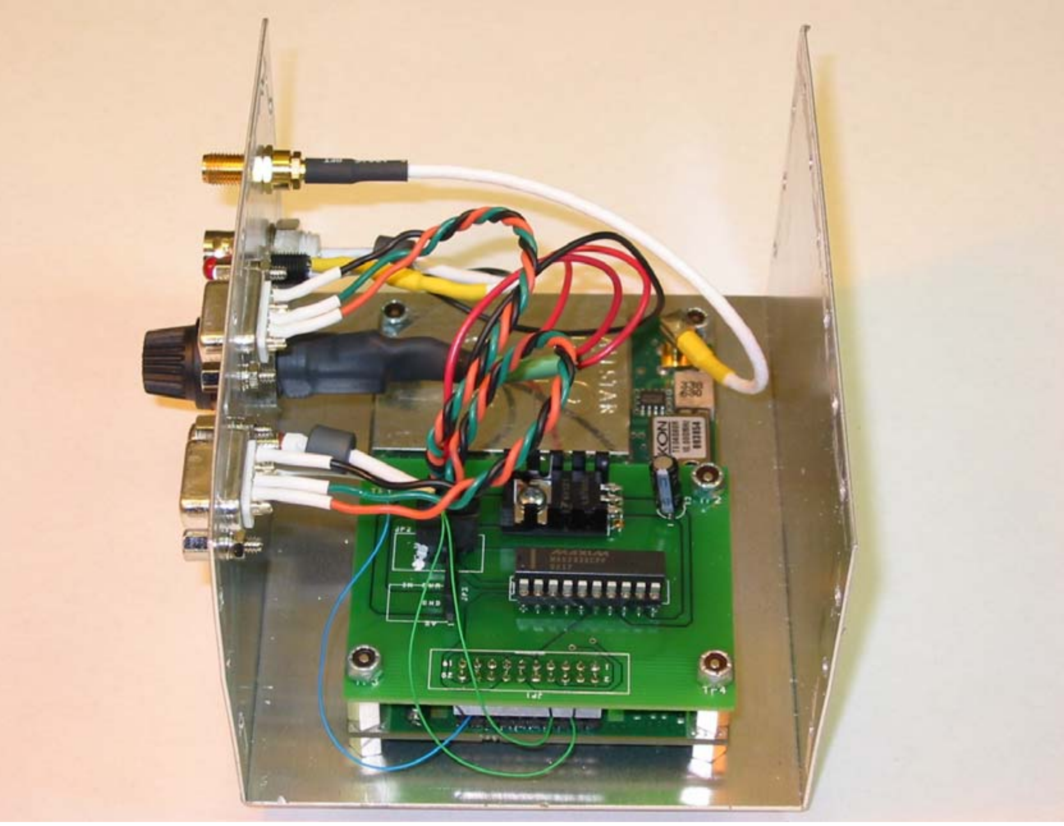

Figure 5.1 Open Box CMC Allstar

GPS is inherently robust against pulsed interference, and the RTCM pulsing scheme used in these experiments has proven to mitigate the near-far problem. This problem arises when simultaneously trying to receive strong and weak signals, such as from a nearby PL and a satellite far, far away. If both signals were transmitted continuously, the automatic gain control (AGC) circuitry of a receiver would use the strongest signal for setting its level. Thus, the already weak signal would be made even weaker and tracking would be lost.

Most off-the-shelf GPS receivers, like the CMC Allstar, employ "slow" AGCs. This means that a short pulse of high amplitude only marginally changes the AGC level, so tracking of low power signals is only affected benignly. Another option would be to implement a “fast” AGC that would almost instantly change its level when a strong pulsed signal is detected, and as quickly recede to its nominal level when tracking weaker signals.

5.1.2 Antenna System

The signals transmitted from the GPS satellites are right-hand circularly polarized (RHCP), and receive antennas are matched up with the same polarization direction. Circular polarization is an obvious choice for satellite navigation systems, since receive antennas may point in any direction during regular use. In addition, the signal experiences Faraday rotation as it travels through the ionosphere. A linearly polarized signal would fade severely under the above conditions.

Circularly polarized signals experience carrier phase wind-up effects if the transmit and receive antennas are rotated relative to each other. Carrier phase range measurements increase or decrease depending on the direction an antenna is rotated; the same way they would change if the antennas were moved closer together or farther apart. Seemingly, antenna rotation translates into antenna translation.

A ground-based system might not have the same constraints as a space-based one. I chose to use a vertical dipole transmit antenna[4], and a circularly polarized patch[5] on a ground plane as a receive antenna. Figure 5.2 on the next page shows the two antennas (not to the same scale).

---

[4] Courtesy Masayoshi Matsuoka

[5] MicroPulse Mini-Arinc 12700 series

Figure 5.2 Transmit and Receive Antennas

The toroid antenna pattern of a vertical dipole illuminates the entire azimuth plane, so transmit power along the ground is independent of direction. A patch antenna on a ground plane has a hemispherical antenna pattern that drops off rapidly at low elevation. Not only does this provide added isolation between the ultra-strong adjacent pseudolites and the ultra-weak satellite signals, but the antenna pattern also helps suppress ground-reflection multipath. Stacking the receive antenna on top of the transmit dipole aligns its antenna pattern null with the direction of the RX antenna. The ground plane also provides extra shielding. The figure on the next page sketches vertical cuts through the antenna patterns of two adjacent GPS transceivers. The RX patches are marked with ovals, and the dipoles with two bars. The antenna patterns are sketched as dashed lines.

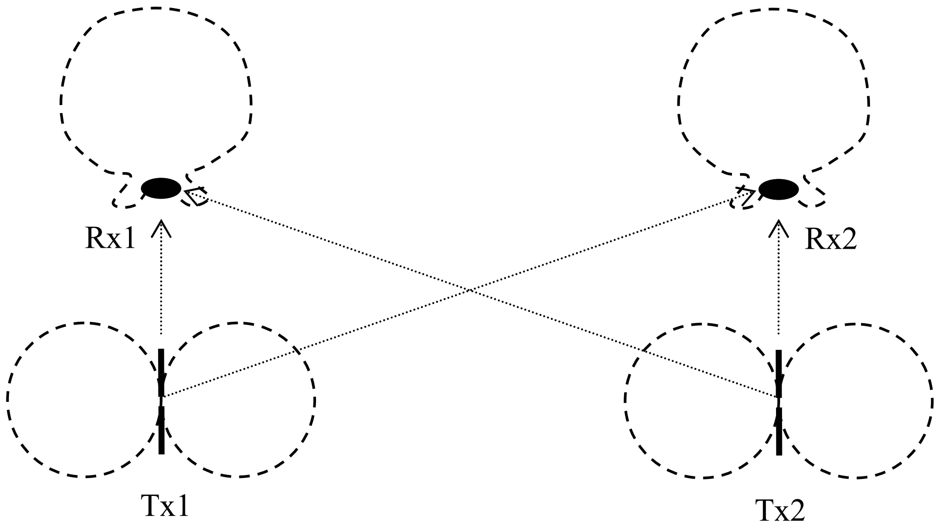

Figure 5.3 Antenna Patterns of GPSTs

5.2 Communication and Data Logging

All GPS transceivers in a network are mutually dependent on each other since positions are calculated based on sum-difference measurements between all GPST pairs. While a network like this also may lend itself to distributed computing, it does require information exchange among all the nodes. In a real-time LNS implementation, measurement data could be modulated onto the data stream from the pseudolites, in the same way as with WAAS [47]. This would require both receiver and pseudolite modifications, but would avoid the added cost and complexity of a separate data link radio.

The leapfrog navigation system prototype was implemented for post-processing of positioning data. A set of Proxim RangeLan2 radios were used to collect data from all

GPSTs. The Proxims could be configured for point to multi-point communications, and a base-station would collect data from all GPS transceivers, as depicted in Figure 5.4.

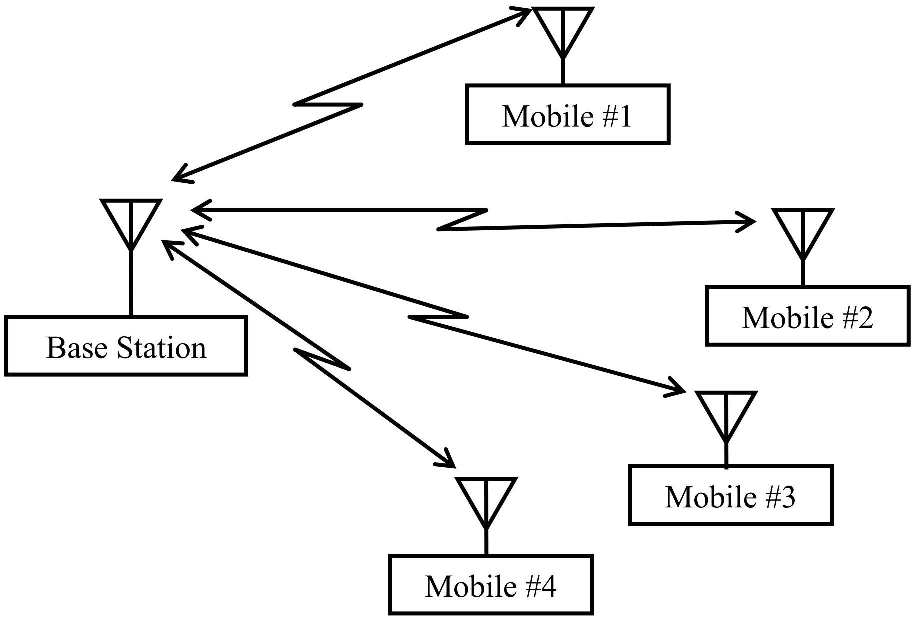

Figure 5.4 Proxim Point to Multi-Point Communication

The CMC Allstar GPS receivers output a binary data stream through a serial interface to the mobile Proxim units, and all streams were transmitted to the Proxim base station and finally to a laptop across an Ethernet interface. Raw data from all units were saved in separate files on the laptop for post-processing. The data paths are shown in Figure 5.5.

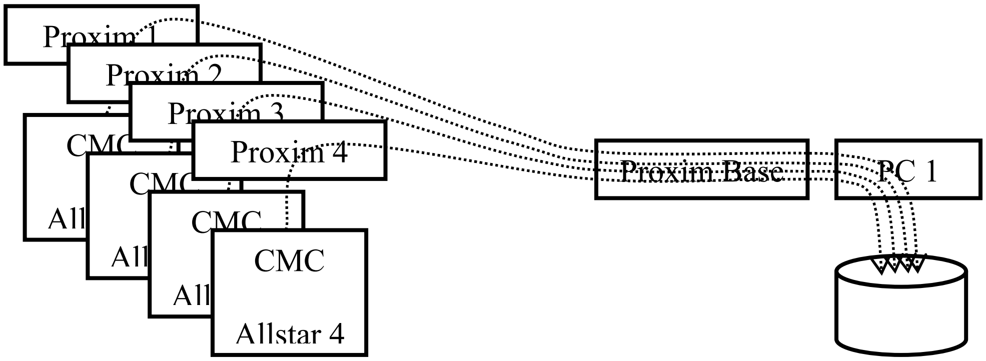

Figure 5.5 GPS Data Flow

Yet another laptop was connected to the first one. This second laptop contained the "CMC GPS Monitor" program (Courtesy Masa Matsuoka), which was used to command the Allstars. Since the receivers by default search for satellites given in the almanac, it proved vital to be able to command the receivers to track the pseudolite PRNs instead. With a 12-channel receiver and a maximum of 12 SVs in view, some of those satellites had to be manually de-selected to give room for pseudolite tracking. The data flow for commanding the Allstars is given in the block diagram below.

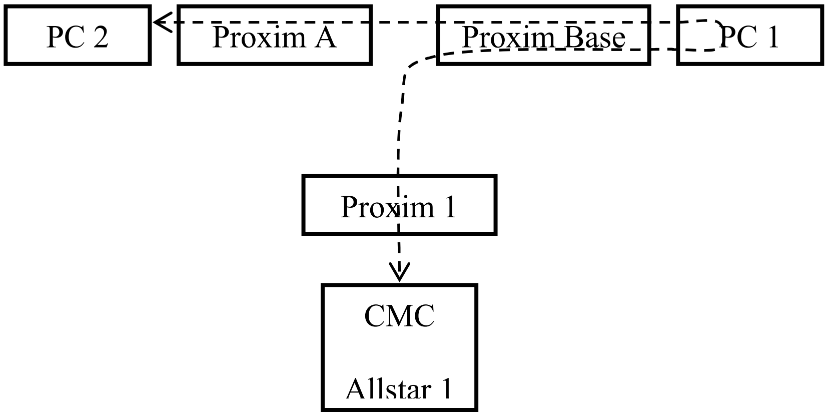

Figure 5.6 Command Data Flow

5.3 LNS Test Scenario and Data Pre-Conditioning

The leapfrog navigation prototype was tested in an open field (Roble Field at Stanford University). Four GPSTs (U_1-U_4) were set up in the vertices of a 10m by 10m square, and four additional target points (blue squares and black diamonds) were also pre-surveyed. Figure 5.7 on the next page shows the layout of the test area.

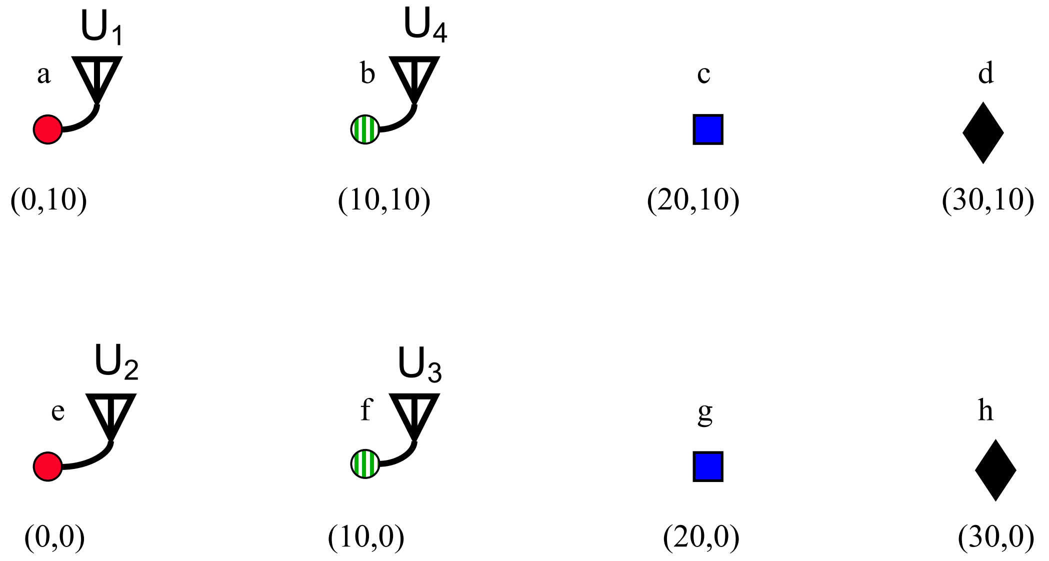

Figure 5.7 Layout of Test Area

Having units U_1 and U_2 act as the initial references (red circles), the positions of units U_3 and U_4 (green stripes) were calculated. U_3 and U_4 were then switched to stationary mode, and U_1 and U_2 were moved from locations a to c and from e to g respectively. The tables were then turned, and units U_3 and U_4 were moved from locations f to h and from b to d. Finally, the units were moved back to their initial locations in the reverse order. Looking at the navigation algorithms (Eq. 2.13), it is clear that up to two units could be moved at a time. In the 2-D case, the only navigation algorithm breakdown occurs if all 4 units line up. Any algorithm singularities were avoided by moving only one GPST at a time, although staggered motion of the mobiles also would have solved the problem.

From Figure 2.9 we find a position ambiguity, because any pair of mobile locations will have mirror images that also solve the equations. This issue cannot be solved using cross-range measurements alone, but only requires initial knowledge of which side of the stationary baseline the two mobiles are.

All 8 test points, a-h, were surveyed using a tape measure, and the targets were marked on the grass using non-toxic spray paint, as shown in the picture below.

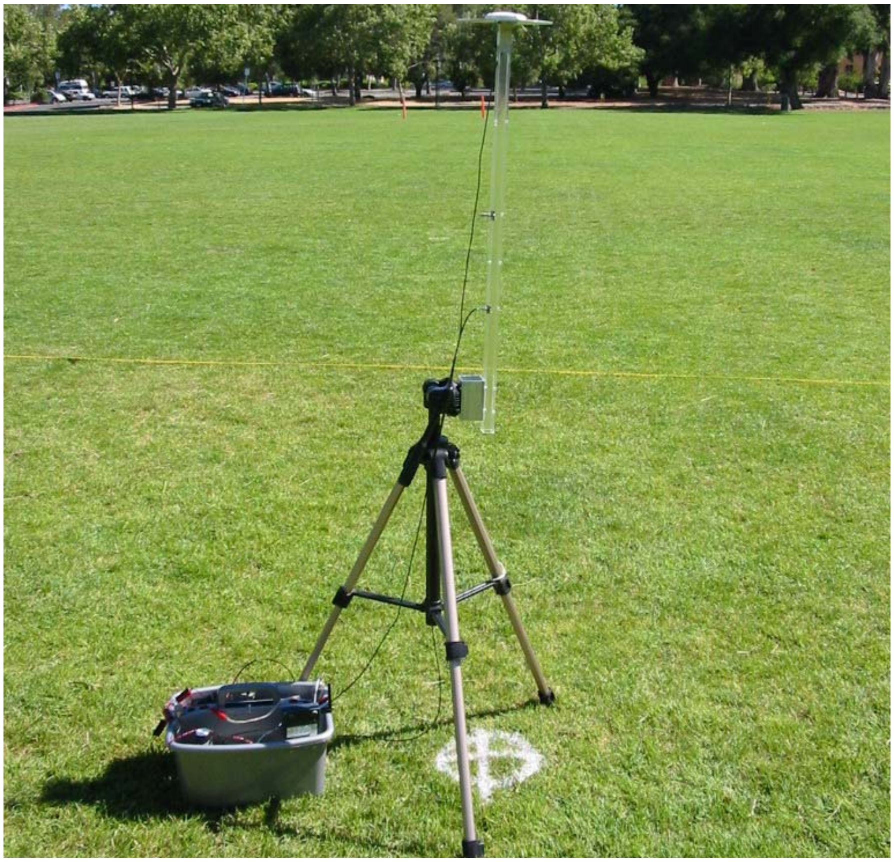

Figure 5.8 Antenna Alignment

Plumb bobs were used to center the antennas directly over the targets, and this alignment procedure should reduce "truth" errors to a few centimeters.

Care was taken to always face the antennas in the same directions, so carrier phase wind-up could be more easily calibrated. These corrections were made manually before the measurements were passed on to the positioning algorithms.

Figure 5.9 shows some of the details of the cross-range measurements between units 1 and 2.

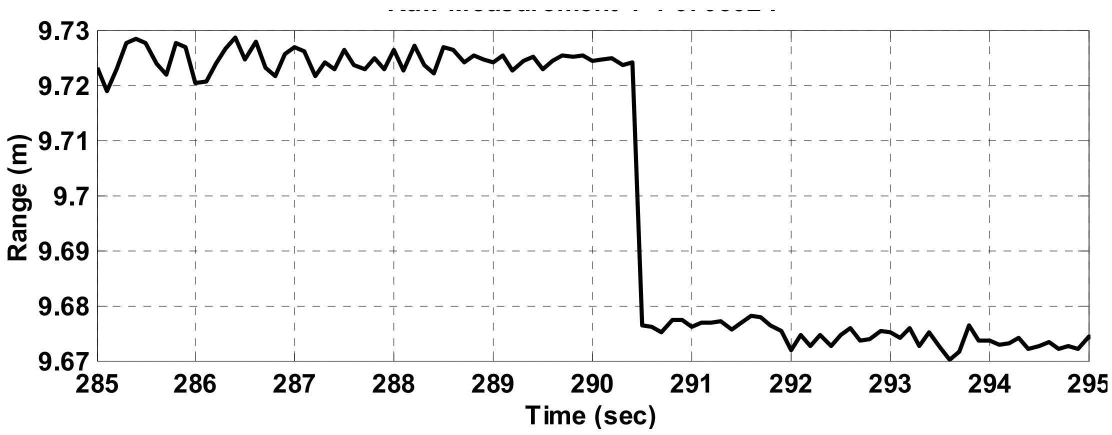

Figure 5.9 Cross-Range Measurement with Cycle Slip

A quarter-cycle slip (~ 5 cm) is clearly noticeable at time 290.5 sec (This is really a ½ cycle slip on one receiver, but the sum-difference GPST process includes a division by 2). Such cycle slips were rather prevalent throughout the data sets, but could easily be corrected in the cases when pairs of GPSTs were standing still. However, the dynamics while moving a unit were so great that cycle slips were indistinguishable from true change in range. Thus, the data is very likely to contain un-corrected cycle slips during motion.

Figure 5.10 shows an event that can be characterized as a "slow" cycle slip while two units were stationary. One likely explanation of the phenomenon may be that multipath (probably from the researcher) momentarily upset signal tracking, but the receiver re-gained lock almost immediately.

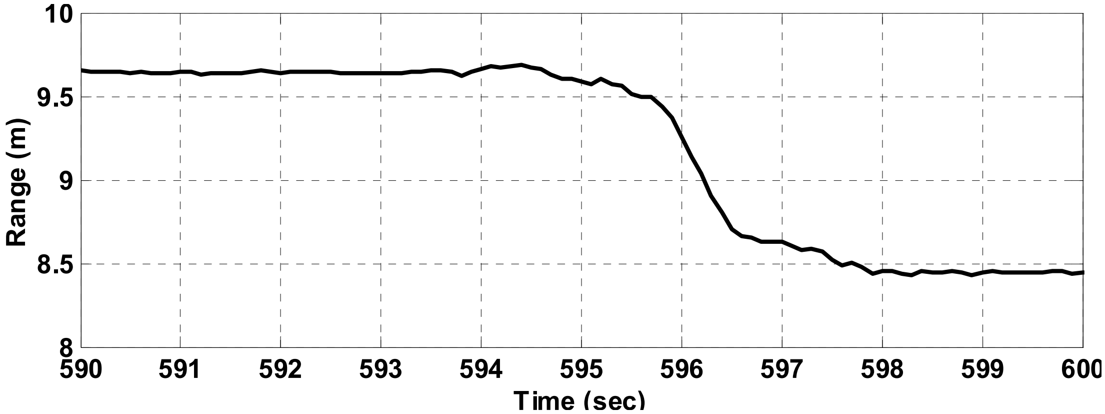

Figure 5.10 4-Second "Slow" Cycle Slip

The above event was only observed once during the entire 3-month field-test campaign, and it was manually corrected by fitting a cubic spline to the data. A more robust implementation of LNS may apply Receiver Autonomous Integrity Monitoring (RAIM) [48], where erroneous measurements would be removed from the solution automatically. The 4-unit LNS implementation solves 4 unknowns using 5 independent measurements. Erroneous measurements could be identified by inspecting cross-range residuals after solving for position. In this way single cross-range errors could be isolated and removed from the otherwise over-determined solution set. In the case where the mobile-to-mobile measurement is disrupted, the 2 mobile locations can still be calculated from 2 pairs of cross-ranges from 2 stationary units. If a mobile-to-stationary measurement is deemed erroneous, first the "good" mobile location can be found from 2 cross-ranges. Then, the second mobile location can be found using the good mobile-to-stationary measurement, and the mobile-to-mobile measurement.

Occurrence of cycle slips could not easily be correlated to external events, but the carrier upsets are likely attributed to multipath. Additionally, the receivers were brought into saturation while tracking the overwhelmingly powerful signals from the pseudolites.

This mode of operation is well outside the specifications of the Allstars, but I can only speculate how such non-linearities affect signal tracking since that information is proprietary to CMC.

5.4 Experimental Results

Position solutions were generated after pre-processing the raw data to remove obvious cycle slips and cycle wind-up effects. Figure 5.11 shows the plot of position solutions as the field test progresses.

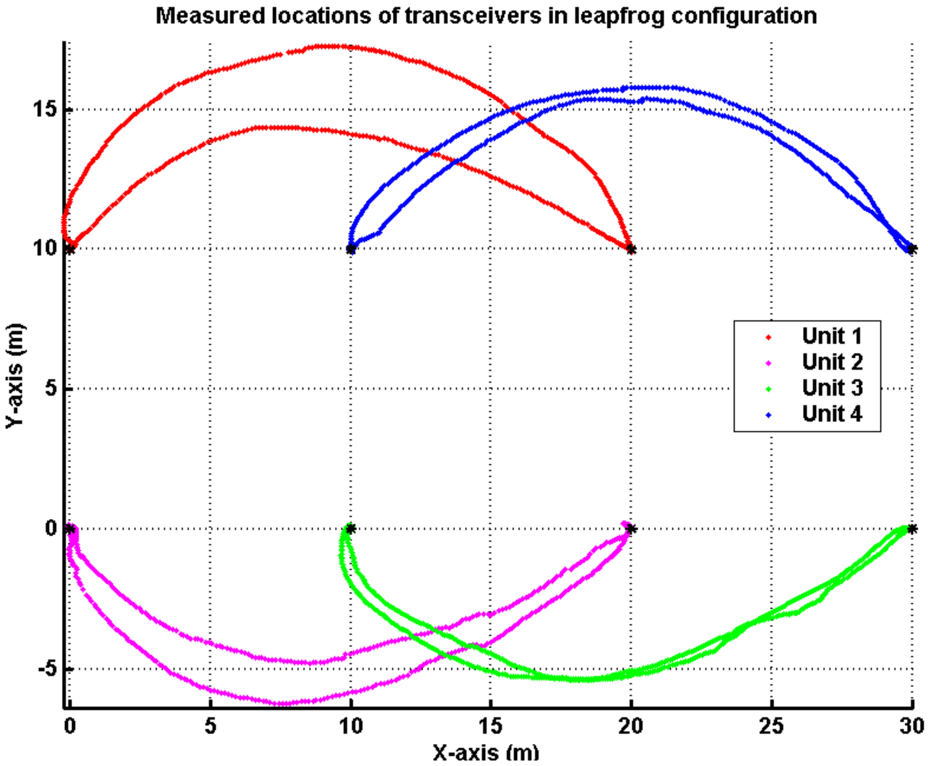

Figure 5.11 Field Test Position Results

These results were generated in Matlab® on a 1.6 GHz P4 PC at approximately 3 times the speed required for real-time operations.

While Figure 5.11 shows that LNS works, the figure on the below has information about how well it works.

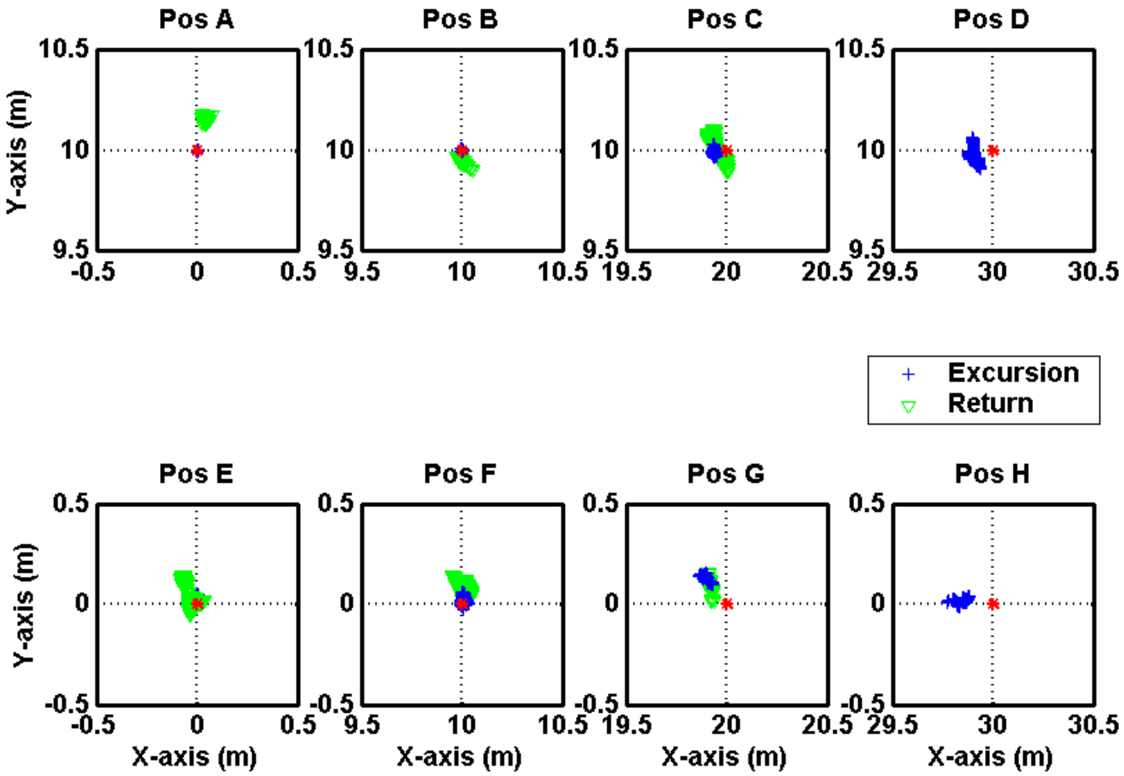

Figure 5.12 Field Test Position Results Zoomed View

The center of each sub-plot shows the pre-surveyed target locations. The crosses and triangles show position solutions during excursion and return respectively. These positions are calculated for GPSTs that are treated as mobiles in the navigation algorithms, but in fact are stationary (only one GPST was moved at a time). Comparing the position solutions with the surveyed locations, we find horizontal root-mean-squared (HRMS) position errors in the 5-15 cm range after 4 leaps of 10 meters each. Figure 5.13 shows measured RMS error statistics for each leap compared with the simulated position uncertainties from the covariance analysis in Chapter 4. The original model used a 1 cm value for cross-range error, but the figure also shows results for 2 cm and 4 cm errors.

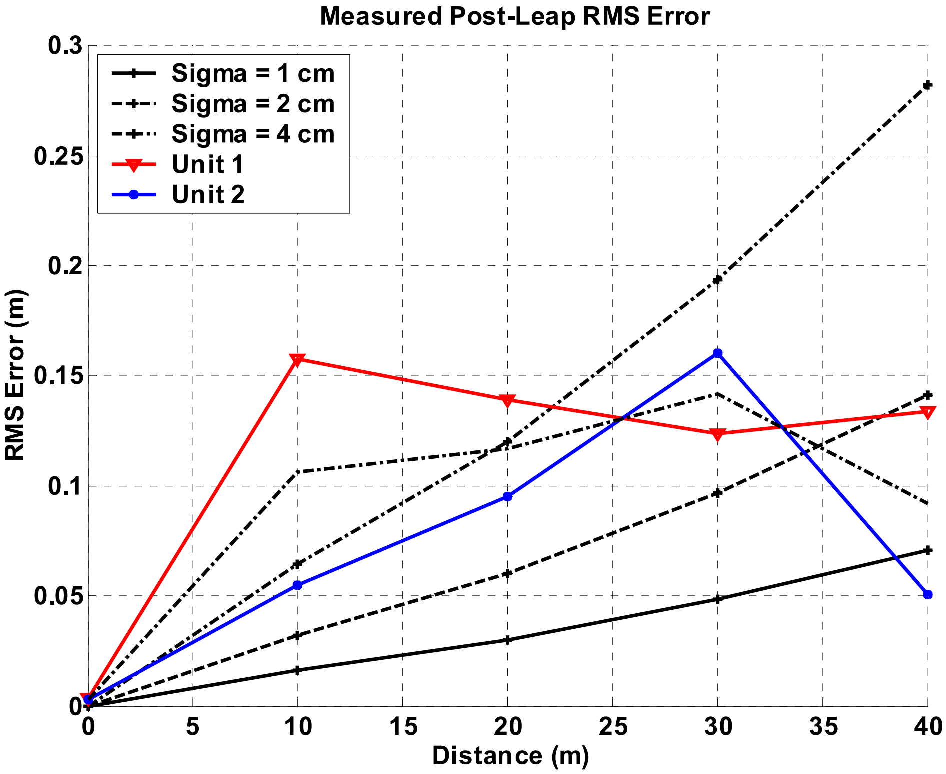

Figure 5.13 Measured Error Statistics and Model Covariances

The main reason for the discrepancy between measurements and theory is the model's assumption of measurement variance. While the sum-difference phase measurements had standard deviations of ~1cm (Chapter 3), this value does not take into account potentially uncorrected cycle slips in the measurements. We could increase our confidence in the model by inflating the measurement variance to envelop biases introduced by cycle slips.

5.5 Summary

This chapter listed the design considerations that eventually lead to a hardware implementation for GPSTs needed for the Leapfrog Navigation System (LNS). GPSTs were built using off-the-shelf components, and CMC Allstar GPS receivers, Integrinautics IN200c pseudolites and Proxim RangeLan2 radios were chosen for the given implementation.

LNS was tested using 4 GPSTs in a 10m x 10m original configuration. The array was moved a total of 40 meters (4 leaps of 10 meters), and the average absolute position errors never exceeded 16 cm.

Planetary exploration is one of the key applications for the Leapfrog Navigation System, and the next chapter will describe a full LNS Mars mission design.

6 Leapfrog Mars Mission Design

This chapter will look at a detailed Mars mission design using the Leapfrog Navigation System (LNS). A Mars mission is one of the most challenging operational scenarios for LNS and puts extra constraints on the system as far as autonomy is concerned. Several design choices and challenges will be addressed in this Chapter, so potentially deploying the Leapfrog Navigation System to the red planet will not have to be a complete leap of faith.

Chapter 6.1 will describe design considerations and choices both for RF systems and for mechanical integration with suitable rovers. The next two chapters are dedicated to operational procedures for LNS deployment and to planning paths for a mission. The final chapter will look into options for augmenting the bare-bones Leapfrog Navigation System.

6.1 Design Considerations

Mars has a diameter of 6,787 km, and a gravitational pull approximately 30% of that of Earth. The Martian atmosphere is thin, 7.5 mill bars (1013 on Earth), and consists mainly of CO_2. However, sandstorms with wind speeds of several tens of meters per seconds occasionally engulf the entire planet. Its arid climate in many ways resembles some deserts on Earth. Mars' orbit is 1.524 astronomical units from the Sun, and the Martian day is slightly longer than an Earth day.

6.1.1 Navigation Technology Selection

While sand storms may severely limit range for lasers and other optical equipment, radio frequency equipment would be less affected. Penetration of dust in the atmosphere increases with increasing wavelength, but so does antenna size. One could in theory pick any frequency for use with a navigation system, since Mars to this date has no mandated spectrum plan (that we are aware of). However, designing hardware from scratch can often prove extremely costly and time consuming, so use or adaptation of existing technology would be preferable.

In addition to attenuation from dust, the greatest technical challenge for a radio-navigation system will be to deal with ground-reflection multipath. Ultra-WideBand technology has very favorable multipath characteristics, but is to date not found in any off-the-shelf products. This may well change soon, but it might mean that UWB will not be a viable technology for a Mars mission navigation system for some time to come. GPS, on the other hand, is proven technology with over a decade of operations and tens of millions of user sets. Chapter 3 in this thesis showed that the GPS signal structure may be weaker in multipath than UWB. However, fairly representative outdoor channel modeling tests showed GPS carrier phase cross-range standard deviations in the order of centimeters. Such measurement accuracy would more than suffice for LNS operation, although carrier phase cycle slips may make this option less than robust.

6.1.2 Dual-Frequency GPS

Dual frequency GPS technology could be used to combat multipath fading. Instead of calibrating delays through the ionosphere, a second frequency would provide spectral diversity. This would make the system more robust since the L2 (1227.60 MHz) frequency would be affected differently by multipath than L1 (1575.42 MHz). Using the single reflection multipath model from Chapter 2 with a reflection coefficient of 0.5, we get the carrier phase errors as function of multipath excess distance for L1 and L2 shown in Figure 6.1.

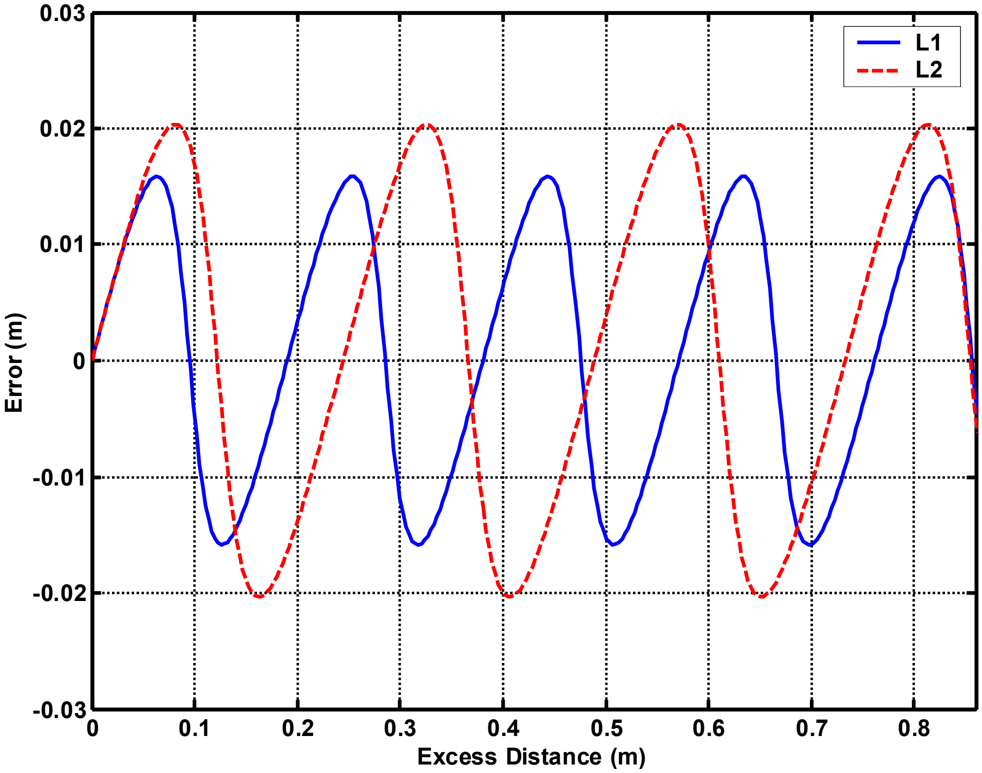

Figure 6.1 Carrier Phase Errors on L1 and L2

The figure above shows the periodicity of multipath effects on the two different wavelengths. The L2 frequency has greater worst-case errors than L1 since it has the longer wavelength.

The total received signal amplitudes as function of excess distance is plotted in Figure 6.2 on the next page. From Figures 6.1 and 6.2 one can find that the two frequencies rarely experience severe fading at the same time.

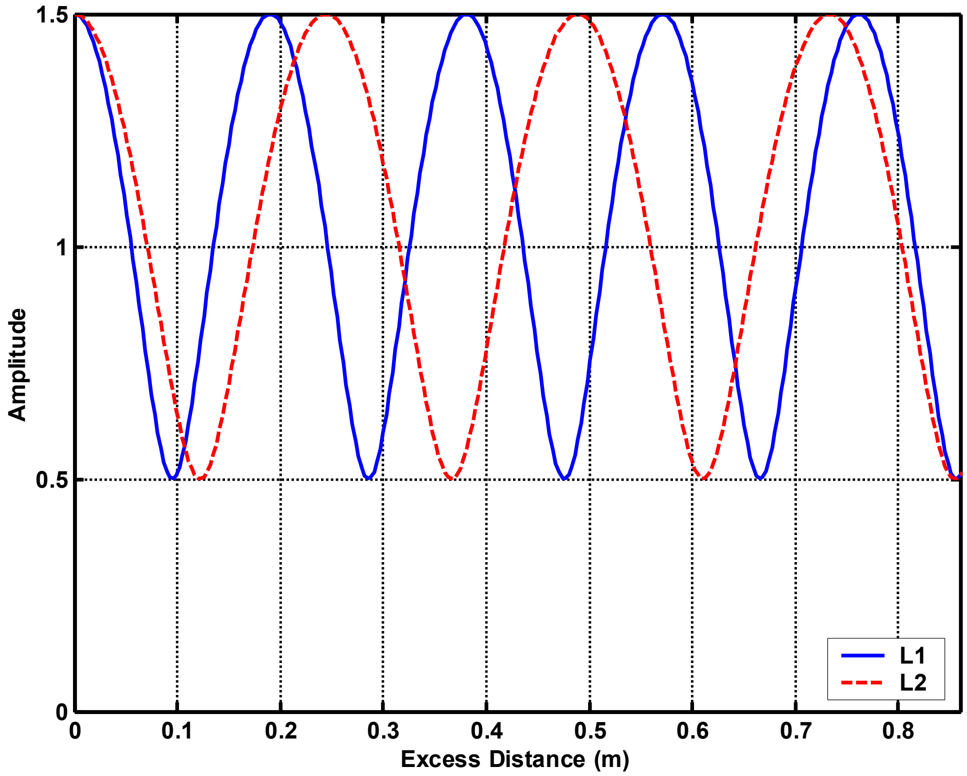

Figure 6.2 Received Signal Amplitudes L1 and L2

A second frequency also enables quicker and more robust wide-laning techniques [49] for carrier cycle ambiguity resolution. Wide-laning basically works by tracking other modulation products than just L1 or L2. The L1-L2 beat frequency, L_{WL}, has a wavelength of ~86 cm (also noticeable in Figures 6.1-6.2).

Compared to the 19 cm L1 and the 24 cm L2 wavelengths, use of L_{WL} decreases the initial cycle ambiguity search space tremendously. Practically speaking, cycle ambiguities would be resolved sequentially. First, the initial ambiguity space would be searched using L_{WL}. Then, a smaller area/volume of size 86 cm could be searched using L1 and/or L2. Figure 6.3 depicts the granularity of the two ambiguity search spaces (only L_{WL} and L1 shown). The solid lines are spaced at the L_{WL} wavelength of 86 cm, and the dotted lines have the L1 spacing of 19 cm. The error ellipses are only meant to show relative scale of the position solutions based on L1 and L_{WL} respectively.

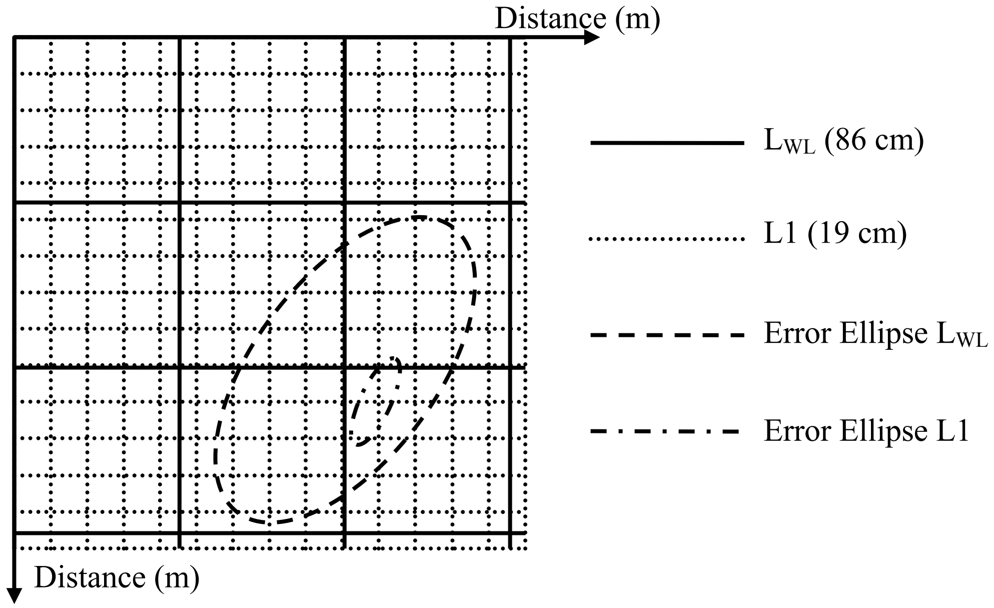

Figure 6.3 L_{WL} and L1 Ambiguity Search Spaces

L_{WL} measurements could be used in the positioning algorithms directly, but tracking of the modulation product is less robust than tracking either of the fundamental frequencies. The measurement variance of L_{WL} is equal to the sum of the variances for L1 and L2.

The gains of using two frequencies come at the expense of added hardware complexity and cost. However, dual-frequency GPS hardware is already readily available (although not space-grade) in GPS Real-Time-Kinematic (RTK) systems. Carrier phase cycle slip concerns would mandate the use of more than one frequency for an LNS Mars mission.

6.1.3 Antennas and Range

The Leapfrog Navigation System could easily be implemented on a slew of rover types, from the 1996 Sojourner-class [16] to a current Mars Exploration Rover (MER) [50] class of vehicles. The only external modifications to the rovers would be the addition of an antenna boom. A simple, robust and elegant solution to this problem would be to have a fixed length boom hinged to the side of the rover. In this way the antenna could easily be folded during the trip to Mars. A simple spring mechanism would suffice for erecting the antenna once a rover is deployed onto the surface. While vertical dipole antennas could be mounted to the boom, there is also a choice of making the boom itself into an antenna. Slot antennas [51] have very similar radiation patterns to dipoles. A slot antenna can be made by cutting out a sliver of material from a metallic pipe. For best match, the slot should be ½ wavelengths long, and it should be fed at the sides of the center point, as in the figure below.

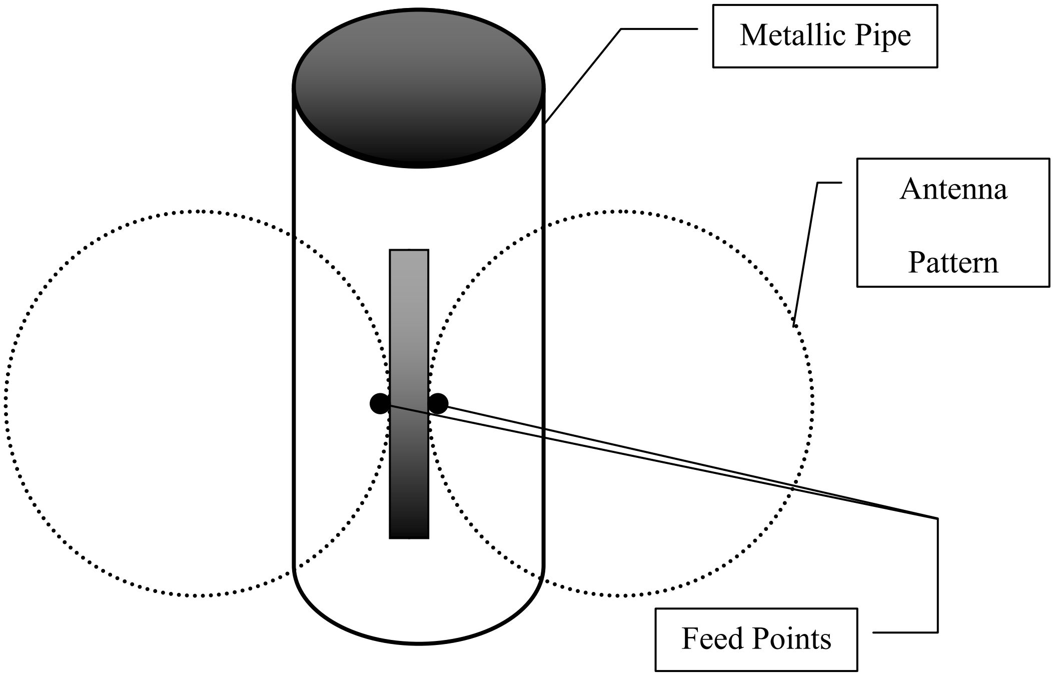

Figure 6.4 Slot Antenna with Radiation Pattern

It would be advantageous to mount the antennas as high from the ground as possible to get the best possible line-of-sight range. Since Mars has such a thin atmosphere, its radio horizon will more closely match the true horizon than Earth[6]. Figures 6.5 shows that this range, *d*, depends on the antenna heights (h_1, h_2) and radius of curvature, ρ, of the planet.

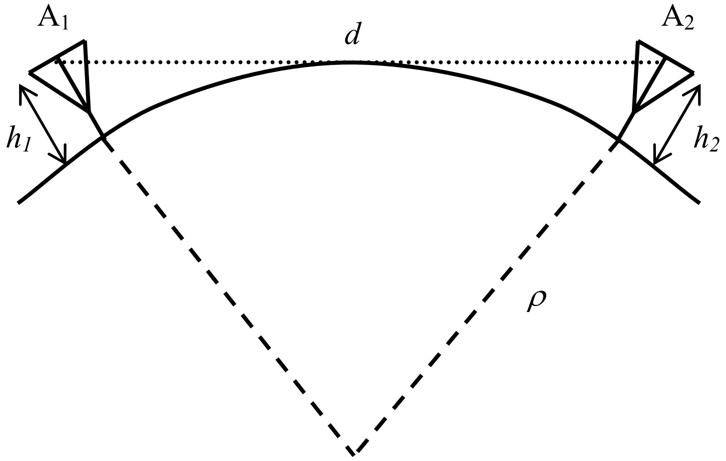

Figure 6.5 Line-of-Sight Range Calculations

Figure 6.6 shows the line-of-sight range for increasing heights of h_1 and h_2 (same heights). Figures 6.5 and 6.6 represent pure geometry. However, received signal power, hence true range, is likely to follow the trend given by Equation 3.4. This equation comes as a result of multipath at grazing reflection angles has Fresnel reflection coefficients near -1 almost independent of the dielectric constant of the reflector [42] (Martian soil in our case). Keeping received power the same while doubling the range means doubling both antenna heights, or making just one of them 4 times taller! This is often referred to as the “height gain” of Equation 3.4.

---

[6] Due to the index of refractivity of the atmosphere.

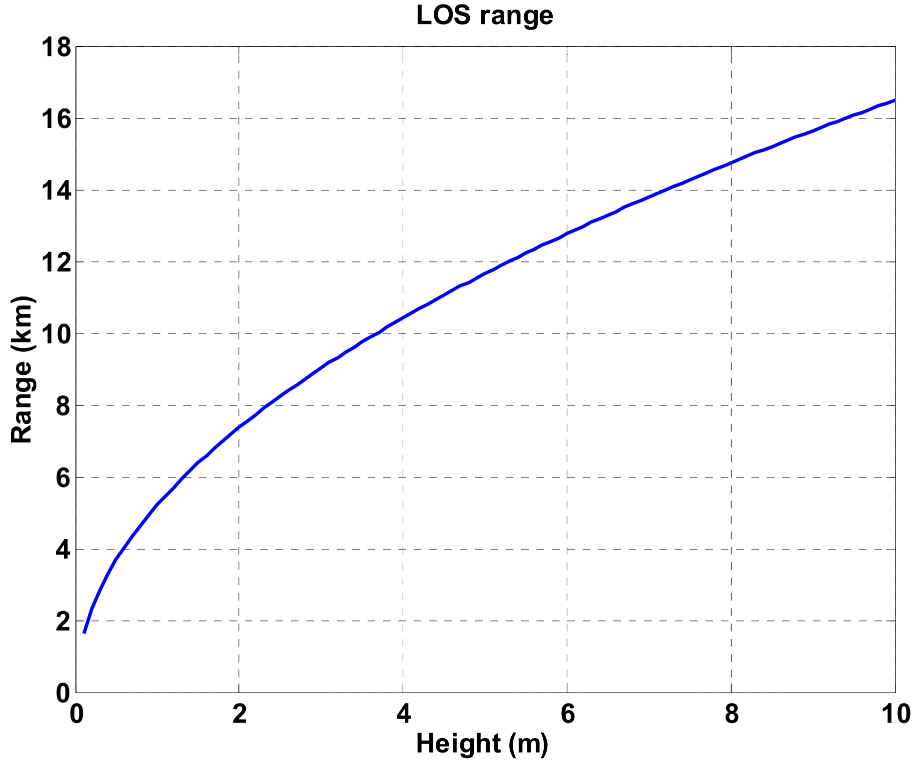

Figure 6.6 LOS Range on Mars

While the previous paragraph made the case for tall antennas, this parameter must be traded off against weight, change in center of mass, wind-drag flipping moment, and general storage space concerns. A thicker antenna boom would be good because it would provide for less dynamic flexure, hence less variation in cross-range. However, a thicker boom would also mean a greater change in the rover center of mass and more weight total. In turn this would limit the inclines the rover could negotiate, and it would reduce any margins in total launch weight[7]. Still, variations in terrain are likely to dominate these effects.

---

[7] Since 1 lb delivered to Mars takes ~1 ton of gross launch weight, weight is worth its weight in gold.

Since Mars occasionally experiences strong storms, there may be concerns over wind drag from an antenna boom. However, offline calculations show that the drag from a 2 ft long ½ in thick cylinder (antenna boom) is significantly less than 1 Newton in the thin Martian atmosphere.

By adding motors to an antenna boom, there is also the possibility of having it double as a self-righting mechanism. Although this option borders on featuritis[8] and increases system complexity by several orders of magnitude, having a self-righting rover may well increase the overall probability of mission success.

6.2 LNS Deployment and Initialization

This chapter describes the process of initial deployment of LNS to Mars, and the following assumptions are made in the following:

- 4 similar rovers of Sojourner-class, all with dual-frequency GPS transceivers
- The lander and/or at least one rover have a set of stereo vision cameras.
- The lander is also outfitted with a GPS transceiver.

Final descent to Mars may happen in a similar way to the Mars Pathfinder Mission of 1996. A lander aero-brakes through the atmosphere, retro-rockets slow the descent even further, and final touchdown is padded through the use of air bags. One possible configuration of the lander is shown in Figure 6.7.

---

[8] The "illness" where too many features are added to a single product, e.g. making a combined toaster oven and TV.

Once the lander has opened its petals, the 4 rovers can be driven to suitable initial positions, e.g. in a star-configuration around the lander. One rover would then be driven around the other units. LeMaster [21] showed that this technique could be used to calibrate line biases, solve carrier cycle ambiguities, and find the initial positions of all units relative to each other.

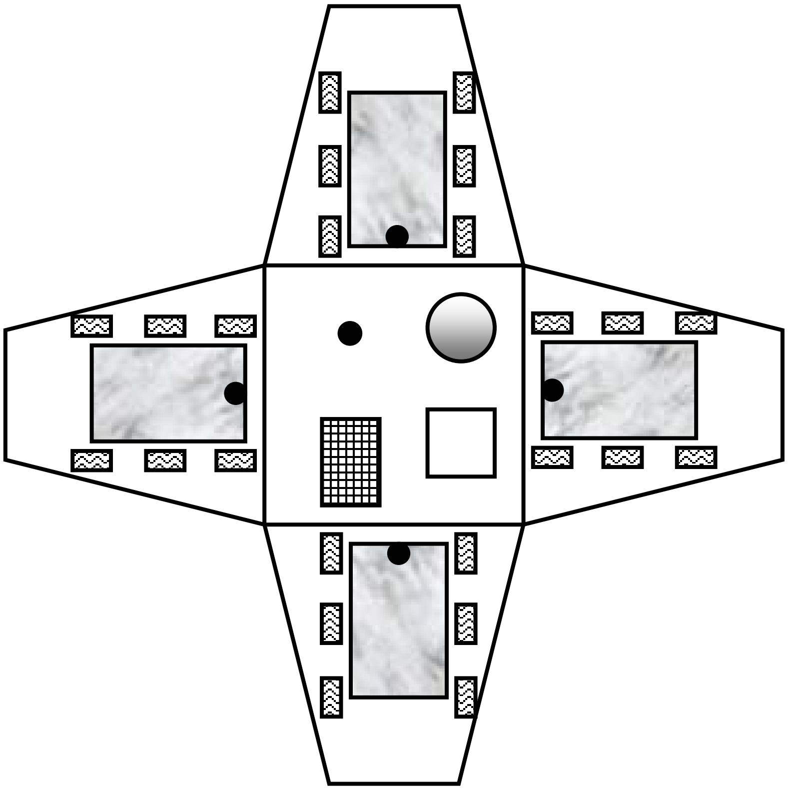

Figure 6.7 Lander with Four Rovers

After finding all relative positions, the total array should be aligned with the principal Martian directions. This operation is essential in order to "match up the map with the terrain." Mars has no magnetic field, so unlike Earth, a simple compass would not work. Going back to first principles, the Sun could be used to align the array. There are two parts to this problem: finding the attitude of one unit, and finding the true headings from that unit to the other units in the array.

One way to solve the first part of the problem would be to have stereo-vision cameras track a shadow (e.g. of their own antenna boom) over a full day. Sun dials require a smooth projection surface, but range/angle measurements from a stereo-vision system could correct for most errors stemming from surface roughness. The sun dial approach would also require the camera system to be outfitted with angle sensors, e.g. optical encoders, so the vehicle body coordinate frame could be rotated into a local East-North coordinate frame.

Once a unit is aligned with East and North, the same camera system could be used to find the heading directions to the other units. Heading measurements to either of the other units would suffice, since the relative positions of all units in the array already had been calculated. However, getting measurements from all units in view would greatly increase confidence in the alignment procedure. Furthermore, the range/angle measurements from a set of stereo-vision cameras would provide a second set of relative position solutions. Figure 6.8 shows the two coordinate rotations needed to align the array with East and North.

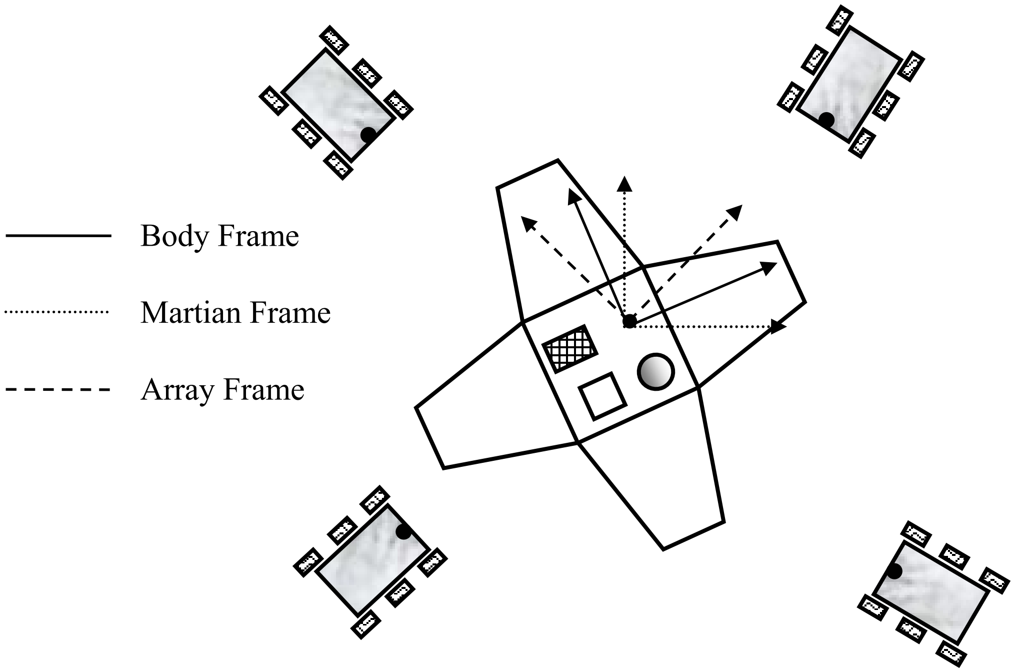

Figure 6.8 Rotations of Body and Array Frames into Martian Frame

6.3 Path Planning

In Chapter 2 we found that 3 rovers are the absolute minimum number of units required for a Leapfrog Navigation System. However, this also means that the 3 rovers will line up once for every leap, and that creates a singularity in the positioning algorithms. We seek to find the effects of geometry on pre-leap positioning accuracy for the 3-rover case. We can create a map of HDOP by successively probing a grid of possible mobile unit locations given the locations of two stationary units, like in Figure 6.9.

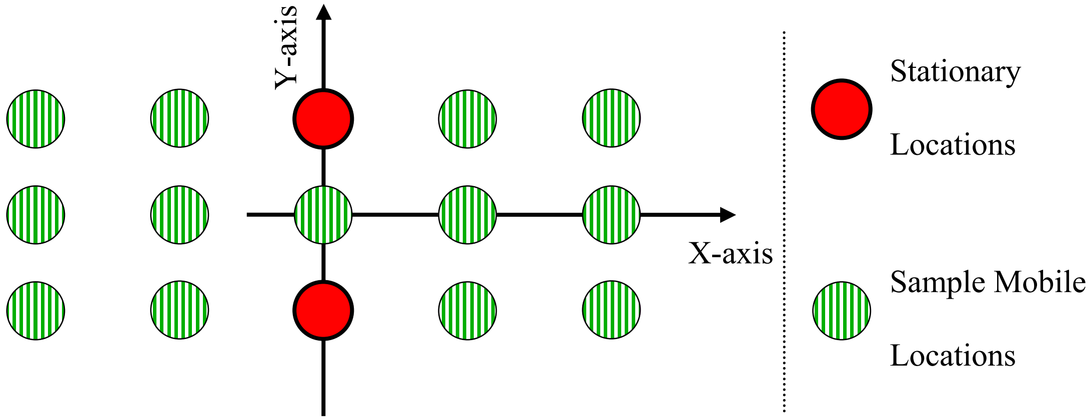

Figure 6.9 HDOP Calculation Setup

Figure 6.10 shows the corresponding HDOP for 3-unit LNS with horizontal distances normalized by the baseline distance of the stationary units.

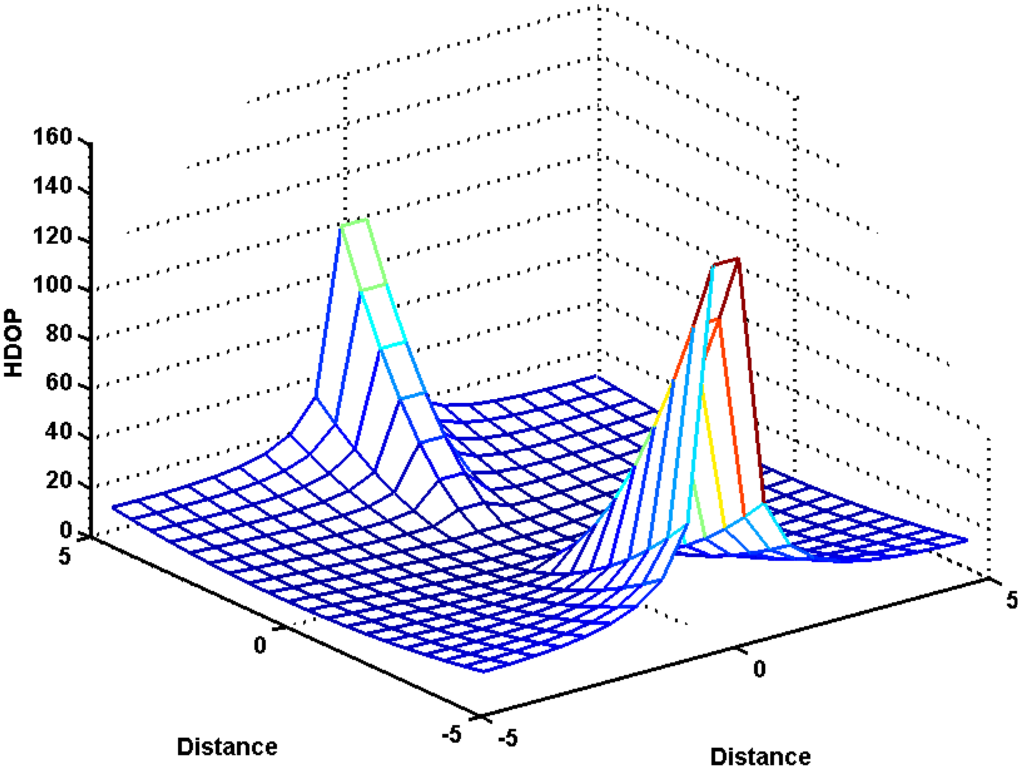

Figure 6.10 Three-Unit LNS HDOP

The resulting singularity in the navigation algorithm could be alleviated by incorporating such things as odometer readings and laser-range measurements in the position solutions. Note that positioning outside the bad HDOP areas still work well, as long as there is an external way of discerning which side of the static baseline the single mobile unit is. Figure 6.11 shows a possible movement pattern for 3-unit LNS where the mobile unit always passes right between the two stationary ones and ends up in its mirror position. We can infer from Figure 6.10 that this direction of travel has the smallest HDOP gradient.

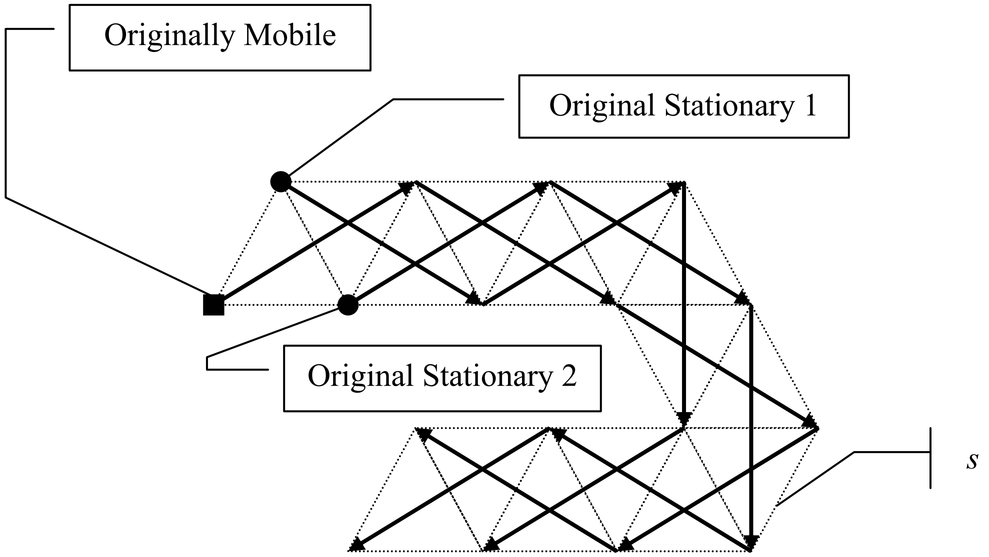

Figure 6.11 Three-Unit LNS Movement Pattern

Each move takes a rover a distance $s/2$ beyond the farthest stationary unit. However, the rover must travel a total distance $\sqrt{3/2} \cdot s$ to get there. Thus, the equilateral movement pattern limits total array speed to 41 % of the operating speed of each unit.

Going with a 4-unit Leapfrog Navigation System would provide several benefits; the greatest of which would be tolerance towards single unit failures. Total failure of one unit would still leave three others operational, and that number meets the minimum requirements for LNS (given additional measurements, e.g. odometer, stereo vision, inertials etc.). One possible movement pattern for 4 unit LNS is depicted in Figure 6.12.

The two mobile units must be staggered as they cross the baseline between the two stationary units to avoid singularities in the navigation algorithms. If the rovers were to follow an elliptical trajectory with semi-minor axis 1/3 of the semi-major one, then total array movement speed approaches 48 % of rover speed as the stagger goes to zero. Since two units always remain still, the theoretical maximum array speed is 50 %.

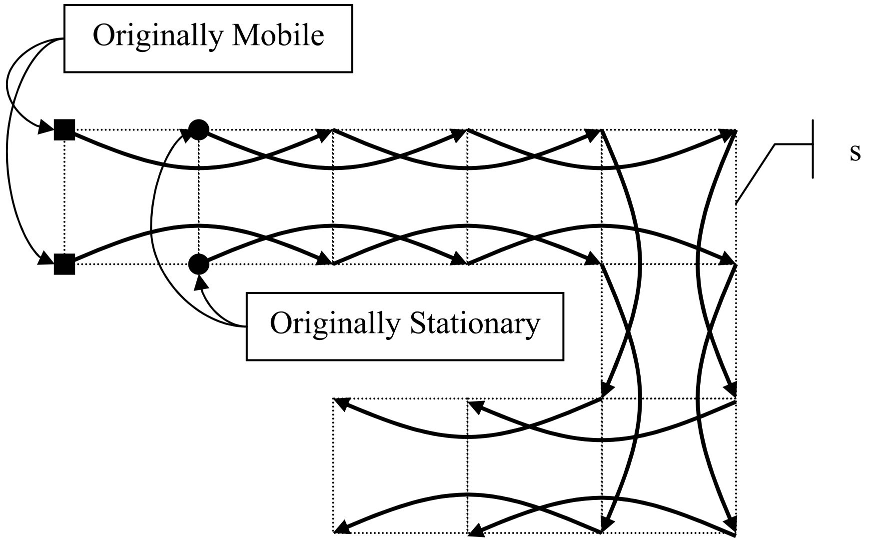

Figure 6.12 Four-Unit LNS Movement Pattern

LNS may provide a very efficient way for conducting science experiments while traversing the Martian landscape. The very nature of LNS requires two units to stand still at all times, which should provide ample time for taking soil/rock samples etc. Such samples could then be analyzed en route to the next location. In this way, LNS could facilitate a virtual game of tag for solving a science mission.

Having multiple LNS rovers means that each one could be outfitted to provide a wider spectrum of scientific instruments than what would be possible to fit into a single vehicle. Complimentary sets of implements may include scoops for handling soil samples, and drills for taking rock samples. Since a Leapfrog Navigation System may move out of communication range with the lander, one rover could also be outfitted with a high gain antenna for communications with an orbiting spacecraft.

Having accurate relative positions and a group of rover opens the door for such things as antenna pattern shaping [52] and distributed computing. Multiple antennas on each rover would enable direction-finding or attitude calculations.

6.4 Positioning Augmentations

LNS may be suited for several operational scenarios; from surveying a larger area to providing guidance from a landing site to specific features in the Martian landscape. We will study two approaches on how to augment bare-bones LNS positioning; an external Doppler measurement technique, and a method for post-processing the LNS data.

6.4.1 Martian TRANSIT

Most Mars missions to date that involved an actual landing have also included an orbiting spacecraft. TRANSIT-like [53] position solutions may be found by tracking the Doppler frequency of signals transmitted from the orbiter during an overhead pass. This would require the orbiter to transmit its “known” positions as well, and a network of reference stations on the planet surface would be required for accurate orbit determinations. A less accurate method, but currently used, may involve use of the NASA Deep-Space Network [54,55].

When TRANSIT was operational it yielded stand-alone position accuracies in the 20-30 meter range. In differential mode, this accuracy improved to about 1 meter. Differential operations have less strict requirements on orbiter location, and the relative location of the lander to the group of rovers. In the cases where the rovers are outside communications range with the lander, raw data could be stored for post processing of locations upon return to the lander. Conversely, the differential corrections could be transmitted via the orbiter.

The greatest disadvantage of the TRANSIT approach comes in terms of availability. A single orbiter may be in view only once or twice per day, so basing navigation on just the space vehicle may not be practical. However, differential TRANSIT may be a perfect match for LNS. Absolute position error accumulates as a function of number of leaps in LNS. External position fixes through Doppler measurements from an orbiter would effectively reset LNS error accumulation every time the space vehicle passed overhead. The LNS position errors may grow beyond the 1-2m expected accuracy of a differential TRANSIT solution, and the combined position error may have the following time trace.

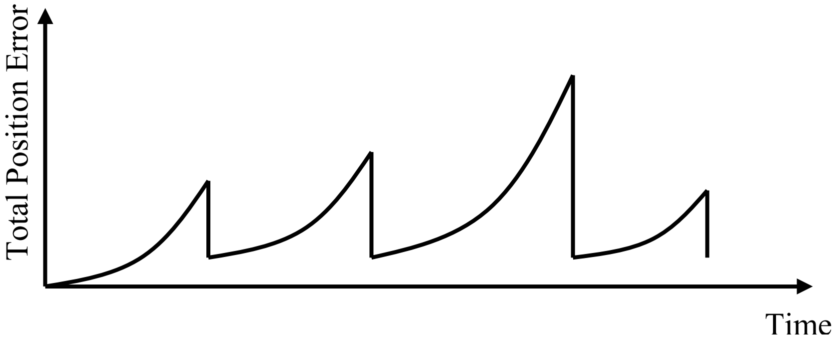

Figure 6.13 Updated LNS (Saw-tooth)

This is very similar to the implementation gain of combining an Inertial Navigation System (INS) with GPS [56].

The TRANSIT augmentation would work particularly well on one-way missions, where a group of rovers are sent out to explore areas far from the original landing site.

6.4.2 LNS Re-initialization and Back-propagation

From Chapter 4 we find that a sample return mission could have rovers travel up to ~7.5 km from the lander and still find their way back to within 10 meters. A re-initialization could be performed upon return, and the aggregate LNS error could be calibrated. Position error estimates could be lowered during the entire excursion by using symmetry and propagating the re-initialized position solutions backwards. This is possible since the forward and backward paths yield two independent positioning solutions for each location.

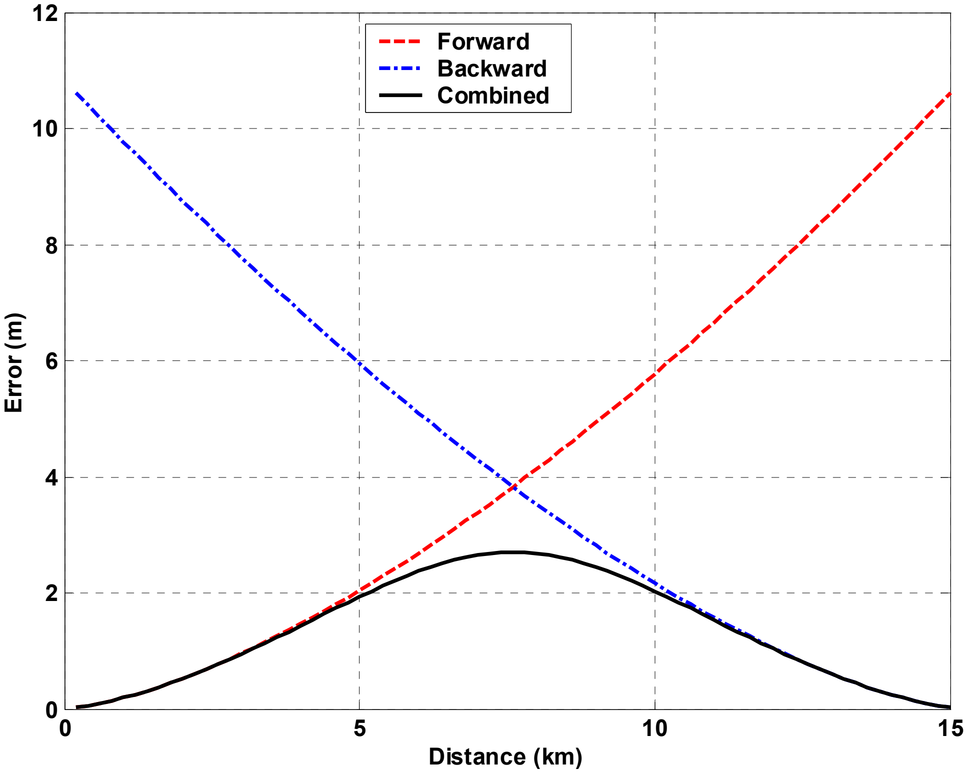

Figure 6.14 LNS Error Growth after Re-Initialization

Figure 6.14 clearly shows the gain of combining the two measurement paths. The dashed line is the forwards direction, the dash-dotted line is the backward direction, and the black solid line is the combined error estimate given by Equation 6.1 [57].

$$\frac{1}{\sigma_{total}^{2}} = \frac{1}{\sigma_{forward}^{2}} + \frac{1}{\sigma_{backward}^{2}} \qquad \textbf{Eq. 6.1}$$

The added information from a re-initialization can be used to extend the range of LNS for a given tolerance on absolute position. However, the above calculations require LNS to find the way back to the lander in the first place (effectively given by Figure 4.7).

Given the advantages of re-initialization, surveys over larger areas should be done in a star pattern, shown in Figure 6.15.

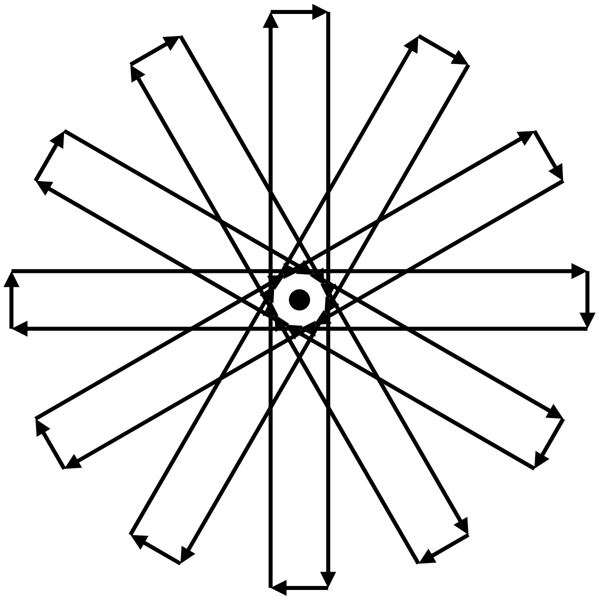

Figure 6.15 Star Survey Pattern

While this method ensures minimal error growth, it also means heavy overlap in the area close to the lander.

6.5 Summary

This chapter described the process of designing a Leapfrog Navigation System Mars mission. Such a mission should utilize dual-frequency GPS transceivers because of the added cycle-slip robustness. Having 4 rovers would be very beneficial for mission robustness, although 3 rovers would be the absolute minimum requirement.

By adding a GPST with the lander, one has the option of re-initializing LNS solutions after returning from an excursion. Combining forward and backward propagated solutions would significantly improve the post-processed positioning errors during the entire expedition. Another technique for augmenting LNS may be found in using Doppler measurements from an orbiter for differential TRANSIT. Such additional information could be used to reset LNS error growth, which would be particularly important during one-way missions.

7 Conclusions and Future Work

This chapter summarizes all results and contributions. Additionally, the chapter suggests improvements to the current Leapfrog Navigation System (LNS) architecture as well as directions for future research.

7.1 Summary of Results and Contributions

7.1.1 Leapfrog Navigation System

The main contribution of this research is the conception, design, implementation and experimental demonstration of the Leapfrog Navigation System. LNS calculates relative positions of mobile navigation units based on cross-range measurements from an array of stationary units in addition to cross-range measurements among the mobile units themselves. Absolute references to initial unit locations are kept by separating the group of navigation units into two teams, and alternating the teams between being stationary and being mobile.

LNS performance was analyzed through its positioning covariance statistics. The absolute position errors during team-wise advances grow as function of the topology of the navigation units, the number of leaps (mobile/stationary alternations) and the fundamental ranging accuracies. Models of those cross-range errors were created based on the field experiments described in Chapter 3. The results of simulations of one indoor (UWB) and 2 outdoor (GPST) scenarios are listed in Table 7.1.

	Indoor UWB 2m Baseline	Outdoor GPST 10m Baseline	Outdoor GPST 100m Baseline
Leap distance (m)	2.5 / 5 / 7.5 / 10	10 / 20 / 30 / 40	100 / 200 / 300 / 400
Range in km at 10m error bound	.14 / .17 / .2 / .22	1.1 / 1.4 / 1.7 / 2.2	11.4 / 14.4 / 5.6 / 2.9

Table 7.1 Simulation Results for Various Baseline/Leap-Distance Combinations

A prototype LNS was constructed using GPS transceivers based solely on off-the-shelf components. Outdoor field tests with 2 pairs of GPSTs in a 10m-by-10m configuration yielded the following results:

	Results Unit 1 / Unit 2	Simulation Sigma = 1cm	Simulation Sigma = 2cm	Simulation Sigma = 4cm
Error at 10 m	15.8cm / 5.5cm	1.6cm	3.2cm	6.4cm
Error at 20 m	13.9cm / 9.5cm	3.0cm	6.0cm	12.0cm
Error at 30 m	12.4cm / 16.0cm	4.8cm	9.7cm	19.3cm
Error at 40 m	13.4cm / 5.0 cm	7.1cm	14.1cm	28.2cm

Table 7.2 Field Test Results and Simulations

While the first unit in the above tests seemed to have a somewhat constant error, the second unit's errors were bounded by the simulations that assumed a 4 cm fundamental cross-range error. Un-corrected cycle slips in the field tests may well explain the discrepancies between the results and the nominal simulation scenario.

7.1.2 The Navigation Channel

Multipath may well be the largest source of errors for ground based radio-navigation systems such as LNS. Multipath directly biases ranging measurements, but it also comes in form of power fading, which instigates GPS carrier cycle slips.

Both indoor and outdoor navigation channel measurements were performed to find how multipath affects the ranging measurements of GPS and UWB signals. Indoor measurements at the Stanford University LAAS Lab showed multiple occurrences of signal reflections having stronger amplitudes than direct signals. Some of these cases could be explained by attenuation through a wall for the direct signal component, while the reflected ones came in through a door opening. Other cases were correlated to the realistic, and non-isotropic, gain patterns of the transmit and the receive antennas used in the tests.

Multipath effects were analyzed in terms of average delay and delay spread; concepts borrowed from communication systems. However, this work introduces a new metric, Strongest Arrival Delay, which is the delay between a direct signal and the strongest signal component. A maximum SAD of ~18 ft was measured in the indoor tests, while outdoor tests yielded a worst case SAD of only ~1/2 ft. SAD is also coarse measure of range error for GPS-like navigation systems.

Multipath introduces fading in any kind of spread spectrum systems. Thus, deteriorating signal detection and tracking. For spread spectrum navigation systems, multipath additionally biases the fundamental ranging measurements. In GPS this effect is described in multipath envelope plots, e.g. Figure 2.15.

Ultra-WideBand technology in its current state works by transmitting very short pulses instead of continuously modulating information onto a carrier signal. These pulses typically last in the order of 1 ns, and a direct signal and can be distinguished from multipath components with excess delays of more than one pulse width. In this way, only ultra-close multipath affects signal detection and tracking for UWB systems. Simulations in Chapter 2 suggest worst case ranging errors of ~6 cm for a 1 GHz wide UWB signal in the presence of a single reflection with half its amplitude.

7.2 Future Work

Several improvements can be made to the current Leapfrog Navigation System prototype. The first and foremost augmentation should be to bring LNS from a two-dimensional to a three-dimensional system. The only way to accomplish this is to get measurements out of the plane of the current setup. Masa Matsuoka [58] has already done work with placing an additional GPST in a basket under a helium balloon, as shown in Figure 7.1. There may however be practical difficulties with flying a balloon in high winds or in thin atmospheres, and other options should be researched, too. Autonomous planes have been suggested for Mars missions [59], and such craft could potentially be outfitted with ranging devices.

As suggested in Chapter 6, a differential TRANSIT-like system could be used to contain error growth for an LNS Mars mission. While such an augmentation by itself would provide 3-D positioning, Doppler based solutions would only be very sparsely available. Alternatively, re-initialization and backward post-processing of LNS data can also be used to reduce error-growth for a round-trip mission.

Figure 7.1 Masa's Helium Balloon

For use on Earth, LNS could easily be integrated with regular GPS. In the same way as a TRANSIT-like system, GPS could be used to update position solutions during times with good SV availability. Integration with GSP has many advantages beyond reducing error growth. First of all, it gives LNS a reference system, WGS-84, that works with local maps. Integration also removes ambiguous solutions from the system, e.g. whether a unit is above or below the plane described by three other units.

Combining cross-range measurements among a group of mobile units with pseudorange measurement from GPS satellites gives a combined set of navigation equations which generally has many more measurements than unknowns [60]. This can be used either to improve the combined position accuracy, or it can be traded off with availability. A combined LNS/GPS unit with limited view of the sky might still find its position with help of cross-ranges from a few of its neighbors.

The practical implementation of the LNS GPS transceivers also has room for improvements. Currently, the receiver and transmitter parts have separate antennas. Chapter 4 showed that antenna separation only produced fairly benign range biases in a 2-D projected system. As one antenna pair travels out of plane in a 3-D system, the corresponding range bias will start to approach the tx/rx antenna separation. Collocating the transmit and the receive antennas would remove biases due to antenna separation as well as biases due to antenna tilt. However, antenna separation is also a very simple way of introducing signal isolation between the transmitter and the receiver. In the field test described in Chapter 5 both pseudolites (PL) and satellites were tracked simultaneously, although the relatively high powered (1μW) PLs saturated the receivers. Too much PL power was found to completely jam the receivers, though. Thus, using a single antenna requires a new technique for signal isolation. This objective could be accomplished by increasing the receiver's total dynamic range (requires receiver HW modification), or by synchronizing the RTCM pulsing sequence of the PL with a set of RF switches, an RF coupler and an attenuator. Figure 7.2 shows such an active blanking implementation of a single antenna GPS transceiver.

When the pseudolite RTCM sequence is turned on, the antenna and the receiver switches are turned to the PL side. During this time interval the receiver only sees its own PL. At all other times the two switches are turned to their opposite positions, and the receiver is connected directly to the antenna. After initial adjustments the attenuator can be fixed to a value where the receiver works normally even in the presence of its own

PL. Care has to be taken in order to ensure sufficient isolation of other signal paths from the PL to the receiver.

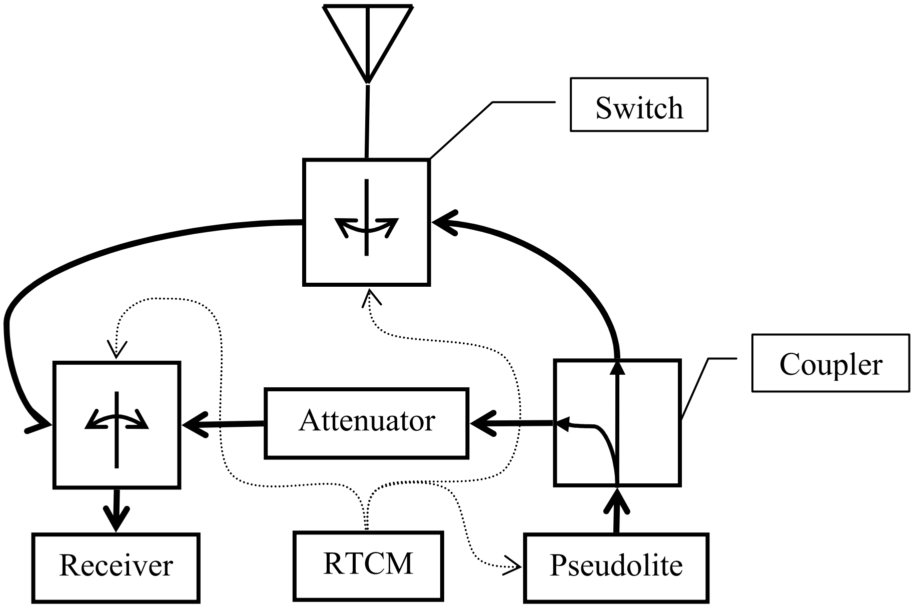

Figure 7.2 Single-Antenna GPST Configuration

The setup used for the LNS tests in Chapter 5 used a dipole transmit antenna and a Mini-Arinc patch receive antenna. The patch antenna is circularly polarized, and this gives rise to carrier phase cycle wind-up as two GPSTs are moved around each other. A linearly polarized receive antenna, such as a dipole or slot antenna, would solve the cycle wind-up problem, but it comes at the cost of increased fading. This approach was tried but found impractical in the previously mentioned field tests. These tests used GPS satellites to provide synchronized sampling of carrier phase on multiple receivers. A vertical dipole antenna has its gain pattern null towards zenith and its maximum gain in the horizontal plane. This de-emphasized high elevation SV signal strengths beyond the point of tracking.

The use of GPS to synchronize LNS obviously means that it is a less than autonomous system. The Orion receivers were used in the previous versions of GPSTs, and all GPSTs in a network were synchronized to a primary pseudolite. This approach is completely independent of standard GPS, but the implementation turned out to be rather cumbersome in real use. The off-the-shelf approach used in this work was meant as proof of concept for the Leapfrog Navigation System. As mentioned previously in this chapter, a regular GPS receiver, such as the CMC Allstar, lends itself easily to integration of LNS and regular GPS.

A custom built GPST definitely still deserves a second look, since it may offer much greater flexibility in design than any GPS equipment currently on the market. One improvement to the current design would be to tie the transmitter and receiver parts in a GPST to the same clock. Equation 2.5 for two GPS transceivers gives

$$\begin{aligned} \phi_j^{(k)} &= d_j^{(k)} + B^{(k)} - b_j + l_j^{(k)} + N_j^{(k)} \cdot \lambda_{L1} + \upsilon_{\phi,j}^{(k)} \\ \phi_k^{(j)} &= d_k^{(j)} + B^{(j)} - b_k + l_k^{(j)} + N_k^{(j)} \cdot \lambda_{L1} + \upsilon_{\phi,k}^{(j)} \end{aligned} \qquad \textbf{Eq. 7.1}$$

The top equation has GPST *k* act as transmitter and GPST *j* as receiver, and the bottom equation has those roles reversed. The common clock option means setting $B^{(k)} = b_k$ and $B^{(j)} = b_j$ in Equations 7.1, and adding the two measurements yields

$$\phi_j^{(k)} + \phi_k^{(j)} = 2 \cdot d_j^{(k)} + l_{jk} + N_{jk} \cdot \lambda_{L1} + \upsilon_{\phi,jk} \qquad \textbf{Eq. 7.2}$$

Thus, only two measurements are needed to generate clock-free cross-ranges. Going from double-difference to single-difference measurements means halving the number of noise terms. A common clock GPS transceiver would also have a much simpler single antenna implementation. Since a GPST receiver unit will not have to track its own pseudolite, only a single antenna switch is needed in the system, shown in Figure 7.3.

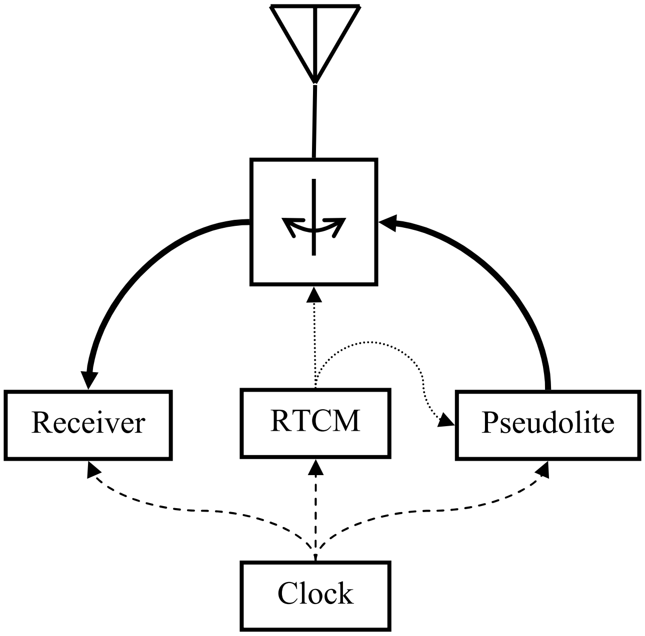

Figure 7.3 Common-Clock GPST Configuration

In the previous figure, the receiver PL is connected to the antenna only during its RTCM-pulsed transmissions. At all other times, the receive side is connected directly to the antenna.

A custom built GPST could also be based on the Software radio principle [61]. Signals from a fairly simple RF front-end could be sampled very fast and all signal processing could be done on a Field Programmable Gate Array (FPGA). Not only is this design modular as far as hardware goes, but an FPGA is also easily re-programmable for quick changes to tracking loop parameters etc. The SW radio approach should adapt easily to use in multi-frequency configurations. Having two or more frequencies [62] enables beat-frequency tracking for quick cycle ambiguity resolution, and different frequencies will be affected differently by multipath. A custom GPST may also apply a longer and faster PRN sequence, e.g. the 10.23 MHz P-code. The longer the sequence the more code-isolation between units, and the faster the chipping rate the better the code phase multipath performance.

In modernizing GPS and in deploying its European counterpart, Galileo, a new type of signal structure will be used, Binary-Offset-Carriers (BOC) [63]. These signal structures are classified by BOC(*m,n*), where *m* is the sub-carrier offset (in MHz) from center frequency and *n* is the chipping rate (in Mcps). BOC signals have favorable multipath characteristics to regular spread spectrum signals partially due to the inherent frequency diversity of the modulation scheme. While it may take a few years to see off-the-shelf equipment capable of using these signal upgrades, they are nonetheless intriguing for LNS.

While GPS carrier phase was shown to work fairly well in the LNS implementation described in this thesis, Ultra-WideBand technology may provide some improvements still. Not only will UWB be void of cycle-ambiguities, but it is also likely to be very robust towards multipath while providing ranging accuracies comparable to GPS carrier phase. There are still UWB interference issues to be better understood, and the UWB spectrum allocation is not yet set in stone. Based on the current FCC regulations, UWB systems are likely to have limited range. Nonetheless, UWB is very interesting for future implementations of LNS as well as other navigation architectures.

Appendix A

First, let us rewrite the 2-D version of Equation 2.10 in the following form.

$$\frac{\hat{\phi}_{m_1 s_1}}{2} = \left(d_{m_1,0}^{(s_1)} + \frac{\partial d_{m_1}^{(s_1)}}{\partial x_{m_1}} \cdot \Delta x_{m_1} + \frac{\partial d_{m_1}^{(s_1)}}{\partial y_{m_1}} \cdot \Delta y_{m_1} \right) + R \qquad \textbf{Eq. A.1}$$

The additional term, *R*, is the residual left after linearization, and we will estimate this residual using the second order term in the Taylor series expansion.

$$\begin{aligned}
R &\approx \frac{1}{2!}\left(\frac{\partial^2 d_{m_1}^{(s_1)}}{\partial x_{m_1}^2} \cdot \Delta x_{m_1}^2 + 2\frac{\partial^2 d_{m_1}^{(s_1)}}{\partial x_{m_1} \partial y_{m_1}} \cdot \Delta x_{m_1} \Delta y_{m_1} + \frac{\partial^2 d_{m_1}^{(s_1)}}{\partial y_{m_1}^2} \cdot \Delta y_{m_1}^2 \right) \\
&\approx \frac{1}{2!}\left(\begin{array}{l} \dfrac{\partial^2 \sqrt{\left(x_{s_1} - x_{m_1}\right)^2 + \left(y_{s_1} - y_{m_1}\right)^2}}{\partial x_{m_1}^2} \cdot \Delta x_{m_1}^2 \\ +2\dfrac{\partial^2 \sqrt{\left(x_{s_1} - x_{m_1}\right)^2 + \left(y_{s_1} - y_{m_1}\right)^2}}{\partial x_{m_1} \partial y_{m_1}} \cdot \Delta x_{m_1} \Delta y_{m_1} \\ +\dfrac{\partial^2 \sqrt{\left(x_{s_1} - x_{m_1}\right)^2 + \left(y_{s_1} - y_{m_1}\right)^2}}{\partial y_{m_1}^2} \cdot \Delta y_{m_1}^2 \end{array} \right) \\
&\approx \frac{1}{2! \cdot \left(d_{m_1}^{(s_1)}\right)^3} \left(\begin{array}{l} \left[\left(d_{m_1}^{(s_1)}\right)^2 - \left(x_{s_1} - x_{m_1}\right)^2 \right] \cdot \Delta x_{m_1}^2 \\ -2\left[\left(x_{s_1} - x_{m_1}\right)\left(y_{s_1} - y_{m_1}\right) \right] \cdot \Delta x_{m_1} \Delta y_{m_1} \\ +\left[\left(d_{m_1}^{(s_1)}\right)^2 - \left(y_{s_1} - y_{m_1}\right)^2 \right] \cdot \Delta y_{m_1}^2 \end{array} \right) \qquad \textbf{Eq. A.2}
\end{aligned}$$

In the equation above, a mobile unit, *m₁*, is nominally located at $\left(x_{m_1}, y_{m_1}\right)$, and a stationary unit, *s₁*, is located at $\left(x_{s_1}, y_{s_1}\right)$.

As an example, consider a case where we could tolerate a residual range error of 1 cm due to linearization. Let us further place the stationary unit at (0,0) and the mobile one at (10,0). We solve the equation on the next page to find the maximum perturbation.

$$.01 \approx \frac{1}{2! \cdot 10^3}\left(10^2 - 0\right) \cdot \Delta y_{m_1}^2$$

$$\Delta y_{m_1}^2 \approx .2$$

$$\Delta y_{m_1} \approx .45 \text{ m}$$

Similar limits for 2.5 and 100 meter baselines are .22 m and 1.41m respectively.

Appendix B

```
function gOut = Get_LNS_Gm_Matrix(positionStationary, positionMobile)

% Function Get_LNS_Gm_Matrix generates the Leapfrog Navigation System
% Gm matrix given position estimates of all mobile and stationary
% units.
% Inputs: Stationary units positions, mobile units positions
% Output: LNS Gm matrix
% Guttorm R. Opshaug 2/14/02

[rowS colS] = size(positionStationary);
[rowM colM] = size(positionMobile);

if rowS ~= rowM
    error('Both input matrices must have the same number of rows!');
end

% Load all elements between mobile and stationary units

gRegular = zeros(colS*colM, rowM*colM);
myIndex = 1;
for ij = 1:colS
   for jk = 1:colM
      gRegular(myIndex,((jk-1)*rowM +1):jk*rowM) =
      GetLOS(positionMobile(:,jk), positionStationary(:,ij));
      myIndex = myIndex + 1;
  end
end

% Load all elements between mobile units

numMeas = round((colM)*(colM - 1)/2);
gCross = zeros(numMeas, rowM*colM);
myDist = zeros(numMeas,1);
myIndex = 1;
for ij = 2:colM
   for jk = 1:(ij - 1)
      myLos = GetLOS(positionMobile(:,jk), positionMobile(:,ij));
      gCross(myIndex, ((ij - 1)*rowM +1):((ij)*rowM)) = myLos;
      gCross(myIndex, ((jk -1)*rowM +1):(jk*rowM)) = -myLos;
      myIndex = myIndex + 1;
   end
end

% Combine the two matrices

gOut = [gRegular; gCross];
```

```
function gOut = Get_LNS_Gs_Matrix(positionStationary, positionMobile)

% Function Get_LNS_Gs_Matrix generates the Leapfrog Navigation System
% Gs matrix given position estimates of all mobile and stationary
% units.
% Inputs: Stationary units positions, mobile units positions
% Output: LNS Gs matrix
% Guttorm R. Opshaug 2/14/02


[rowS colS] = size(positionStationary);
[rowM colM] = size(positionMobile);

if rowS ~= rowM
    error('Both input matrices must have the same number of rows!');
end


% Load all elements between mobile and stationary units

gRegular = zeros(colS*colM, rowM*colM);
myIndex = 1;
for ij = 1:colS
   for jk = 1:colM
      gRegular(myIndex,((ij-1)*rowM +1):ij*rowM) =
      -GetLOS(positionMobile(:,jk), positionStationary(:,ij));
      myIndex = myIndex + 1;
  end
end

% Load all elements between mobile units

numMeas = round((colM)*(colM - 1)/2);
gCross = zeros(numMeas, rowM*colM);

% Combine the two matrices

gOut = [gRegular; gCross];


function los = GetLOS(pos1, pos2)

% Function GetLOS generates the line-of-sight unit vector between two
positions.
% Input: Position 1 and Position 2
% Output: Line-of-sight unit vector between positions 1 and 2.
% Guttorm R. Opshaug 2/14/02

los = transp((pos2 - pos1)/norm(pos2 - pos1));
```

Appendix C

The antennas borrowed from Fantasma Networks Inc. came with no specifications on antenna pattern. However, I measured that characteristic by setting up a makeshift antenna range in the middle of the science and engineering quad at Stanford University. The same hardware as in Chapter 3.2.2 was used to measure reception power. One antenna was mounted on a plastic pole 4’ 10” off the ground, while the other one was put on a turn-table with angle markings, as shown in the figure below.

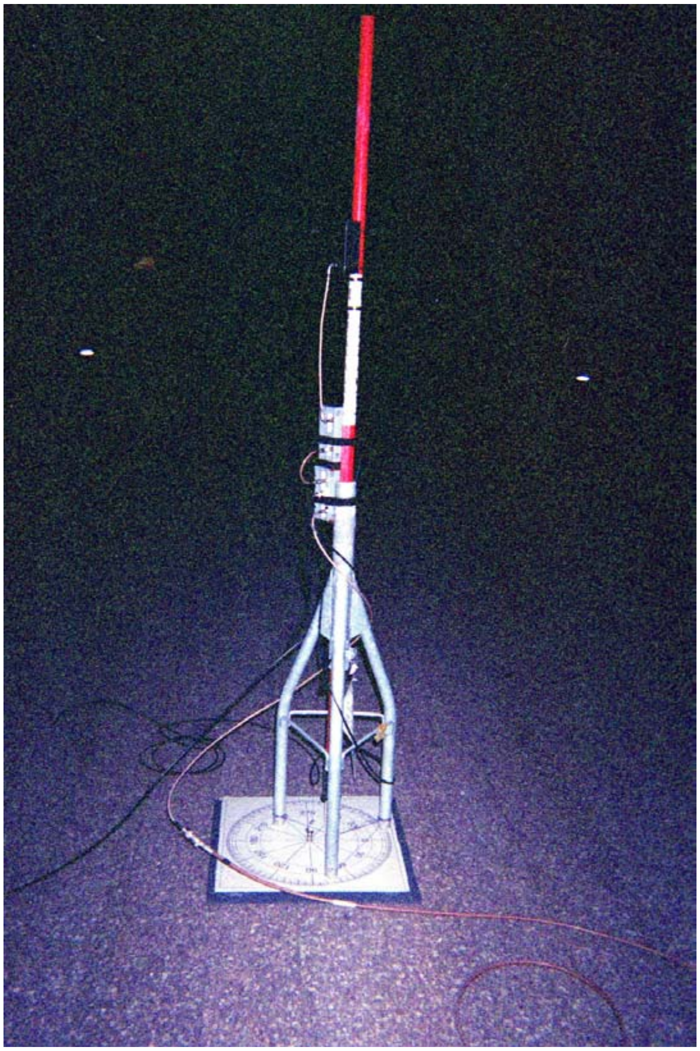

Figure C.1 Antenna Range

Measurements were taken every 30 degrees as the antenna was rotated, and the resulting antenna pattern is shown below.

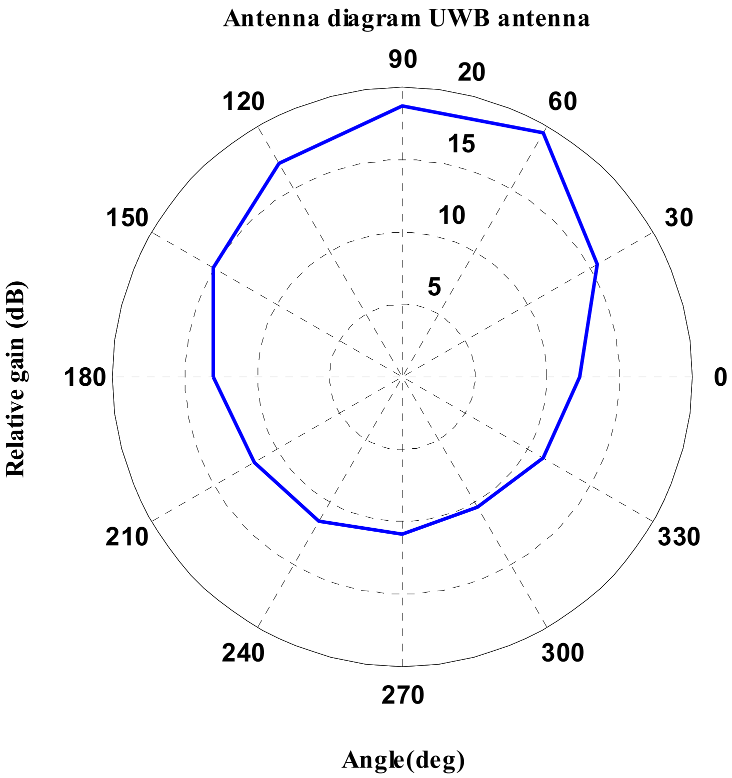

Figure C.2 Antenna Diagram for UWB Antenna

Appendix D

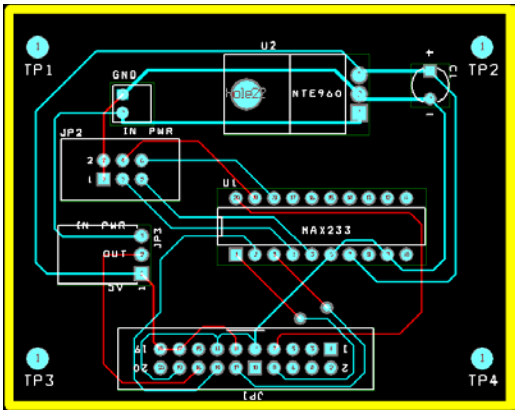

Figure D.1 PCB Layout

~

List of References

1 Aaron David, San Jose Mercury News

GPS pioneer wins prestigious award: Stanford emeritus professor shares $500,000 Draper prize

San Jose Mercury News, February 19, 2003

2 Marilynn Wylie Green, Maged Malkawi and S. S. Wang

E-911 mobile location and location-based technologies

SPIE, v.4586, p.274-281, 2001

3 Michael L. O'Conner

Carrier-phase differential GPS for automatic control of land vehicles

Thesis (Ph. D.)--Stanford University, 1998

4 Boris S. Pervan, David G. Lawrence, Konstantin G. Gromov, Guttorm R. Opshaug, Vicky Lu, Jock R.I. Christie, Ping-Ya Ko, Sam Pullen, Per Enge and Bradford Parkinson

Prototype LAAS Architecture Design Considerations

GPS Solutions, Vol. 2, No. 1, Summer 1998

5 Bradford W. Parkinson, James J. Spilker, Penina Axelrad and Per Enge

Global Positioning System: Theory and Applications

AIAA Inc, Washington DC, Progress in Astronautics and Aeronautics Vol. 163-164, 1996

6 J. Shewfelt, G. Turetzky, M. Chou

An Optimized GPS Receiver Architecture for Intellectual Property and System on Chip (SoC) Integration

ION-GPS Conference, Portland OR, 2002

7 Pratap Misra and Per Enge

Global Positioning System: Signals, Measurements, and Performance

Ganga-Jamuna Press, Lincoln MA, 1 edition, 2001

8 Theodore S. Rappaport

Wireless communications : principles and practice

Prentice Hall PTR, Upper Saddle River, N.J., 1 edition, 1996.

9 Per Enge, Rod Fan, Anil Tiwari, Andrew Chou, Wallace Mann, Anant Sahai, Jesse Stone and Ben Van Roy

Improving GPS Coverage and Continuity: Indoors and Downtown

ION-GPS Conference, Salt Lake City UT, 2001

10 Gerald F. Ross,

The transient analysis of multiple beam feed networks for array systems

Ph.D. dissertation, Polytechnic Institute of Brooklyn, Brooklyn, NY 1963

11 Federal Communications Commission

Part 15--Radio Frequency Devices

Code of Federal Regulations, Title 47, Volume 1, Washington DC, Revised as of August 20, 2002

12 Ravinder Kapoor, A. Banerjee, G.A. Tsihrintzis and N. Nandhakumar

UWB Radar Detection of Targets in Foliage Using Alpha-Stable Clutter Models

IEEE Transactions on Aerospace and Electronics, Vol. 35, July 1999

13 Moe Z. Win and Robert A. Scholtz

Characterization of Ultra-Wide Bandwidth Wireless Indoor Channels: A Communication-Theoritic View

IEEE Journal on Selected Areas in Communications, Vol. 20, Dec 2002

14 Ming Luo, Dennis Akos, Sam Pullen, and Per Enge

Interference to GPS from UWB transmitters

ION-GPS Conference Salt Lake City UT, 2000

15 Federal Communications Commission

FIRST REPORT AND ORDER: In the matter of Revision of Part 15 of the Commission's Rules Regarding Ultra-Wideband Transmission Systems

FCC, February 2002

16 Kenneth R. Johnson

Mars Pathfinder spacecraft, lander, and rover testing in simulated deep space and Mars surface environments

Journal of the Institute of Environmental Sciences, v.40, no.5, p.17-26, Sep-Oct 1997

17 H. Price, K. Cramer, S. Doudrick, W. Lee, J. Matijevic, S. Weinstein, T. Lam Trong, O. Marsal and R. Mitcheltree

Mars sample return spacecraft systems architecture

IEEE Aerospace Conference Proceedings, v.7, p.357-375, 2000

18 Jonathan M. Stone, Edward A. LeMaster, J. David Powell and Stephen Rock

GPS Pseudolite Transceivers and their Applications

ION National Technical Meeting, Anaheim CA, 1999

19 D. B. Wolfe, C. L. Judy, E. J. Haukkala and D. J. Godfrey

Engineering the world's largest DGPS network

Oceans Conference Record (IEEE) ; 2000; v.1, p.79-87

20 H. Stewart Cobb

GPS pseudolites: theory, design, and applications

Thesis (Ph. D.)--Stanford University, 1997

21 Edward A. LeMaster

Self-Calibrating Pseudolite Arrays: Theory and Experiment.

Thesis (Ph. D.)--Stanford University, 2002

22 John A. Orr and David Cyganski

Developing a System for Tracking and Locating Personnel in Hostile Environments

DARPA NETEX, September 2001

23 Robert Fleming, Cherie Kushner, Gary Roberts and Uday Nandiwada

Rapid Acquisition for Ultra-Wideband Localizers

IEEE UWB Science and Technology Conference, Baltimore MD, 2002

24 Robert Fontana and Steven Gunderson

Ultra-Wideband Precision Asset Location System

IEEE UWB Science and Technology Conference, Baltimore MD, 2002

25 John Phillips and Gerard Mac Namee

Personal wireless communication with DECT and PWT

Artech House, Boston MA, 1998

26 Peter Stuckmann

The GSM evolution : mobile packet data services

J. Wiley, New York NY, 2003

27 Donald C. Cox

910 MHz Urban Mobile Radio Propagation: Multipath Characteristics in New York City

IEEE Transactions on Communications, Vol. COM-21, November 1973

28 Snorre Kjesbu and Torkil Brunsvik

Radiowave propagation in industrial environments

IECON Proceedings (Industrial Electronics Conference); 2000; v.4, p.2425-2430

29 Dennis Akos, Ming Luo, Sam Pullen, and Per Enge

Ultra-Wideband and GPS: Can They Co-exist?

GPS World, September 2001

30 Digital John G. Proakis and Dimitris G. Manolakis

Digital Signal Processing: Principles, Algorithms and Applications

Macmillan Publishing Company, New York, NY, 2 edition, 1992

31 Kazimierz Siwiak

Ultra-Wide Band Radio: Introducing a New Technology

IEEE Semiannual Vehicular Technology Conference, Rhodes Greece, 2001

32 Qinghai, G. Huan and C. Wenyan

Constructing communication port of Manchester code with HSO/HSI of 8098/80c196 KB

Proceedings of the International Symposium on Test and Measurement; 2001; v.1, p.563-566

33 Charles A. Zweng and John Dohm

Flying the omnirange; a pilot's guide to the omnidirectional radio range, distance measuring equipment, and the Victor airways

Pan American Navigation Service, North Hollywood CA, 5 edition, 1959

34 David K. Barton (compiled and edited)

Radars

Artech House, Dedham MA, 1977-1980

35 Ilan Biton, Mark Koifman and Itzhack Bar Itzhack

Direct solution of the GPS equations

Proceedings of ION GPS, v.2, p.1313-1320, 1996

36 Clark E. Cohen

Attitude determination using GPS : development of an all solid-state guidance, navigation, and control sensor for air and space vehicles based on the Global Positioning System

Thesis (Ph. D.)--Stanford University, 1993

37 *Navstar GPS Space Segment / Navigation User Interface (ICD-200c)*

38 Donald C. Cox and Robert P. Leck

Correlation Bandwidth and Delay Spread Multipath Propagation Statistics for 910-MHz Urban Mobile Radio Channels

IEEE Transaction on Communication, Vol. COM-23, pp 1271-1280, November 1975

39 Matthias Pätzold

Mobile fading channels

J. Wiley, New York NY, 2002.

40 Kaveh Pahlavan, Prashant Krishnamurthy and Jaques Beneat

Wideband Radio Propagation Modeling for Indoor Geolocation Applications

IEEE Communications Magazine, April 1998

41 Tatsuo Furuno and Tokio Taga

Time Delay Spread in Microcellular Environment for Personal Communication Systems

IEICE Transactions on Communication, Vol. E79-B, September 1996

42 Börje Forssell

Radionavigation Systems

Prentice Hall International Ltd., Hertfordshire UK, 1991

43 J. Fairbrother

Height gain and location variability in a thirty metre cube

IEE Conf Publ, no.301 pt.2, p.281-284, 1989

44 Edward A. LeMaster and Stephen M. Rock.

Self-Calibration of Pseudolite Arrays Using Self-Differencing Transceivers.

ION-GPS Conference, Nashville TN, 1999

45 Paul Horowitz and Winfield Hill

The Art of Electronics

Cambridge University Press, Cambridge UK, 2 edition (reprint), 1997

46 Federal Communications Commission. Experimental radio station construction permit and license # wc2xlc, 2000

47 Victor T. Wullschleger, Daniel G. O'Laughlin and Franklin M. Haas

FAA flight test results for GPS wide area augmentation system (WAAS) cross-country demonstration

ION National Technical Meeting, Colorado Springs CO, 1994

48 Bradford W. Parkinson and Penina Axelrad

Autonomous gps integrity monitoring using the pseudorange residual.

Navigation. Journal of the Institute of Navigation; Summer 1988; v.35, no.2, p.255-274

49 Jaewoo Jung

High integrity carrier phase navigation using multiple civil GPS signals

Thesis (Ph. D.)--Stanford University, 2001

---

50 Terry Huntsberger, Hrand Aghazarian, Yang Cheng, Eric T. Baumgartner, Edward Tunstel, Chris Leger, Ashitey Trebi Ollennu and Paul S. Schenker

Rover autonomy for long range navigation and science data acquisition on planetary surfaces

IEEE International Conference on Robotics and Automation, Washington DC, 2002

51 Chih-Ming Su, Hong-Twu Chen, Fa-Shian Chang and Kin-Lu Wong

Dual-band slot antenna for 2.4/5.2 GHz WLAN operation

Microwave and Optical Technology Letters; Nov 20 2002; v.35, no.4, p.306-308

52 James Shau-Shiun Jan and Per Enge

Using GPS to Synthesize a Large Antenna Aperture When the Elements are Mobile

ION National Technical Meeting, Salt Lake City UT, 2000

53 Robert J. Danchik

Overview of transit development

Johns Hopkins APL Technical Digest, Jan-Mar 1998, v.19, no.1, p.18-26

54 Joseph R. Guinn

Mars surface asset positioning using in-situ radio tracking

AAS/AIAA Space Flight Mechanics Meeting, Santa Barbara CA, 2001

55 Victor Y. Lo

Characterization and simulation of end-to-end data link performance of the NASA deep space network

IEEE International Conference on Communications, Part 1, Montreal Canada, 1997

56 Demoz Gebre-Egziabher

Design and performance analysis of a low-cost aided dead reckoning navigator

Thesis (Ph. D.)--Stanford University, 2001

57 Paul Zarchan and Howard Musoff

Fundamentals of Kalman filtering : a practical approach

AAIA Inc, Reston VA, Progress in Astronautics and Aeronautics, Vol. 190, 2000

58 Masayoshi Matsuoka, Edward A. LeMaster, and Stephen M. Rock.

3-D Capabilities for GPS Transceiver Arrays

ION-GPS Conference, Portland OR, 2002

59 Karl A. Faymon

Microwave beam powered Mars airplane

Proceedings of the Intersociety Energy Conversion Engineering Conference, v.1, p.28-33, 1990

60 Guttorm R. Opshaug and Per Enge

Integrated GPS and UWB Navigation System

IEEE UWB Science and Technology Conference, Baltimore MD, 2002

61 Jonas Thor and Dennis M. Akos

A direct RF sampling multifrequency GPS receiver

IEEE PLANS, Position Location and Navigation Symposium, 2002

62 Richard D. Fontana, Wai Cheung and Tom Stansell

The Modernized L2 Civil Signal: Leaping Forward in the 21st Century

GPS World, September 2001

63 Guenter W. Hein, Jeremie Godet, Jean-Luc Issler, Jean-Christophe Martin, Philippe Erhard, Rafael Lucas-Rodriguez and Tony Pratt

Status of Galileo Frequency and Signal Design

ION-GPS Conference, Portland OR, 2002